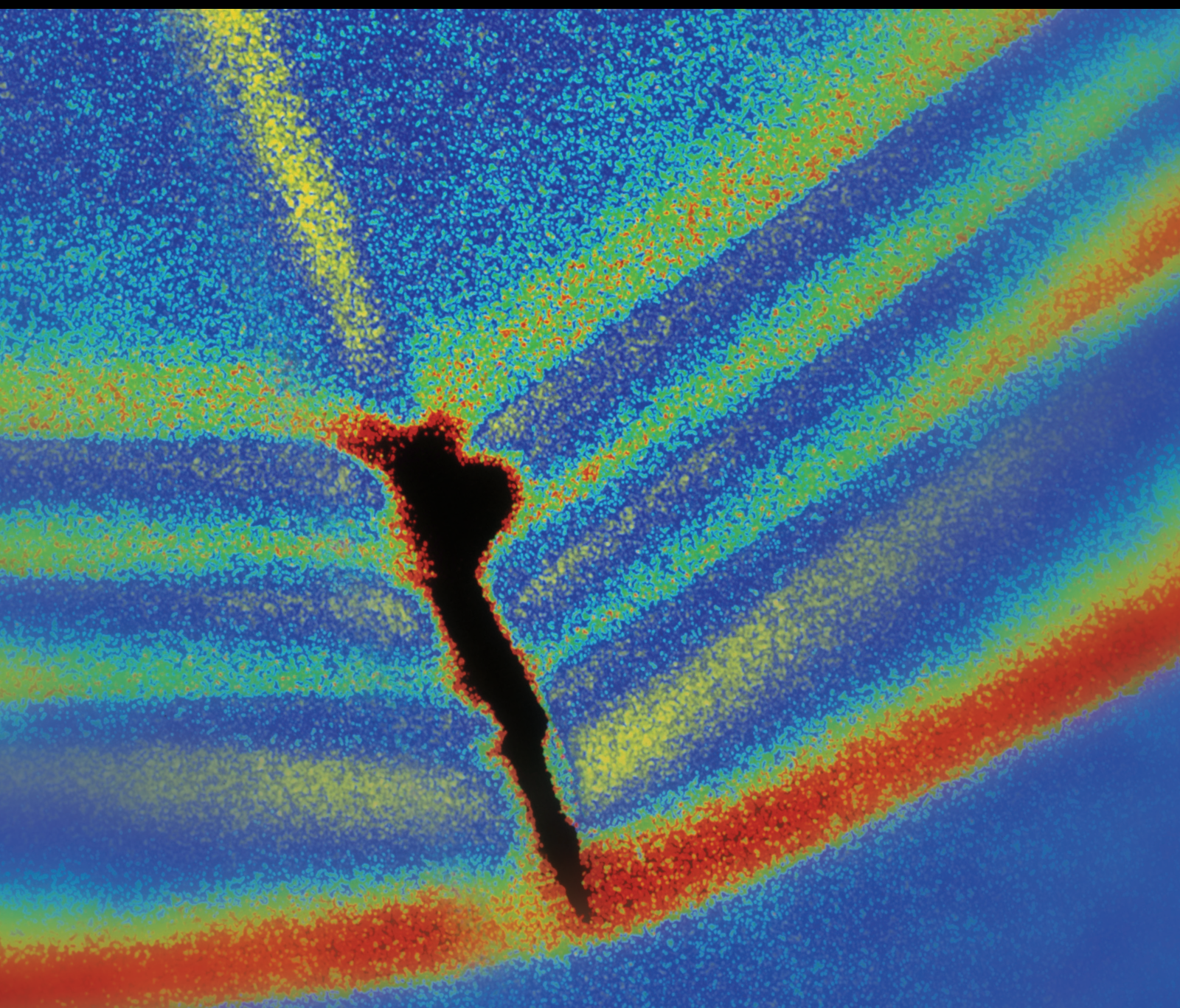


Shock and Vibration

# Shock and Vibration Induced by Mining Extraction 2016

Guest Editors: Caiping Lu, Linming Dou, Nong Zhang, Marcin A. Lutyński, and Shimin Liu





---

**Shock and Vibration Induced by  
Mining Extraction 2016**

Shock and Vibration

---

**Shock and Vibration Induced by  
Mining Extraction 2016**

Guest Editors: Caiping Lu, Linming Dou, Nong Zhang,  
Marcin A. Lutynski, and Shimin Liu



---

Copyright © 2016 Hindawi Publishing Corporation. All rights reserved.

This is a special issue published in "Shock and Vibration." All articles are open access articles distributed under the Creative Commons Attribution License, which permits unrestricted use, distribution, and reproduction in any medium, provided the original work is properly cited.

## Editorial Board

Brij N. Agrawal, USA  
Marco Alfano, Italy  
Farbod Alijani, Canada  
Sumeet S. Aphale, UK  
Mariano Artés, Spain  
Hassan Askari, Canada  
Matteo Aureli, USA  
Ranjan Banerjee, UK  
Mahmoud Bayat, Iran  
José A. Becerra Villanueva, Spain  
Marco Belloli, Italy  
Subhamoy Bhattacharya, UK  
Ivo Caliò, Italy  
Antonio Carcaterra, Italy  
Dumitru I. Caruntu, USA  
Noel Challamel, France  
Athanasios Chasalevris, UK  
Ashwin Chinnayya, France  
Giorgio Dalpiaz, Italy  
Farhang Daneshmand, Canada  
Sergio De Rosa, Italy  
Dario Di Maio, UK  
Longjun Dong, China  
Lorenzo Dozio, Italy  
Mohamed El Badaoui, France  
Mohammad Elahinia, USA  
Fiorenzo A. Fazzolari, UK  
Francesco Franco, Italy

Pedro Galvín, Spain  
Alessandro Gasparetto, Italy  
Gianluca Gatti, Italy  
Anindya Ghoshal, USA  
Nere Gil-Negrete, Spain  
Hassan Haddadpour, Iran  
M.I. Herreros, Spain  
Hamid Hosseini, Japan  
Reza Jazar, Australia  
Sakdirat Kaewunruen, UK  
Yuri S. Karinski, Israel  
Jeong-Hoi Koo, USA  
Georges Kouroussis, Belgium  
Mickaël Lallart, France  
Kenneth J. Loh, USA  
Nuno M. Maia, Portugal  
Giuseppe C. Marano, Italy  
Laurent Mevel, France  
Emiliano Mucchi, Italy  
Tony Murmu, UK  
Sundararajan Natarajan, India  
Toshiaki Natsuki, Japan  
Miguel Neves, Portugal  
Coral Ortiz, Spain  
Aleksandar Pavic, UK  
Evgeny Petrov, UK  
Antonina Pirrotta, Italy  
Vitomir Racic, Italy

Carlo Rainieri, Italy  
Didier Rémond, France  
Francesco Ripamonti, Italy  
Salvatore Russo, Italy  
Edoardo Sabbioni, Italy  
Jerzy T. Sawicki, USA  
Onome E. Scott-Emuakpor, USA  
Vadim V. Silberschmidt, UK  
Kumar V. Singh, USA  
Isabelle Sochet, France  
Alba Sofi, Italy  
Jussi Sopanen, Finland  
Stefano Sorace, Italy  
Narakorn Srinil, UK  
Salvatore Strano, Italy  
Chao Tao, China  
Mario Terzo, Italy  
Tai Thai, Australia  
Carlo Trigona, Italy  
Federica Tubino, Italy  
Nerio Tullini, Italy  
Marcello Vanali, Italy  
Jörg Wallaschek, Germany  
Zaili L. Yang, UK  
Stana Živanović, UK  
Lei Zuo, USA

# Contents

---

**Shock and Vibration Induced by Mining Extraction 2016**

Caiping Lu, Linming Dou, Nong Zhang, Marcin A. Lutyński, and Shimin Liu  
Volume 2016, Article ID 4502093, 1 page

**Algorithm Indicating Moment of P-Wave Arrival Based on Second-Moment Characteristic**

Jakub Sokolowski, Jakub Obuchowski, Radoslaw Zimroz, Agnieszka Wylomanska, and Eugeniusz Koziarz  
Volume 2016, Article ID 4051701, 6 pages

**Research on Effects of Blast Casting Vibration and Vibration Absorption of Presplitting Blasting in Open Cast Mine**

Li Ma, Kemin Li, Shuangshuang Xiao, Xiaohua Ding, and Sydney Chinyanta  
Volume 2016, Article ID 4091732, 9 pages

**Analysis and Numerical Simulation on the Reduction Effect of Stress Waves Caused by Water Jet Slotting Near Blasting Source**

Dengfeng Su, Yong Kang, Dongyang Li, Xiaochuan Wang, and Fuwen Yan  
Volume 2016, Article ID 5640947, 18 pages

**Numerical Analysis on Failure Modes and Mechanisms of Mine Pillars under Shear Loading**

Tianhui Ma, Long Wang, Fidelis Tawiah Suorineni, and Chunan Tang  
Volume 2016, Article ID 6195482, 14 pages

**Deformation and Failure Mechanism of Roadway Sensitive to Stress Disturbance and Its Zonal Support Technology**

Qiangling Yao, Xuehua Li, Fan Pan, Teng Wang, and Guang Wang  
Volume 2016, Article ID 1812768, 14 pages

**Research on the Rockburst Tendency and AE Characteristics of Inhomogeneous Coal-Rock Combination Bodies**

Yun-liang Tan, Wei-yao Guo, Qing-heng Gu, Tong-bin Zhao, Feng-hai Yu, Shan-chao Hu, and Yan-chun Yin  
Volume 2016, Article ID 9271434, 11 pages

## Editorial

# Shock and Vibration Induced by Mining Extraction 2016

Caiping Lu,<sup>1</sup> Linming Dou,<sup>2</sup> Nong Zhang,<sup>1</sup> Marcin A. Lutyński,<sup>3</sup> and Shimin Liu<sup>4</sup>

<sup>1</sup>*School of Mines, China University of Mining and Technology, Xuzhou 221116, China*

<sup>2</sup>*State Key Laboratory of Coal Resources and Safe Mining, China University of Mining and Technology, Xuzhou 221116, China*

<sup>3</sup>*Institute of Mining Engineering, Faculty of Mining and Geology, Silesian University of Technology, Ul. Akademicka 2, Gliwice, Poland*

<sup>4</sup>*Department of Energy and Mineral Engineering, School of Earth and Mineral Sciences, The Pennsylvania State University, State College, PA 16802, USA*

Correspondence should be addressed to Caiping Lu; [cplucumt@126.com](mailto:cplucumt@126.com)

Received 22 September 2016; Accepted 22 September 2016

Copyright © 2016 Caiping Lu et al. This is an open access article distributed under the Creative Commons Attribution License, which permits unrestricted use, distribution, and reproduction in any medium, provided the original work is properly cited.

With the increasing depth and intensity of coal mining, the rockburst and correspondingly induced dynamic disasters are aggravating, which has been a serious threat to the safety of coal mines. According to reliable statistics, only 32 coal mines were characterized by rockburst danger until 1985 in China; unfortunately, by the end of 2014, nearly 147 coal mines were classified as rockburst tendency. Simultaneously, the mining depth of about 50 coal mines reaches or surpasses 1000 m. In the period of 2004–2014, more than 35 fatal rockbursts occurred, which cruelly killed over 300 workers and caused thousands of injures. In despite of lack of accurate data about rockburst in coal mines in other countries, we believe that the rockburst should be a ubiquitous dynamic phenomenon in deep coal mines in the world.

It has been verified that the mining-induced shock or vibration can easily trigger strong tremor and even cause rockburst disaster in high-stress concentration region by experimental and field investigations. Therefore, it is very urgent to essentially understand the mining-induced shock and vibration waves in coal mines.

Our special issue is dedicated to fundamental understanding of mining-induced shock and vibration waves mainly concentrated on mechanical principles, propagation and attenuation laws, monitoring and warning methods, and prevention of catastrophic shock. A total of 6 papers have been accepted for publication in the special issue, which is mainly divided into four aspects that are the deformation and failure mechanism of coal and rock with rockburst tendency, the propagation and attenuation rules of shock wave

including blasting waves, early warning based on acoustic emission (AE), and innovative supporting technologies of roadway in deep coal mines, respectively. By rigorous review and negotiation, two highlights are presented that are the numerical analysis on failure modes and mechanisms of mine pillars and the reduction effect of stress waves caused by water jet slotting near blasting source.

Rockburst in coal mines is a worldwide conundrum poorly understood, the early-warning indexes are confusing and exasperating; especially, its prevention is yet not effectively resolved. The satisfactory solution compulsorily requires the worldwide efforts and cooperation in coal mining and rock mechanics community.

*Caiping Lu  
Linming Dou  
Nong Zhang  
Marcin A. Lutyński  
Shimin Liu*

## Research Article

# Algorithm Indicating Moment of P-Wave Arrival Based on Second-Moment Characteristic

Jakub Sokolowski,<sup>1</sup> Jakub Obuchowski,<sup>1</sup> Radosław Zimroz,<sup>1</sup>  
Agnieszka Wyłomanska,<sup>2</sup> and Eugeniusz Koziarz<sup>3</sup>

<sup>1</sup>KGHM CUPRUM Ltd., CBR, Sikorskiego 2-8, 53-659 Wrocław, Poland

<sup>2</sup>Faculty of Pure and Applied Mathematics, Hugo Steinhaus Center, Wrocław University of Science and Technology, Janiszewskiego 14a, 50-370 Wrocław, Poland

<sup>3</sup>KGHM Polska Miedź S.A. O/ZG "Rudna", Henryka Dąbrowskiego 50, 59-100 Polkowice, Poland

Correspondence should be addressed to Jakub Sokolowski; [jsokolowski@cuprum.wroc.pl](mailto:jsokolowski@cuprum.wroc.pl)

Received 22 April 2016; Accepted 1 August 2016

Academic Editor: Shimin Liu

Copyright © 2016 Jakub Sokolowski et al. This is an open access article distributed under the Creative Commons Attribution License, which permits unrestricted use, distribution, and reproduction in any medium, provided the original work is properly cited.

The moment of P-wave arrival can provide us with many information about the nature of a seismic event. Without adequate knowledge regarding the onset moment, many properties of the events related to location, polarization of P-wave, and so forth are impossible to receive. In order to save time required to indicate P-wave arrival moment manually, one can benefit from automatic picking algorithms. In this paper two algorithms based on a method finding a regime switch point are applied to seismic event data in order to find P-wave arrival time. The algorithms are based on signals transformed via a basic transform rather than on raw recordings. They involve partitioning the transformed signal into two separate series and fitting logarithm function to the first subset (which corresponds to pure noise and therefore it is considered stationary), exponent or power function to the second subset (which corresponds to nonstationary seismic event), and finding the point at which these functions best fit the statistic in terms of sum of squared errors. Effectiveness of the algorithms is tested on seismic data acquired from O/ZG "Rudna" underground copper ore mine with moments of P-wave arrival initially picked by broadly known STA/LTA algorithm and then corrected by seismic station specialists. The results of proposed algorithms are compared to those obtained using STA/LTA.

## 1. Introduction

Obtaining accurate information about seismic phenomena induced by mining activity might be a difficult task. The recordings strongly depend on distance between source and measuring device, energy of the event, lithology of the rock mass, device parameters, noise induced by transmission line, and so forth. In order to acquire exact features of the event (like, e.g., 3-dimensional location) recordings from at least four different one-axial sensors are required.

When the seismic event occurs, its energy is transported via different types of seismic waves, which can be primarily classified as body waves (P-wave, S-wave) and surface waves (Rayleigh wave, Love wave, and Stoneley wave). P-waves possess the highest velocity among others; thus they indicate

onset of the event. Therefore, in order to receive detailed information about particular phenomenon, the first step is to indicate its moment of P-wave arrival.

From mathematical point of view the problem is isometric with finding a moment in time series where it loses stationarity (as the background noise is considered to be stationary) or as a problem of finding structural break point.

The moment of P-wave arrival is commonly used in estimation of event location [1], energy [2], and focal mechanism [3]. Determining such a moment manually is time-consuming and requires considerable experience. However, under development of science and technology, many automatic P-wave picking algorithms were proposed. Implementation and use of such methods are a much faster solution but not 100% reliable, as the results frequently differ from indications

given by seismic station specialists. Thus the algorithms are frequently used as an initial pick followed by experts' manual correction.

So far, there are plenty of different algorithms which can be divided into 2 main groups: proceeding in time and proceeding in frequency domain [4]. Broadly known time domain methods include AR-AIC [5, 6], which fits autoregressive model to the data and determines the moment of P-wave arrival in a point where Akaike Information Criterion [7] is minimized, and STA/LTA algorithm [8, 9], which for fixed characteristic function (e.g., square of the signal) computes its average over short and long time window and indicates the onset time when the ratio of averages exceeds predefined value. The moment of P-wave arrival might be also determined with use of neural networks [10, 11], methods based on wavelet transform [12, 13], spectrogram [14, 15], and cross-correlation [16].

When dealing with the problem of P-wave arrival moment, one may investigate it as an element of a signal segmentation procedure [17, 18], as the indication of onset moment is basis for segmentation. Common methods are often used in both problems.

Recently, a method of finding a critical point which divides the time series into two stationary parts with different variances has been proposed [19]. The basis for this method is statistical property of the second central statistical moment; that is, the expected value of cumulative sum of squares for stationary time series increases linearly with time. Such property is independent of the underlying probability distribution, as long as the variance is finite. The method has been already utilized in structural break detection method [20]. It was decided to involve this idea for P-wave arrival point estimation. However, the entire seismic event does not possess stationarity property, nor it can be split into two stationary time series. Thus the method requires a modification. In this paper two similar methods are proposed and compared to a widely used STA/LTA algorithm. All of the investigated automatic P-wave picking methods are compared with arrivals indicated by specialists of O/ZG "Rudna" underground copper ore mine seismic station experts due to their extensive experience in analysis of mining-induced seismic events.

The rest of the paper is organized as follows: in Methodology the new method of structural break detection is presented. Moreover, we recall the STA/LTA algorithm (the classical method used to detection of P-wave arrival time). Next, in Section 3 of application to real data, the new methodology is applied to the real seismic signals. Obtained results are compared with the STA/LTA technique. The last section contains conclusions.

## 2. Methodology

**2.1. STA/LTA Algorithm.** One of the classical algorithms that are often used in the problem of P-wave arrival moment detection is based on the short-term-average and long-term-average (STA/LTA) trigger method. The underlying idea of this method is to evaluate in a continuous fashion the value

of characteristic function (CF) of a seismic signal in two moving-time windows (one short and one long) in order to detect the seismic event. The characteristic function used for calculation purpose can be defined as energy, absolute amplitude, or envelope function of the microseismic trace. Irrespective of the definition of the characteristic function (CF), the short time window (STA) is supposed to measure the instantaneous amplitude of the seismic signal, whereas the long time window (LTA) provides information about the amplitude of seismic noise. When their ratio exceeds a predefined value  $\tau_A$  (activation threshold), the following recorded samples are marked to be event-driven until the ratio falls below another predefined value  $\tau_D$  called the deactivation threshold. In this algorithm, for a raw signal  $x_1, \dots, x_n$ , the following statistic  $SLR_t$  is being calculated:

$$SLR_t = \frac{(1/s) \sum_{k=t-s}^t CF(x_k)}{(1/l) \sum_{k=t-l}^t CF(x_k)}, \quad (1)$$

where  $s$  and  $l$  denote short and long time windows lengths (in samples), respectively. Moreover, in the above equation  $CF(x)$  is a specific characteristic function defined in terms of signal energy. In the literature different characteristic functions can be found, such as absolute value of the signal or envelope of the microseismic trace. In this paper we consider  $CF(x) = x^2$ .

In the STA/LTA algorithm the inspection of the  $SLR_t$  statistic is performed and on such basis one can detect the moment of P-wave arrival. This moment is the minimum  $t$  for which the ratio STA/LTA exceeds the predefined value  $\rho$ ; that is,

$$t_p = \min_t SLR_t > \rho. \quad (2)$$

In this paper we compare the classical approach based on the STA/LTA algorithm with the new algorithm based on the cumulative empirical second moment of given raw signal.

**2.2. Algorithm Based on the Empirical Second Moment.** As it was mentioned, the proposed method is based on the empirical second moment of given raw signal  $x_1, \dots, x_n$ . First, we introduce the statistic which is a cumulative second moment of given sample:

$$C_x(t) = \sum_{i=1}^t x_i^2. \quad (3)$$

The  $C_x(t)$  statistic was used in [19] as a base of the method applied in the segmentation problem in case when in real data we observe that some characteristics change with respect to time. This statistic was also a main point of the testing procedure whether in the given sample a structural break point exists or not.

In this paper we extend the methodology presented in [19] and propose to analyze the following statistic:

$$L_x(t) = \log C_x(t). \quad (4)$$

This choice is motivated by seismic recordings characteristics and discussion is carried out in further sections. As one can

expect  $L_x$  can tend to  $-\infty$  if at least the first reading is equal to 0. In order to avoid this problem we modify the raw signal and in the further analysis instead of  $x_1, \dots, x_n$  we substitute the first reading  $x_1$  with the first nonzero reading. This technical issue is related to a single sample at the very beginning of the recording; thus it does not influence the results. We denote corrected series as  $x'_1, \dots, x'_n$ .

Until the moment of P-wave arrival, the seismic recordings  $x_t$  consist of ambient noise which is considered stationary [21]; obviously they can be described by independent identically distributed Gaussian random variables. Moreover, we assume that the theoretical second moment of the distribution is finite. It can be shown that for data before the moment of P-wave arrival we have the following:

$$EL_{x'}(n) \sim \log(n). \quad (5)$$

Our methodology is therefore based on this observation. In the procedure, in contrast to [19], we fit the logarithm function  $f_1 = a + b \log(x)$  to first  $k$  points of  $L_{x'}(t)$  statistic. After the moment of P-wave arrival the character of the  $L_{x'}(t)$  statistic changes. It is not exactly known what kind of function we can observe after the moment of P-wave arrival; however it was noted that in general the statistic is concave with respect to  $t$ . Here we decided to test two different concave functions: exponential  $f_2 = c \exp dx + \text{const}$  and power  $f_3 = gx^n + \text{const}$ . These functions are fitted with time shift; that is,  $f(t) = L_{x'}(t - k)$ ,  $t = k + 1, \dots, n$ . In order to reduce computational time we subtract  $L_{x'}(n)$  or  $L_{x'}(k + 1)$  and then fit the exponential or power functions, respectively. Fitted functions coefficients are obtained by using of Levenberg-Marquardt algorithm (LMA) [22, 23] which is an iterative algorithm used to solve nonlinear least squares problems. It combines features of Gauss-Newton method and the method of gradient descent [24]. The LMA algorithm requires at least 3 points to fit considered functions. The next step is to calculate the squared errors between  $L_{x'}(t)$  and fitted functions. The estimated point of P-wave arrival is  $k$  for which the error is minimized.

Entire detection algorithm can be described as follows:

- (1) Set  $k = 3$ .
- (2) If  $k = n - 2$  go to (7).
- (3) Fit  $f_1 = a + b \log x$  to  $\{L_{x'}(1), \dots, L_{x'}(k)\}$ ,  $f_2 = c \exp(d(x - k))$  to  $\{L_{x'}(k + 1), \dots, L_{x'}(n)\} - L_{x'}(n)$ , and  $f_3 = e(x - k)^n$  to  $\{L_{x'}(k + 1), \dots, L_{x'}(n)\} - L_{x'}(k + 1)$ .
- (4) Calculate  $e_i^1 = \sum_{j=1}^k (f_1(j) - L_{x'}(j))^2 + \sum_{j=k+1}^n (f_2(j - k) - (L_{x'}(j) - L_{x'}(n)))^2$ . Calculate  $e_i^2 = \sum_{j=1}^k (f_1(j) - L_{x'}(j))^2 + \sum_{j=k+1}^n (f_3(j - k) - (L_{x'}(j) - L_{x'}(n)))^2$ .
- (5) Set  $k = k + 1$ .
- (6) Go to (2).
- (7)  $l_1 = \arg \min (e_k^1)$ ,  $l_2 = \arg \min (e_k^2)$ .

$l_1$  is "exponent" estimator, and  $l_2$  the "power" one.

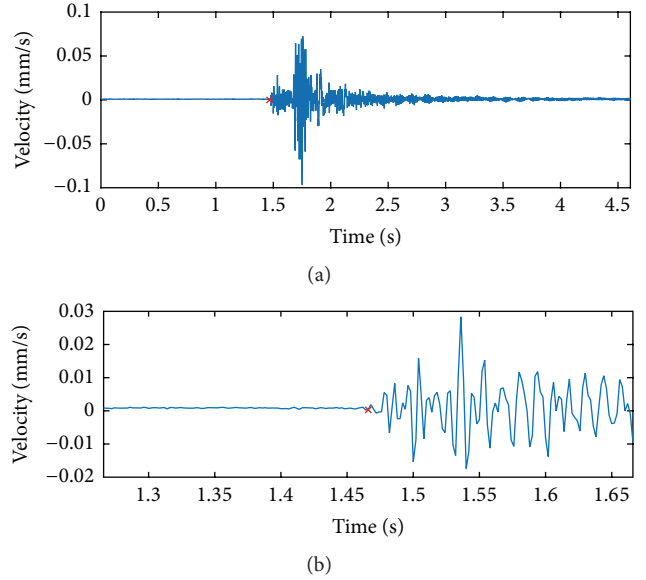


FIGURE 1: Exemplary seismic event with P-wave arrival determined by specialists (a) and its zoom (b).

### 3. Application to Real Seismic Data

In this paper the proposed algorithm was applied to a 188 single-event recordings from O/ZG "Rudna" underground copper ore mine. The signals were gathered by seismic system ELOGOR-C which is used to rock mass observation. The system consists of 2 sets of 32 seismometers Willmore MK-III type; each collects velocity data in the frequency band 0.5–150 Hz which is adequate frequency band containing mining-induced events. Such band is enough for localization, seismic energy estimation, and focal mechanism indication by analysis of first motion direction, which is the basic purpose of the monitoring system. The microseismic events in higher frequency are registered in this mine by a different system. The data is transmitted to seismic station using analog transmission (frequency modulation) and sampled with sampling frequency 500 Hz. Due to characteristics of the deposit, the seismic system network is relatively flat and a few additional sensors are located in shafts. Analyzed signals are dated from August 1, 2015, to August 19, 2015. The events length extent from 4.6 s to 33 s. Moments of P-wave arrival was indicated preliminarily using the STA/LTA algorithm and then manually corrected by seismic station experts.

In Figure 1 an exemplary seismic event is presented with moment of P-wave arrival marked by red cross. In Figure 1(b) zoom on the arrival time is shown. It is easy to spot stationarity of the background noise before the arrival of P-wave (red cross).

Application of  $C_x(t)$  statistic can be seen in Figure 2.

As it was noted in [19], when applying  $C_x(t)$  statistic to a stationary process with variance  $\sigma^2$ , its expected value would be  $EC_x(t) = t\sigma^2$ . Seismic recordings before the moment of P-wave arrival (denote  $p$ ) fulfill the stationarity assumptions.

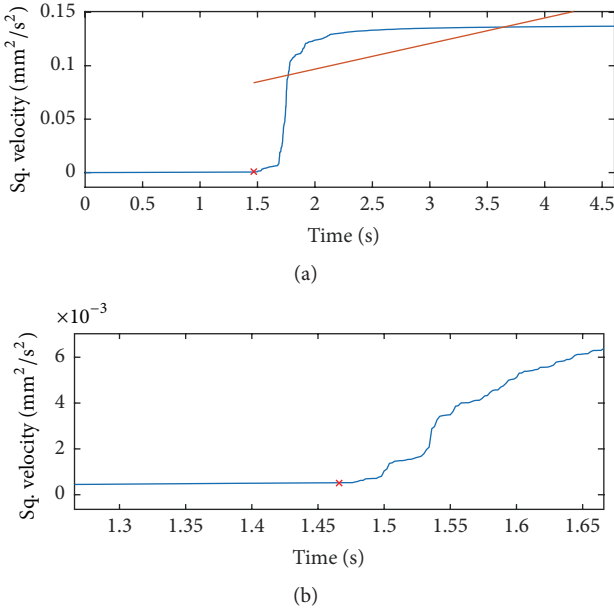


FIGURE 2:  $C_{x'}(t)$  statistic applied to exemplary seismic signal presented in Figure 1 (a) and its zoom (b).

However, strict utilization of algorithm proposed in [19] cannot work properly, as after the P-wave arrives the series is not stationary.  $R^2$  statistics were computed for linear fits from arrival point indicated by seismic station specialists to the end of recording (see example in Figure 2). The mean value of these  $R$ -statistics for the entire set of seismic records is 0.349 which is unacceptable. Thus the P-wave arrival indicated by using inappropriately fitted function might be false. Application of logarithm function to  $C_x(t)$  statistics might highlight the P-wave arrival, since the structural change is sudden in case of  $L_{x'}(t)$  statistic contrary to  $C_x(t)$ .

In Figure 3 the values of  $L_{x'}(t)$  statistic are contained. With use of logarithm, the break point (Figure 3, marked with red cross) might be noticed much easier than it could be indicated from  $C_{x'}(t)$  (Figure 2).

It is worth to notice that the  $L_{x'}(t)$  statistic can be divided into 2 concave series, and the division point is located in the moment of P-wave arrival (marked with red cross).

Figure 3 presents the quality of fit. The average  $R^2$  statistic for power function fit (fitted on the interval from the onset moment indicated by seismic station experts till the end of recording) is equal 0.976 and 0.974 for exponential function. This indicates that these functions appropriately approximate the  $L_{x'}$  statistics.

**3.1. Algorithm Results with Exponential Function Fitted.** In Figure 4 results of the algorithm (exponential function fitted to the second part of statistic) are contained. Performed data analysis provides that 54.3% of algorithm picks do not differ by more than 10 samples (which corresponds to 0.02 s) from moments indicated by seismic station experts. 79.9% of differences do not exceed 50 samples (0.1 s). The largest difference is 177 samples (0.354 s).

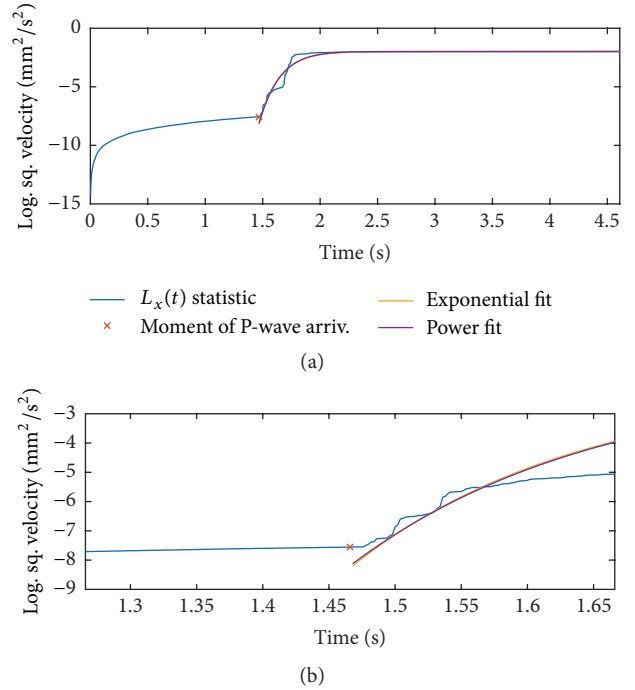


FIGURE 3:  $L_{x'}(t)$  statistic applied to exemplary seismic signal presented in Figure 1 (a) and its zoom (b). Fit parameter  $R^2 = 0.9557$  and 0.9591 for exponential and power function fitting, respectively.

**3.2. Algorithm Results with Power Function Fitted.** The results presented in Figures 4 and 5 provide that exponential and power fitting lead to similar results. Within the power function fitted 58.5% of differences do not exceed 10 samples (0.02 s) and 83% do not exceed 50 samples (0.1 s). The largest difference is 255 samples (0.51 s).

**3.3. Results Based on STA/LTA.** In order to examine performance of the proposed algorithms we compare them to P-wave picks obtained by the STA/LTA method with the most optimal parameters. The method requires predefined threshold  $\rho$ . The P-wave arrival is triggered when the STA/LTA ratio exceeds  $\rho$ . Also, the length of short and long time windows needs to be predefined. This is a drawback of this method, as optimal values of these quantities can change for different working conditions of sensors.

The algorithm was tested with different  $\rho$  values from 1 to 10 (step 0.05). Simultaneously, different lengths of short and long time windows were tested (short window from 10 to 200, step 10 samples, and long window from 10 to 400 samples more than the short one, step 10 samples). The most accurate estimated arrival moments were obtained with  $\rho = 2.2$  and  $s = 20$  samples and  $l = 320$  samples.

In Figure 6 one can observe that results are significantly worse than that these provided by the novel algorithms based on second statistical moment. The analysis provides that 47.8% and 71.7% of picks do not exceed 10 and 50 samples, respectively. Additionally, STA/LTA algorithm missed 3 P-wave arrivals; algorithm proceeded through entire signal and without any moment triggered. The largest difference

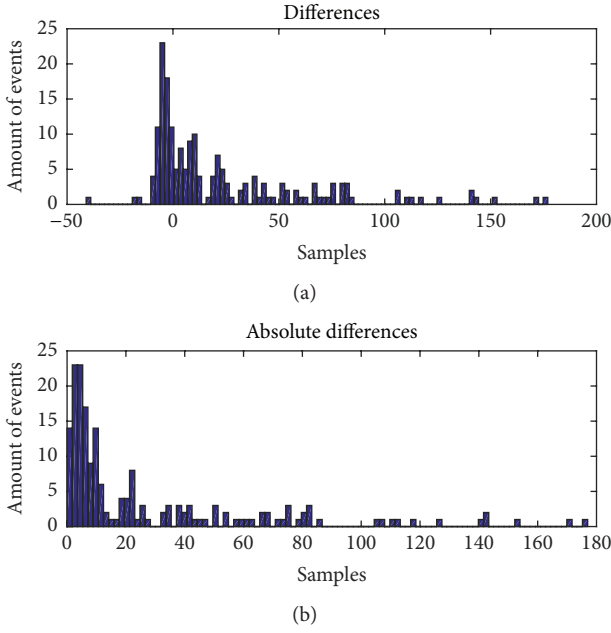


FIGURE 4: Histogram of differences between algorithm picks and those given by specialists: exponential function fitted (a) and histogram of absolute differences (b).

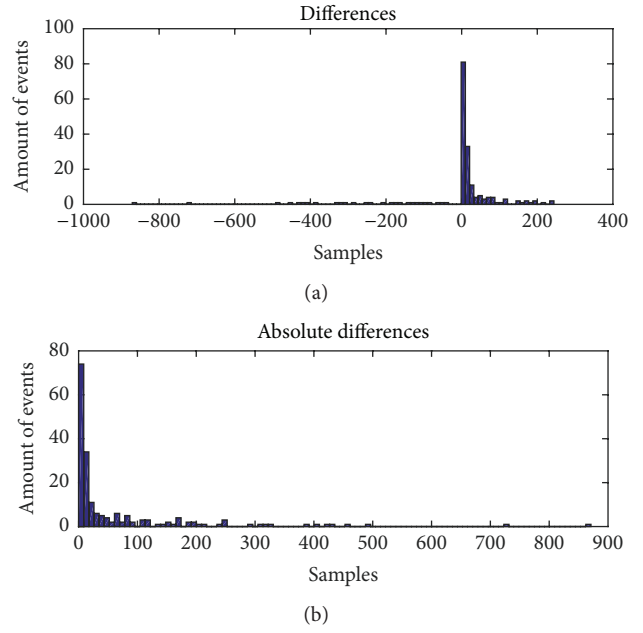


FIGURE 6: Histogram of absolute differences between STA/LTA picks and those given by experts (a) and histogram of absolute differences (b).

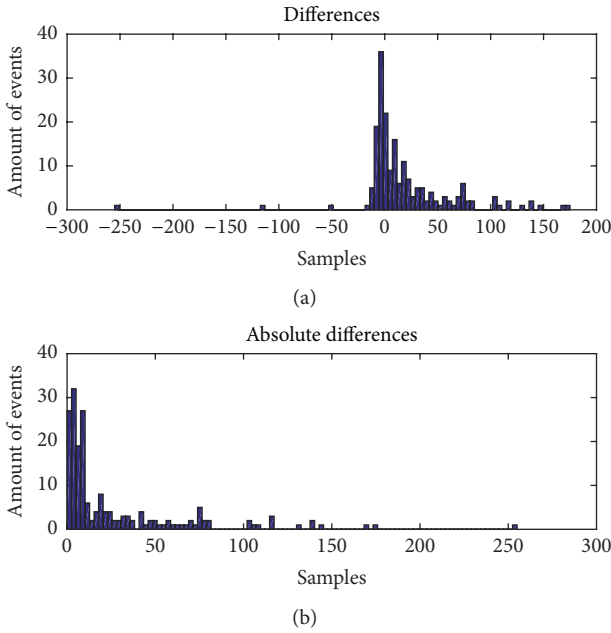


FIGURE 5: Histogram of differences between algorithm picks and those given by specialists: power function fitted (a) and histogram of absolute differences (b).

between algorithm results and seismic station specialists is 490 samples (0.98 s). Moreover, significantly more events are indicated before the actual moment of P-wave arrival. This shows that STA/LTA is prone to outliers.

In Table 1 basic statistics are included in order to compare three investigated methods. As it can be noticed the proposed algorithms outperform STA/LTA algorithm in all aspects,

TABLE 1: Comparison between algorithms based on second statistical moment and STA/LTA method.

	Algorithm (exp)	Algorithm (power)	STA/LTA
Number of correct (exact) picks	5	7	2
Mean of absolute differences	27.2935	27.2287	51.4505
Std. dev. of differences	39.2442	43.8035	101.3341
Std. dev. of abs. differences	36.6021	39.2816	87.2602
Mode of abs. differences	3	3	3

expect the mode of absolute differences which is equal to 3 for all methods. Fitting the power function provides the best results in terms of correct picks and mean of absolute differences but has worse standard deviations than the exponential fitting.

### 4. Conclusions

In this paper the regime switching detection method was adopted in order to find P-wave arrival. The algorithm was tested on seismic signal recordings from O/ZG “Rudna” underground copper ore mine. The results included in this paper show that the proposed algorithms are capable of indicating P-wave arrival moments as the estimated points were close with points manually indicated by mine station experts. The results were also compared to those provided by

widely used STA/LTA algorithm. Results of both fitting algorithms give better results than the results obtained using the STA/LTA method in terms of descriptive statistics. Moreover, the algorithm does not require any parameters nor calibration to proceed. Comparison of two proposed functions (power and exponential) does not provide clear answer which one is better. The power function leads to higher number of correct picks and lower mean of absolute differences but higher standard deviations of differences between estimated and actual picks.

Despite the fact that algorithms are considerably more accurate than STA/LTA, they still possess some drawbacks. The most noticeable concern is the computational complexity of the basic implementation, since for each signal many fittings (namely, twice the signal length) have to be performed. Additionally, STA/LTA can be computed online and provide information about event occurrence immediately. In case of the novel algorithms the response time might be minimized by considering only a short part of the signal registered after the P-wave arrival. The minimum number of samples acquired after the P-wave arrival that provides accurate pick is therefore of high importance. Moreover, algorithms for exponential or power functions fitting that update the fitted coefficients might significantly increase the computational speed. In future work the proposed methods might be upgraded in order to test whether the seismic event occurred or not. It is also interesting to assess the impact of better P-wave picking on localization accuracy. The method can also be tested for nonanthropogenic teleseismic events.

## Competing Interests

The authors declare that there are no competing interests regarding the publication of this article.

## References

- [1] W. Spence, "Relative epicenter determination using P-wave arrival-time differences," *Bulletin of the Seismological Society of America*, vol. 70, no. 1, pp. 171–183, 1980.
- [2] J. Boatwright and J. B. Fletcher, "The partition of radiated energy between P and S waves," *Bulletin of the Seismological Society of America*, vol. 74, no. 2, pp. 361–376, 1984.
- [3] G. Kwiatek and Y. Ben-Zion, "Assessment of P and S wave energy radiated from very small shear-tensile seismic events in a deep South African mine," *Journal of Geophysical Research: Solid Earth*, vol. 118, no. 7, pp. 3630–3641, 2013.
- [4] M. Withers, R. Aster, C. Young et al., "A comparison of select trigger algorithms for automated global seismic phase and event detection," *Bulletin of the Seismological Society of America*, vol. 88, no. 1, pp. 95–106, 1998.
- [5] R. Sleeman and T. van Eck, "Robust automatic P-phase picking: an on-line implementation in the analysis of broadband seismogram recordings," *Physics of the Earth and Planetary Interiors*, vol. 113, no. 1–4, pp. 265–275, 1999.
- [6] M. Leonard and B. L. N. Kennett, "Multi-component autoregressive techniques for the analysis of seismograms," *Physics of the Earth and Planetary Interiors*, vol. 113, no. 1–4, pp. 247–263, 1999.
- [7] H. Akaike, "Information theory and an extension of the maximum likelihood principle," in *Selected Papers of Hirotugu Akaike*, Springer Series in Statistics, pp. 199–213, Springer New York, New York, NY, USA, 1998.
- [8] R. V. Allen, "Automatic earthquake recognition and timing from single traces," *Bulletin of the Seismological Society of America*, vol. 68, no. 5, pp. 1521–1532, 1978.
- [9] M. Leonard, "Comparison of manual and automatic onset time picking," *Bulletin of the Seismological Society of America*, vol. 90, no. 6, pp. 1384–1390, 2000.
- [10] J. Wang and T.-L. Teng, "Artificial neural network-based seismic detector," *Bulletin of the Seismological Society of America*, vol. 85, no. 1, pp. 308–319, 1995.
- [11] S. Gentili and A. Michelini, "Automatic picking of P and S phases using a neural tree," *Journal of Seismology*, vol. 10, no. 1, pp. 39–63, 2006.
- [12] K. S. Anant and F. U. Dowla, "Wavelet transform methods for phase identification in three-component seismograms," *Bulletin of the Seismological Society of America*, vol. 87, no. 6, pp. 1598–1612, 1997.
- [13] H. Zhang, C. Thurber, and C. Rowe, "Automatic P-wave arrival detection and picking with multiscale wavelet analysis for single-component recordings," *Bulletin of the Seismological Society of America*, vol. 93, no. 5, pp. 1904–1912, 2003.
- [14] A. G. Hafez, T. A. Khan, and T. Kohda, "Earthquake onset detection using spectro-ratio on multi-threshold time-frequency sub-band," *Digital Signal Processing*, vol. 19, no. 1, pp. 118–126, 2009.
- [15] G. Xiantai, L. Zhimin, Q. Na, and J. Weidong, "Adaptive picking of microseismic event arrival using a power spectrum envelope," *Computers & Geosciences*, vol. 37, no. 2, pp. 158–164, 2011.
- [16] E. H. Ait Laasri, E.-S. Akhouayri, D. Agliz, and A. Atmani, "Automatic detection and picking of P-wave arrival in locally stationary noise using cross-correlation," *Digital Signal Processing*, vol. 26, no. 1, pp. 87–100, 2014.
- [17] D. Kucharczyk, A. Wyłomańska, J. Obuchowski, R. Zimroz, and M. Madziarz, "Stochastic modelling as a tool for seismic signals segmentation," *Shock and Vibration*, vol. 2016, Article ID 8453426, 13 pages, 2016.
- [18] R. Zimroz, M. Madziarz, G. Żak, A. Wyłomańska, and J. Obuchowski, "Seismic signal segmentation procedure using time-frequency decomposition and statistical modelling," *Journal of Vibroengineering*, vol. 17, no. 6, pp. 3111–3120, 2015.
- [19] J. Gajda, G. Sikora, and A. Wyłomańska, "Regime variance testing—a quantile approach," *Acta Physica Polonica B*, vol. 44, no. 5, pp. 1015–1035, 2013.
- [20] D. Kucharczyk, A. Wyłomańska, and R. Zimroz, "Structural break detection method based on the Adaptive Regression Splines technique," <http://arxiv.org/abs/1605.08667v1>.
- [21] S. J. Gibowicz and A. Kijko, *An Introduction to Mining Seismology*, vol. 55, Elsevier, New York, NY, USA, 2013.
- [22] K. Levenberg, "A method for the solution of certain non-linear problems in least squares," *Quarterly of Applied Mathematics*, vol. 2, no. 2, pp. 164–168, 1944.
- [23] D. W. Marquardt, "An algorithm for least-squares estimation of nonlinear parameters," *Journal of the Society for Industrial and Applied Mathematics*, vol. 11, no. 2, pp. 431–441, 1963.
- [24] A. Cauchy, "Méthode générale pour la résolution des systèmes d'équations simultanées," *Comptes Rendus de l'Académie des Sciences Paris*, vol. 25, pp. 536–538, 1847.

## Research Article

# Research on Effects of Blast Casting Vibration and Vibration Absorption of Presplitting Blasting in Open Cast Mine

Li Ma,<sup>1,2</sup> Kemin Li,<sup>2</sup> Shuangshuang Xiao,<sup>2</sup> Xiaohua Ding,<sup>2</sup> and Sydney Chinyanta<sup>2</sup>

<sup>1</sup>State Key Laboratory for Geomechanics & Deep Underground Engineering, China University of Mining and Technology, Xuzhou, Jiangsu 221116, China

<sup>2</sup>School of Mines, China University of Mining and Technology, Xuzhou, Jiangsu 221116, China

Correspondence should be addressed to Kemin Li; [likemin513@126.com](mailto:likemin513@126.com)

Received 3 January 2016; Revised 16 June 2016; Accepted 29 June 2016

Academic Editor: Georges Kouroussis

Copyright © 2016 Li Ma et al. This is an open access article distributed under the Creative Commons Attribution License, which permits unrestricted use, distribution, and reproduction in any medium, provided the original work is properly cited.

The impact energy produced by blast casting is able to break and cast rocks, yet the strong vibration effects caused at the same time would threaten the safety of mines. Based on the theory of Janbu's Limit Equilibrium Method (LEM), pseudo-static method has been incorporated to analyze the influence of dynamic loads of blasting on slope stability. The horizontal loads produced by blast vibrations cause an increase in sliding forces, and this leads to a lower slope stability coefficient. When the tensile stresses of the two adjacent blast holes are greater than the tensile strength of rock mass, the radial oriented cracks are formed, which is the precondition for the formation of presplit face. Thus, the formula for calculating the blast hole spacing of presplit blasting can be obtained. Based on the analysis of the principles of vibration tester and vibration pick-up in detecting blast vibrations, a detection scheme of blast vibration is worked out by taking the blast area with precrack rear and non-precrack side of the detection object. The detection and research results of blast vibration show that presplit blasting can reduce the attenuation coefficient of stress wave by half, and the vibration absorption ratio could reach 50.2%; the impact of dynamic loads on the end-wall slope stability coefficient is 1.98%, which proves that presplit blasting plays an important role in shock absorption of blast casting.

## 1. Introduction

Blasting operation, the initial step in open-pit mining, may break the ores into fragments so that they can be mined and loaded by excavating equipment. However, this operation might create environmental impacts such as air overpressure, ground vibration, fly-rocks, and back-break around the blasting zone [1–3]. Blast casting in open cast mines is usually associated with high bench, large hole diameter, and large explosive charge. More than 30% stripping materials are cast into mined-out area, as a result, the operation of surplus overburdens in mining, loading, and hauling can be relatively reduced, resulting in a reduction in stripping costs and transportation costs. Based on the operation features of mining and loading equipment, the stripping technology composed of blast casting with dragline displays evident economic advantages among various mining technologies as blast casting is applied in rock breaking step. The shift and transportation of surplus material can be realized with the

coordinated application of dragline stripping equipment. The total number of blast holes in a high bench blast casting can be more than 500. The explosive charge in one hole is between 1.8t and 2.7t, and the aggregate explosive load reaches 900t to 1500t. High bench blast casting may not only cause strong vibration effect and affect large area, but also exert severe influences on surrounding buildings and pit slope [4, 5]. Consequently, controlling the vibration effects of blast casting and reducing the negative effects are of great importance to maintaining the regular production and work safety in open cast mines [6, 7].

The effective blast energy used for breaking and casting rocks only accounts for 20% to 30% of the gross energy, and the rest of the energy is distributed to producing fly-rocks, causing vibration effect and dissipating into the air. Vibration velocity of rock mass particles is an important indicator for describing the intensity of vibration effect. Explosive volume, charge position, explosive type, detonation direction, and charge structure directly affect the vibration

TABLE 1: Basic information of the minable coal seam.

Coal measure era	Coal seam type	Thickness of coal seam		Coal seam spacing	Coal seam structure	Stability
		Min~max	Average/m			
Taiyuan formation	6	6I	0.10 ~ 12.65	0 ~ 9.58	Complex	Unstable
			2.78	1.13		
		6II	0.05 ~ 7.71	0 ~ 9.58 , 0 ~ 5.46	Complex	
	3.26	1.13 , 0.25				
	6III~VI	0.50 ~ 27.19	0 ~ 5.46	Complex	Relatively stable	
			22.76	0.25		

strength [8]. Therefore, millisecond blasting together with the detonation direction is often adopted to control the ignition charge over the same period. Presplit blasting is often used to control the blast vibration effect and mitigate disasters caused by vibrations. Changing the charge structure is also a conventional method [9–11], with which presplit blasting can exert positive effects on shock absorption and reduce detonation wave propagation since it is able to form presplit cracks with a definite width and depth before the detonation of the main blast hole. This leads to termination of the transmission of detonating waves. Presplit cracks cause reflection and refraction on stress waves causing the stress wave energy transmitted into rock mass within protection zones to be reduced [12, 13]. Cai and Ma conducted a series of research on vibration reduction mechanism of presplit blasting with the application of joint stiffness model and stress wave theory. The research proved that the vibration absorption effect can be improved through increasing the length and depth of presplitting cracks [14]. Zou studied the vibration reduction result of presplit blasting with in situ investigation and figured out that the closer the presplit crack was, the better the vibration reduction results were obtained [15]. Salmi and Hosseinzadeh analyzed the mechanism of presplit blasting with the help of numerical simulation and determined that tensile stress waves induced by the denotation of two adjacent blast holes are the primary cause of presplit cracks [16]. Yang launched tests on trial blast holes with cross hole method and ultrasonic waves and established that presplit blasting might cause less damage to the rock mass in the slope than loosening blasting [17]. Sun et al. conducted some research on vibration effect of blast casting and its influences [18, 19]. Zhang and Song concluded and analyzed the practical experience of adopting presplitting blast in Heidaigou open cast mine and demonstrated that presplitting plays an important role in reducing blast vibration and maintaining the structure of rock mass in the slope [20, 21].

Presplit blasting is a major method to reducing the vibration effect of blast casting in higher bench and is of great significance to ensuring safety in blasting and production of open cast mines. Based on the characteristics of vibration effects and the vibration reduction mechanism of presplit blasting, the effects of presplit blasting on blast casting are analyzed on the basis of the study on the detection of results of blast vibration.

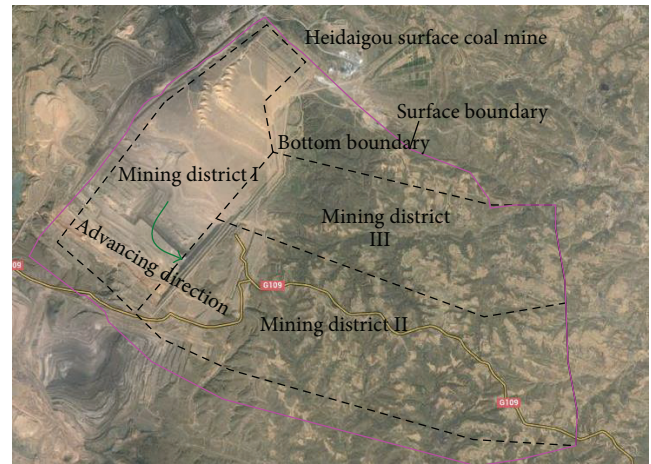


FIGURE 1: Mining district division and current exploitation status of Heidaigou open cast mine.

## 2. Engineering Geology of the Experimental Area

Heidaigou open cast mine is located in the southeastern part of Zhungeer Coalfield in Erdos Plateau. The average strike length of the mining range is 7.86 km and the width is 5.39 km, resulting in a gross area of 42.36 km<sup>2</sup>. Most coals mined within this area are long flame coal with the characteristics of ultra-low-phosphorous, low-sulfur, and medium- or high-ash-fusion-point. The minable coal seam in Heidaigou is the 6th composite coal seam with thick-layer and massive structure; the average thickness is 28.8 m and dipping less than 10°. Table 1 shows the basic information of the minable coal seam. The aggregate amount of minable coals within the boundary reaches 149.77 million tons. The zone is divided into three mining districts. At present, it is in the transitional period from primary mining district to secondary mining district, as shown in Figure 1.

By adopting loosening blasting, the upper soil and rock of Heidaigou open cast are broken and fragmented into pieces to be excavated and loaded by shovels and then transported to an internal dump by self-discharging truck. With the application of blast casting in the rocks above the coal seam roof within the scope of 40~50 m, more than 30% of the materials can be casted into the mined-out section and the surplus materials are disposed with a dragline. The strata of

TABLE 2: Main characteristic parameters of rock stratum in the blasting area.

Lithology	Rock density ( $\gamma$ )	Rock mass velocity ( $v_{rm}$ )	Rock wave velocity ( $v_r$ )	Integrity coefficient ( $K_i$ )	Crack coefficient ( $K_c$ )	Wave impedance ( $R$ )	Blastability
Mudstone	2.7 g/cm <sup>3</sup>	1273 m/s	3744 m/s	0.12	0.88	$3.44 \times 10^3$ g/cm <sup>3</sup> ·m/s	Medium
Sandstone	2.3 g/cm <sup>3</sup>	796~1118 m/s	1586~3226 m/s	0.06~0.5	0.5~0.99	$2.2 \times 10^3$ g/cm <sup>3</sup> ·m/s	Easy

Note: the integrated coefficient of rocks is determined by the square of the ratio of rock mass velocity to rock wave velocity,  $K_i = (v_{rm}/v_r)^2$ ; the crack coefficient of rocks,  $K_c = (V_r^2 - V_{rm}^2)/V_r^2$ ; the wave impedance of rocks,  $R = \gamma \cdot v_{rm}$ .

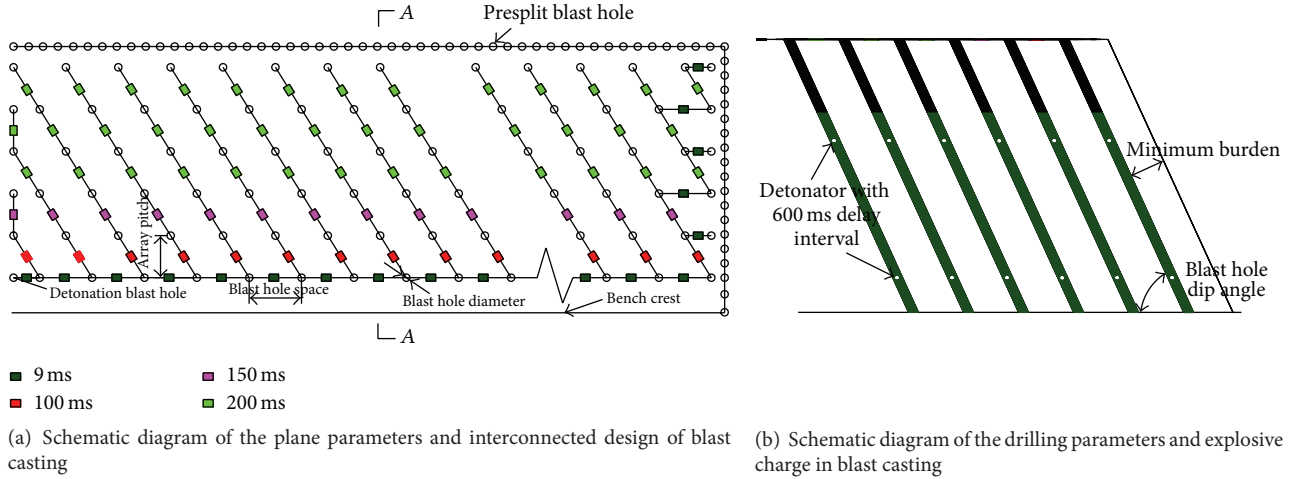


FIGURE 2: The schematic diagram of blast casting parameters.

the blast casting area are mainly composed of sandstone and mudstone, and the main characteristic parameters of rock strata are shown in Table 2 [22].

The blast hole diameter for blast casting in Heidaigou open cast is 310 mm, the blast hole spacing is 9~12 m, the array pitch is 7~9 m, the plunge of blast hole ranges from 65° to 70°, the unit explosive consumption is 0.7~0.9 kg/m<sup>3</sup>, and the minimum burden is 6~6.5 m. In order to control the detonation charge over the same period, hole-by-hole millisecond initiation control technology is adopted, the interhole delay is 9 ms, the interarray delay is 100~200 ms, and the time delay in holes is 600 ms [23]. Presplit blasting is adopted ahead of the detonation of main blast hole so that the impacts of blast vibrations on slope stability on high benches can be reduced. The result is commendable, as shown in Figure 2.

### 3. Vibration Effects of Blast Casting and Vibration Absorption Mechanism of Presplit Blasting

**3.1. Vibration Effect of Blast Casting and Its Impact on Slope Stability.** The displacement, velocity, and acceleration of particle motion caused by blasts are three factors for describing blast vibration strength. Moreover, since the critical safety values of acceleration and displacement are within a relatively wide limit, velocity of blast vibration naturally becomes the most important parameter for determining the destruction-bearing capacity of the medium. According to

Sadov's empirical formula, the velocity of blast vibration can be determined as [24]

$$v = \frac{k}{\sqrt[3]{f(n)}} \left( \frac{\sqrt[3]{Q}}{R} \right)^\alpha, \quad (1)$$

$$f(n) = 0.4 + 0.6n^3,$$

where  $v$  is the velocity of blasting vibration, cm/s;  $Q$  is the maximum explosive charge ignited over the same period, kg;  $R$  is the distance between blasting source center and guard point, m;  $\alpha$  is attenuation coefficient of seismic wave related to geological conditions,  $\alpha = 1$  to 3;  $k$  is medium parameter related to rock properties and blasting methods,  $k = 50$ ~200;  $f(n)$  is the exponential function of the blasting effect;  $n$  is the index of the blasting effect.

According to wave theory, it can be assumed that blasting seismic wave is composed of several simple harmonic waves with different amplitudes and different vibration frequencies [25]:

$$\begin{aligned} X &= \sum_i A_i \sin(\omega_i t), \\ V &= \sum_i \omega_i A_i \cos(\omega_i t + \varphi_{i1}), \\ a &= \sum_i \omega_i^2 A_i \sin(\omega_i t + \varphi_{i1}), \end{aligned} \quad (2)$$

where  $X$  is displacement, cm;  $V$  is vibration velocity, cm/s;  $a$  is vibration acceleration, cm/s<sup>2</sup>;  $A_i$  is blasting vibration

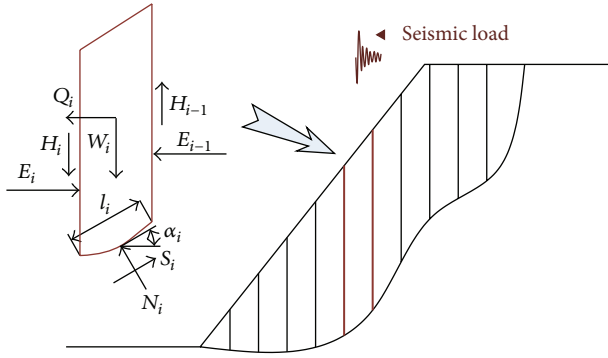


FIGURE 3: Force diagram on noncircular slip surface with slices based on Janbu Method.

amplitude, cm;  $\omega_i$  is circular frequency,  $\omega = 2\pi f$ , Hz;  $t$  is time, s;  $\varphi_{i1}$  and  $\varphi_{i2}$  denote phase differences.

High bench is applied in blast casting with the blast parameters of deep and large blast hole diameter. The rock volume blasted each time and the explosive consumption is huge. Blast vibration effect is a significant factor affecting slope stability of open cast mines. When calculating slope stability affected by blasting dynamics with pseudo-static method, it is usually assumed that the horizontal loads of blasting vibration exerted on the slope slip mass are equivalent to static loads [26]:

$$\begin{aligned} Q_i &= K_s W_i, \\ K_s &= \frac{K_D a_i}{g}, \end{aligned} \quad (3)$$

where  $E_{i-1}$  and  $E_i$  are the normal forces of the  $i$ th slice;  $H_{i-1}$  and  $H_i$  are the vertical shear stresses of the  $i$ th slice;  $N_i$  and  $S_i$  are the vertical reactions and shear forces on the slipping surface, respectively;  $l_i$  is the slice's bottom length of the sliding surface of the  $i$ th slice;  $c_i$  is cohesive force of the  $i$ th slice;  $\varphi_i$  is the internal angle of friction of the  $i$ th slice;  $F_s$  is the factor of safety.

It can be seen from Figure 3 and (7) that the horizontal load produced by blast vibration on the slip mass and the sliding component caused by gravity together constitute the sliding force of the slip mass. The factor of safety of the slope that has been affected by blast vibration is reduced compared to rock masses that are not affected.

**3.2. Vibration Absorption Mechanism of Presplit Blasting.** Blast casting in high bench of open cast mines causes the production of large blasting volume and devastating shock; it can cause relatively severe effects on slope stability of adjacent rock masses which have not been blasted. But as a special method for blasting control, presplit blasting can be very effective in reducing blast vibrations. This is achieved by

where  $Q_i$  is the equivalent static load, N;  $K_s$  is seismic load coefficient;  $a_i$  is vibration acceleration,  $m/s^2$ ;  $W_i$  is the slice weight of sliding mass, N;  $g$  is gravitational acceleration,  $m/s^2$ ;  $K_D$  is reduction coefficient of blasting dynamics whose value range is 0.008~0.152.

According to the schematic diagram for noncircular slip surface shown in Figure 3, the following equation based on Janbu's theory and the equilibrium condition of slice can be obtained [27]:

$$\begin{aligned} \sum Y &= 0, \\ W_i + H_i - H_{i-1} - N_i \cos \alpha_i - S_i \sin \alpha_i &= 0 \\ \sum X &= 0, \\ E_i - E_{i-1} + S_i \cos \alpha_i - N_i \sin \alpha_i - Q_i &= 0. \end{aligned} \quad (4)$$

According to Mohr's-Coulomb criterion, the shear force on the bottom sliding surface should meet the following condition:

$$S_i = \frac{c l_i}{F_s} + N_i \frac{\tan \varphi}{F_s}. \quad (5)$$

Based on the balance of forces of the whole landslide,

$$\sum (W_i + H_i - H_{i-1}) \tan \alpha_i - \sum S_i \sec \alpha_i + \sum Q_i = 0. \quad (6)$$

Combining (4), (5), and (6), the following factor of safety equation is obtained:

$$F_s = \frac{\sum (\sec^2 \alpha_i / (1 + \tan \alpha_i \tan \varphi_i / F_s)) [c_i l_i \cos \alpha_i + (W_i + H_i - H_{i-1}) \tan \varphi_i]}{\sum (W_i + H_i - H_{i-1}) \tan \alpha_i + \sum Q_i \cos \alpha_i}, \quad (7)$$

detonating the explosive charge placed in the presplit hole of the main blasting area and then separating the rock masses from original ones after cracks are formed along the blasting area boundary. In this way, the damages caused by blast vibrations on the original rock masses can be reduced.

The necessary condition to ensure the success of presplit blasting is that the pressure of the explosion in the blast holes will not damage the wall of the hole and the presplit crack will develop along the predetermined direction. According to stress wave interference theory [28–30], stress waves of each explosion spread radically after the denotation of two adjacent presplit holes as shown in Figure 4.

After the charge is denoted, the peak of the stress wave front weakens as the propagation distance of the stress wave increases with the attenuation formula [31, 32]:

$$\begin{aligned} P_R &= P_D \left( \frac{r_1}{R} \right)^\alpha, \\ P_D &= \frac{1}{k+1} \rho D^2 \left( \frac{r_1}{r_2} \right)^{-2k} n, \end{aligned} \quad (8)$$

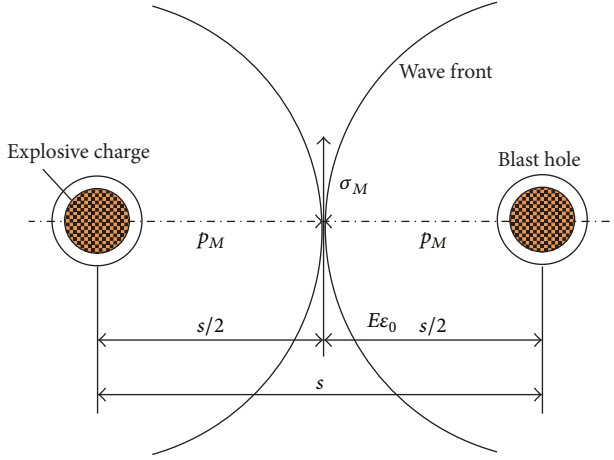


FIGURE 4: Wave front of two adjacent blast holes.

where  $P_R$  is the pressure of stress wave front after the detonation of explosive charge, Pa;  $r_1$  is the radius of blast hole, m;  $R$  is the distance between the center of blast hole and a certain point on the wave front, m;  $\alpha$  is the attenuation coefficient,  $\alpha = 2 - \mu/(1 - \mu)$ ;  $\mu$  is Poisson's ratio;  $P_D$  is the pressure on the wall of the holes, Pa;  $\rho$  is explosive density,  $\text{kg/m}^3$ ;  $D$  is explosive speed, m/s;  $r_2$  is the radius of explosive, m;  $k$  is adiabatic exponent;  $n$  is the multiple of pressure increase of the explosive gas colliding with the blast hole wall, and  $n = 8 \sim 11$ .

The stress wave causes radical displacement of the rock mass between two adjacent blast holes, while the radical displacement derives the tangential stresses and tangential strains. The tangential stress  $\sigma_T$  can be expressed as [33]

$$\sigma_T = \frac{\mu}{1 - \mu} P_R. \quad (9)$$

If the tangential stress on the wall of the hole is greater than the rock tensile strength  $\sigma_t$ , the initial crack on the wall of the blast hole will appear. Resulting from the stress wave of two adjacent blast holes, the sum  $\sigma_M$  of the tangential stress in the middle of the line connecting the two adjacent blast holes ( $R = s/2$ ) is

$$\sigma_M = \frac{2\mu}{(1 - \mu)(k + 1)} \rho D^2 \left( \frac{r_1}{r_2} \right)^{-2k} n \left( \frac{2r_1}{s} \right)^\alpha. \quad (10)$$

Similarly, if the tensile stress produced by blasting  $\sigma_M$  is greater than the tensile strength of rocks, that is,  $\sigma_M \geq \sigma_t$ , radial cracks appear along the lines connecting blast holes, which creates condition for the formation of the presplit face. The high pressure gas of explosion of the two adjacent blast holes then acts on the walls of the hole, thereby forming a quasi-static stress field around the blast holes. When the high pressure gas wedges in the initial crack of hole wall, there is a great tensile stress along the line connecting blast holes. The tensile stress concentration is all sides of the walls of the hole. A free surface with a certain width is formed which can exert positive effects towards the reduction in vibrations.

Therefore, the important precondition for the formation of the presplit face is that tension waves can produce tension crack. Based on (10), the formula of the blast hole spacing in presplit blasting should be

$$s \leq \frac{2r_1}{\left[ \sigma_t \left( (1 - \mu)(k + 1) / 2\mu\rho D^2 n \right) \left( r_1/r_2 \right)^{2k} \right]^{1/\alpha}}. \quad (11)$$

Low density ANFO explosive is used as a presplit blast explosive in Heidaigou open cast with a density of  $200 \text{ kg/m}^3$ , a speed of  $1950 \text{ m/s}$ , a presplit blast hole diameter of  $310 \text{ mm}$ , charge diameter of  $150 \text{ mm}$ , and a unit explosive consumption of  $0.85 \text{ kg/m}^3$ . According to (11), the optimum blast hole spacing of presplit blasting is estimated as ranging from  $3.03 \text{ m}$  to  $4.16 \text{ m}$ , with  $3.5 \text{ m}$  selected for application. Figure 5 shows the presplit blasting effect. The cracks formed from the blast are relatively intact with an even width and the ratio of the half hole to the total presplit hole is a little higher.

The transmission coefficient of stress wave is

$$R_t = \frac{A_t}{A_i}, \quad (12)$$

where  $R_t$  is the transmission coefficient and  $A_i$  and  $A_t$  are the amplitude of incident wave and the amplitude of transmitted wave, respectively.

The wave velocity expression is

$$v = A e^{-\alpha} \sin \omega t \quad (13)$$

and the vibration absorption ratio of presplit blasting is

$$\varepsilon = \frac{|v_i|_{\max} - |v_t|_{\max}}{|v_i|_{\max}} = \frac{|A_i|_{\max} - |A_t|_{\max}}{|A_i|_{\max}} = 1 - R_t. \quad (14)$$

## 4. Detection and Analysis of Vibration Produced by Blast Casting

**4.1. The Detection Principles of Blast Vibration.** Detection system of blast vibration is composed of the blast vibration tester and the vibration pick-up. As the vibration wave is transmitted to the vibration pick-up, induced voltage outputs are generated and once the induced voltage signal exceeds the preset triggering level, the tester automatically records and saves the vibration signals loaded by the sensor. After detecting the vibration signals, the blast vibration waves can be read and analyzed with the connection and communication between special software and vibration tester. The principle diagrams of the detection system and the measuring point layout are shown in Figures 6 and 7, respectively.

Based on the inspection data, the regression analysis should be carried out with Sadov's empirical formula and the formula of vibration velocity attenuation can thus be obtained.

**4.2. Detection Scheme of Blast Vibration.** In order to record the whole vibration process and the attenuation law of blasting seismic waves, the detection scheme of blast vibration is



FIGURE 5: Presplit blasting effect pictures of surface coal mine.

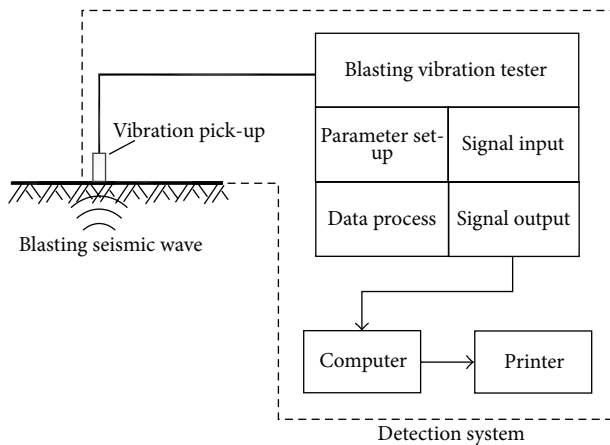


FIGURE 6: The principle diagram of the detection system.

worked out according to the characteristics of blast casting and the geological and topographic conditions of the blasting zone. Detection points are set on the same bench and kept in a straight line on the right side of the blasting zone without presplit blast. Another set of detection points are also set on the same bench in a straight line on the rear blasting zone with presplit blast. Both of the above-mentioned detection points are used to monitor the seismic intensity and variations of blast vibrations.

The blast vibration tester adopted here is a vibration signal recorder whose model is UBOX-20016, the maximum sampling rate of which is 200 KSps/CH and the signal resolution is 16 bits (1/65536 of the measuring range). The vibration pick-up is CD-21 magnetolectric vibration velocity sensor with the sensitivity of 200 mv/cm/s, and the error is less than 3%. The installation of sensors is based on the measurement of vibration velocity in different directions and the sensors must be firmly bonded to the ground by gypsum powder.

The primary detection area of blast vibration is the rear part and the broadside of the blasting zone: the former is with presplit cracks and the latter is without. Therefore, the effect of presplit cracks in vibration reduction can be proved by comparison. Blast vibration recorder is used for inspecting the velocity of particles in vertical direction (V-), radial direction (R-), and transverse direction (T-). Figure 8 shows the schematic diagram of detection point layout.

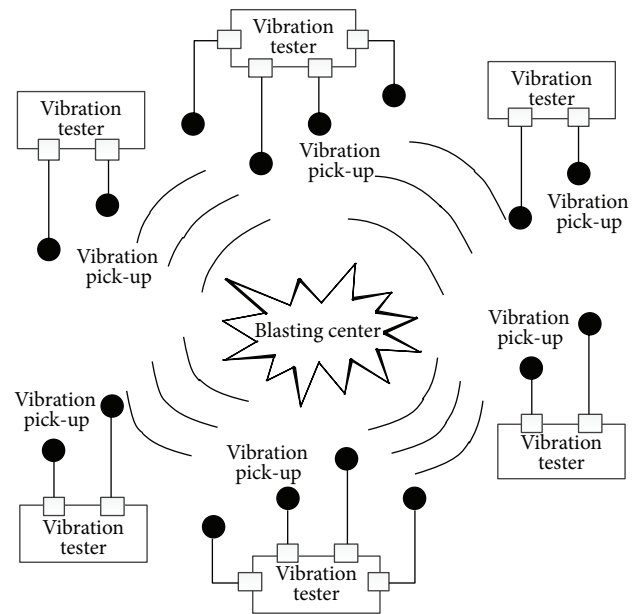


FIGURE 7: The schematic diagram of the measuring point layout.

**4.3. Analysis on the Detection Results of Blasting Vibration.** In all cases, blast vibration detection has been carried out three (3) times. The gross explosive loads (GEL) for each time are  $9.6 \times 10^5$  kg,  $7.8 \times 10^5$  kg, and  $1.3 \times 10^6$  kg, respectively. The maximum explosive charges per delay interval (MECPDE) are  $1 \times 10^4$  kg,  $1.5 \times 10^4$  kg, and  $1.5 \times 10^4$  kg, respectively, and the explosive charge per blast hole is  $2 \times 10^3$  kg. The distance between each detection point and the blasting source (DDPBS) as well as the vibration velocity of the largest particle are shown in Table 3.

Standard blast casting is adopted in Heidaigou open cast, and the blasting acting index  $n = 1$ . Based on (1) and the detection data, the attenuation equations for blast vibration in presplit blasting and non-presplit blasting are obtained by fitting:

$$v = \begin{cases} 95.18 \left( \frac{\sqrt[3]{Q}}{R} \right)^{1.34}, & R^2 = 0.959 \text{ (presplit blast)} \\ 221.61 \left( \frac{\sqrt[3]{Q}}{R} \right)^{1.40}, & R^2 = 0.795 \text{ (non-presplit blast)}. \end{cases} \quad (15)$$

TABLE 3: Location of detection points and blast vibration strength.

Detection point	T- mm/s	V- mm/s	R- mm/s	Resultant mm/s	DDPBS m	GEL kg	MECPDE kg	Remarks
H1-2	14.1	11.1	10.8	17.4	350	960000	10000	Back
H1-3	10.4	16.8	7.8	17.9	550	960000	10000	Back
H1-4		4.3	9.9	10	800	960000	10000	Back
H1-5	1.7	2.3	3.8	3.9	1215	960000	10000	Back
H1-6	1.1	1.9	2.8	2.9	1800	960000	10000	Back
H2-1	104.7	149.7	124.3	181.3	100	780000	15000	Back
H2-2	31.7	56.5	32.7	55	200	780000	15000	Back
H2-3	11.8	17.3	16.3	20.4	300	780000	15000	Back
H2-4	10.8	13.9		18.7	500	780000	15000	Back
H2-5	4.5	3.9	3.7	7.9	800	780000	15000	Back
H2-6	4.2	2.5	2.3	5.4	1000	780000	15000	Back
H2-7	17.4	30	22	41.1	380	780000	15000	Back
H3-1	66.7	69.4	59.8	87.4	162	1300000	15000	Back
Y1-1	28.6	13.5	29.1	30.3	574.9	960000	10000	Right
Y1-2	19.6	12.1	30.6	31.1	604.6	960000	10000	Right
Y1-3	12.6	5.59	12.4	14.5	800	960000	10000	Right
Y1-4	8.51	3.05	8.51	10.3	826.6	960000	10000	Right
Y3-1	65.6	70.9	70.8	118	200	1300000	15000	Right
Y3-2	23.3	28	25.5	50.7	350	1300000	15000	Right
Y3-4	10.1	5.8	—	17.5	550	1300000	15000	Right
Y3-5	6.5	2.4	3.7	10.7	650	1300000	15000	Right

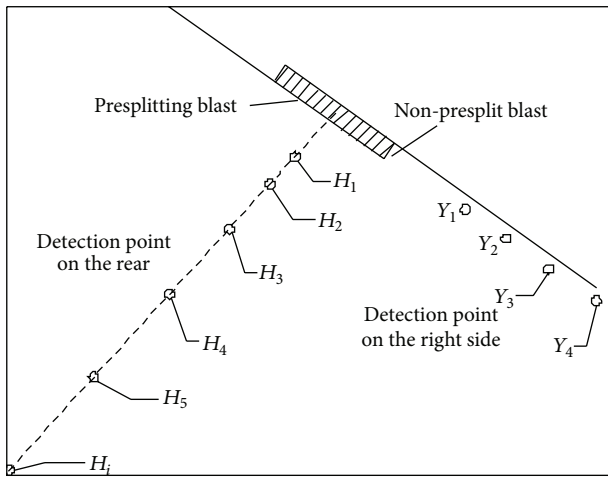


FIGURE 8: Location of the blast detection point and blast vibration source.

According to (15), the attenuation indices under these two conditions are nearly the same, that is, 1.34 and 1.40, respectively. However, the attenuation coefficient might be reduced by half when adopting presplit blasting. Because of the application of hole-by-hole millisecond detonation, the maximum explosive charge per segment is less than  $1.1 \times 10^4$  kg, and the vibration velocity of the end-wall slope is 2.53 cm/s. In addition, the equation for calculating the acceleration of blast vibration is [34]

$$a = 0.028Q^{0.83}R^{-3.5}C_p^2, \quad (16)$$

where  $a$  is acceleration of the blast vibration,  $m/s^2$ ;  $C_p$  is the longitudinal wave velocity,  $m/s$ ; other symbols are consistent with the former expressions.

The transmission velocity of blast vibration in sandstone rock mass is 1118  $m/s$ , the acceleration is calculated as  $1.21 m/s^2$  (16), and the seismic load coefficient of blasting is calculated as 0.012 (3). According to the mechanical parameters of rock mass of Heidaigou open cast listed in Table 4, the factors of stability of the end-wall slope are calculated as 1.311 for the condition of static load and 1.285 for the condition of dynamic load, respectively. Therefore, the effect of dynamic load on factor of safety of the end wall is merely 1.98%.

Meanwhile, the resultant vibration velocities of different detection points are shown in Table 5. As the distance between detection points and blasting centers increases, the vibration velocities decrease exponentially under the condition of both presplit blasting and non-presplit blasting. A closer distance to the blasting center can better reflect the vibration reduction effect of presplit blasting. When the detection point is 200 m away from the blasting center, the vibration absorption ratio is increased to 50.2%, which implies that presplit blasting can effectively absorb vibrations.

## 5. Conclusions

(1) Pseudo-static method has converted the dynamic load of blast vibration to equivalent static load, and Janbu LEM has been used to analyze the influence of blast vibration on slope stability. The horizontal load caused by blast vibration enhances the sliding force of the slip mass and therefore

TABLE 4: Mechanical parameters of rock mass of Heidaigou open cast.

Stratum	Density (kN/m <sup>3</sup> )	Internal friction angle (°)	Cohesion (kPa)
Loess	19.50	29.5	45.1
Sandy mudstone	24.50	30	135
Fine sandstone	24.50	28	150
Medium sandstone	22.70	31.5	150
Coarse sandstone	22.40	32.0	130
Weathered mudstone	24.7	29.0	127.5
Coal	14	35	185.1
Siltstone	24.5	31.3	176.8

TABLE 5: Actual blast vibration detection data and absorption shock rate of presplit blasting.

Detection point distance to blasting center/m	Velocity of vibration/cm·s <sup>-1</sup>						
	200	400	600	800	1000	1200	1400
Presplit blasting	5.48	2.21	1.3	0.89	0.66	0.52	0.43
Non-presplit blasting	11.01	3.97	2.18	1.43	1.03	0.79	0.63
Vibration reduction ratio	50.2%	44.3%	40.4%	37.8%	35.9%	34.2%	31.7%

reduces the factor of safety. Calculated results suggest that slope stability factors on conditions of static load and dynamic load of blasting are 1.311 and 1.285, respectively, and the dynamic load of blast casting has slight effect on the end slope stability, taking only 1.98%.

(2) After the detonation of two adjacent presplit holes, stress waves of each explosion spread radially and create tangential stress in the tangential direction. Based on the theory of stress wave interference, when the sum of the tangential stress of two adjacent blast holes is greater than the rock tensile strength, radial cracks come into being along the line connecting blast holes, which creates condition for the formation of the presplit face. Based on the above condition, the blast hole spacing in presplit blasting is obtained. Accordingly, the blast hole spacing of presplit blasting of Heidaigou open cast mine ranges from 3.03 m to 4.16 m, with 3.5 m used in actual production, satisfying the presplit blasting effect.

(3) The vibration detection principles of vibration testers and pick-ups are analyzed. The vibration velocity of blasting particle is detected in the blasting zone whose rear part is with presplit cracks, and right side is without. Based on Sadov's empirical formula, attenuation formulas of blast vibration on conditions with and without presplit blasting are obtained by numerical fitting, respectively. The detection results indicate that presplit blasting can reduce the attenuation coefficient by half, and the vibration absorption ratio can reach 50.2%, which means presplitting blast is of great significance in shock absorption of blast casting.

## Competing Interests

The authors declare that there are no competing interests regarding the publication of this paper.

## Acknowledgments

This study was supported by the National Natural Science Foundation of China (51034005), the Fundamental

Research Funds for the Central Universities (2010QNB23, 2011QNB25), and the Priority Academic Program Development of Jiangsu Higher Education Institutions.

## References

- [1] K. Pathak, S. Durucan, and S. Kunimatsu, "Activity accounting technique for environmental noise assessment in mechanized surface mining," *Environmental Monitoring and Assessment*, vol. 56, no. 3, pp. 241–256, 1999.
- [2] A. Fişne, C. Kuzu, and T. Hüdaverdi, "Prediction of environmental impacts of quarry blasting operation using fuzzy logic," *Environmental Monitoring and Assessment*, vol. 174, no. 1–4, pp. 461–470, 2011.
- [3] D. J. Armaghani, E. Momeni, S. V. A. N. K. Abad, and M. Khandelwal, "Feasibility of ANFIS model for prediction of ground vibrations resulting from quarry blasting," *Environmental Earth Sciences*, vol. 74, no. 4, pp. 2845–2860, 2015.
- [4] T. N. Singh and V. Singh, "An intelligent approach to prediction and control ground vibration in mines," *Geotechnical and Geological Engineering*, vol. 23, no. 3, pp. 249–262, 2005.
- [5] U. Ozer, A. Kahriman, M. Aksoy, D. Adiguzel, and A. Karadogan, "The analysis of ground vibrations induced by bench blasting at Akyol quarry and practical blasting charts," *Environmental Geology*, vol. 54, no. 4, pp. 737–743, 2008.
- [6] C. Kuzu and E. Guclu, "The problem of human response to blast induced vibrations in tunnel construction and mitigation of vibration effects using cautious blasting in half-face blasting rounds," *Tunnelling and Underground Space Technology*, vol. 24, no. 1, pp. 53–61, 2009.
- [7] D. D. Li and Z. D. Deng, "Evaluation of the effects of blasting vibration on humans in the excavation of CMICT dock," *Engineering Blasting*, vol. 12, no. 2, pp. 82–85, 2012.
- [8] F. Zheng, W. D. Duan, D. W. Zhong, and B. Y. Sun, "Research progress and existing problems of blasting vibration," *Blasting*, vol. 23, no. 1, pp. 92–94, 2006.
- [9] T. L. Shi and B. Z. Li, "The effects of millisecond delay interval, charge distribution and measuring distance on blasting vibration," *Engineering Blasting*, vol. 9, no. 4, pp. 10–13, 2003.

- [10] Y. L. Gao, Q. Tan, S. C. Yang, L. Xue, and Y. L. Yu, "Experimental research on relationship between charge layout and blasting vibration," *Engineering Blasting*, vol. 10, no. 3, pp. 19–48, 2004.
- [11] Ö. Uysal and M. Cavus, "Effect of a pre-split plane on the frequencies of blast induced ground vibrations," *Acta Montanistica Slovaca*, vol. 18, no. 2, pp. 101–109, 2013.
- [12] J. L. Yan and X. F. Chen, "Observation and analysis of vibration reduction effect of pre-split crack in complicated geologic condition," *Blasting*, vol. 25, no. 3, pp. 100–102, 2008.
- [13] A. J. Prakash, P. Palroy, and D. D. Misra, "Analysis of blast vibration characteristics across a trench and a pre-split plane," *Fragblast*, vol. 8, no. 1, pp. 51–60, 2004.
- [14] L. J. Cai and J. J. Ma, "The shock absorption mechanism and its effect analysis of pre-splitting blasting," *China Mining Magazine*, vol. 14, no. 5, pp. 56–58, 2005.
- [15] Y. F. Zou, "Experimental study on the vibration- isolating effect of pre-split crack and vibration-isolating slot," *Blasting*, vol. 22, no. 2, pp. 96–99, 2005.
- [16] E. F. Salmi and S. Hosseinzadeh, "A further study on the mechanism of pre-splitting in mining engineering," *Applied Mechanics and Materials*, vol. 553, pp. 476–481, 2014.
- [17] N. H. Yang, "Experimental study on rock damage in the slope caused by presplit blasting," *Journal of the China Railway Society*, vol. 30, no. 3, pp. 96–99, 2008.
- [18] H. R. Sun, Y. J. Tong, X. L. Lin, and H. S. Gao, "Study on the Vibration Effect of sling blasting in an open coal mine," *Blasting*, vol. 25, no. 1, pp. 69–73, 2008.
- [19] Q. K. Chen, G. C. Li, and K. M. Li, "Monitor and analysis on explosive seismic effect of high-bench cast blast of surface coal mine," *Explosive Materials*, vol. 37, no. 6, pp. 30–33, 2008.
- [20] P. K. Zhang and F. G. Song, "Pre-splitting blasting applied in high-bench cast blasting," *Opencast Mining Technology*, no. 1, pp. 35–41, 2007.
- [21] P. K. Zhang, "Application of pre-splitting blasting in high-bench cast blasting of Heidaigou open pit," *Inner Mongolia Science Technology & Economy*, no. 6, pp. 257–258, 2008.
- [22] W. M. Hu, "Black dai ditch open-pit coal mine rock wave velocity testing technology," *Journal of North China Institute of Science and Technology*, vol. 11, no. 9, pp. 63–67, 2014.
- [23] X. H. Ding, K. M. Li, S. S. Xiao, and W. M. Hu, "Analysis of key technologies and development of integrated digital processing system for cast blasting design," *Journal of Central South University*, vol. 22, no. 3, pp. 1037–1044, 2015.
- [24] C. G. Jin, "Vibrating effect of blasting in open-pit slope," *Metal Mine*, no. 5, pp. 18–20, 1995.
- [25] Q. Liu and S. R. Lv, "Research on the millisecond delay interval time of open-pit bench blasting," *Engineering Blasting*, vol. 20, no. 1, pp. 54–58, 2014.
- [26] M. Chen, W. Lu, D. Shu, and C. Zhou, "Calculation method of equivalent acceleration for limit equilibrium analysis of slope under blasting vibration," *Chinese Journal of Rock Mechanics and Engineering*, vol. 28, no. 4, pp. 784–790, 2009.
- [27] B. He and Y. Wang, "Residual thrust method and Janbu method used to calculate landslide stability," *Safety and Environmental Engineering*, vol. 11, no. 4, pp. 60–62, 2004.
- [28] Y. L. Yu, *Theory and Technology of Engineering Blasting*, Metallurgical Industry Press, Beijing, China, 2004.
- [29] W. M. Ling, "A study on the fracture mechanism of smooth blasting and pre-split blasting," *Journal of China University of Mining & Technology*, vol. 19, no. 4, pp. 79–87, 1990 (Chinese).
- [30] M. Sazid and T. N. Singh, "Numerical assessment of spacing-burden ratio to effective utilization of explosive energy," *International Journal of Mining Science and Technology*, vol. 25, no. 2, pp. 291–297, 2015.
- [31] B. F. Li and C. B. Qi, "Shaped crack mechanism and parameters design of pre-splitting blasting," *West-China Exploration Engineering*, no. 3, pp. 78–79, 2000 (Chinese).
- [32] Q. Zong, "Theoretical analysis of charge structure's influence on pressure on bore wall," *Mining and Metallurgical Engineering*, vol. 26, no. 5, pp. 9–12, 2006 (Chinese).
- [33] K. S. Ge, *Study on Parameter of Pre-Splitting Blasting*, China University of Geosciences, Beijing, China, 2009.
- [34] J. G. Wang, L. F. Luan, Z. Y. Zhang, X. L. Li, and C. L. Fan, "Numerical simulation of blasting vibration effect on stability of high-steep slope," *Blasting*, vol. 29, no. 3, pp. 119–122, 2012.

## Research Article

# Analysis and Numerical Simulation on the Reduction Effect of Stress Waves Caused by Water Jet Slotting Near Blasting Source

Dengfeng Su,<sup>1</sup> Yong Kang,<sup>1,2</sup> Dongyang Li,<sup>1</sup> Xiaochuan Wang,<sup>1,2</sup> and Fuwen Yan<sup>1</sup>

<sup>1</sup>State Key Laboratory of Coal Mine Disaster Dynamics and Control, Chongqing University, Chongqing 400044, China

<sup>2</sup>Hubei Key Laboratory of Waterjet Theory and New Technology, Wuhan University, Wuhan 430072, China

Correspondence should be addressed to Yong Kang; kangyong@whu.edu.cn

Received 4 November 2015; Revised 31 March 2016; Accepted 21 April 2016

Academic Editor: Shimin Liu

Copyright © 2016 Dengfeng Su et al. This is an open access article distributed under the Creative Commons Attribution License, which permits unrestricted use, distribution, and reproduction in any medium, provided the original work is properly cited.

As one of the most serious “side effects” of blast excavation, blast-induced vibration must be controlled for existing buildings and human beings. This paper proposes a method for blast-induced vibration reduction with water jet assistance according to the cutting characters of low-noised, environment-friendly water jet. The mechanism of vibration-isolation with water jet assistance was analyzed, and the stress wave energy attenuation models were established based on blasting theory and stress wave theory. Influence law on shock wave attenuation by vibration-isolation slot was studied by numerical simulation. Simulation results agree with the theoretical analysis roughly. The results of this study put forward a method for blast-induced vibration near blasting source and provide a certain theoretical basis.

## 1. Introduction

With the development of China's economy, the demand for energy and space is increasingly rapid. Therefore, a growing number of large underground space projects have been put into construction. As the most popular method for rock excavation, drilling-blasting method is still an indispensable means in engineering construction. However, it has been proved that only 20~30% of energy released by explosives is used for rock fragmentation during blasting; the rest appears in the form of ground vibration, air blast, fly rock, noise, and back break [1–3]. Among all the “side effects” of blasting, ground vibration, posing a serious threat to existing building structures, is a major concern to designers and environmentalists [4–6]. So it is very important and meaningful to reduce blast-induced vibration.

Generally, the methods for reducing blast-induced vibration include the following ones. The first solution is to adopt millisecond blasting or to decrease explosive charge per delay. Millisecond blasting technique has been verified as

a promising strategy in mitigating the PPV level and a great number of analysis models and methods for blast signals have been carried out [7–10]. The method for decreasing explosive charge per delay may also affect particle size after blasting or production rate [11, 12]. Adding sacrificial cladding in the borehole is the second solution. Guruprasad and Mukherjee [13] proposed layered mild steel plates employed to dissipate or absorb blast energy, and the impulse distributions and energy absorptions in plastic deformation of the mild steel plates were studied. Theobald and Nurick [14] studied the responses of tube-core claddings under blast loads by experiments, whose results showed that panel crush distance increases with increasing impulse and decreases with an increasing number of tubes in the panel core. Palanivelu et al. [15] studied crushing and energy absorption performance of different geometrical shapes of small-scale glass polyester composite tubes under quasistatic loading conditions and found that the corresponding energy absorption of the special geometrical shapes was better than that of the standard square and hexagonal geometrical shapes. Tarlochan et al.

[16] conducted quasistatic compression experimental investigation of composite sandwich cladding structures fabricated from glass fiber, polystyrene foam, and epoxy resin. Zhao et al. [17] proposed a foamed cement-based composite functional material as sacrificial cladding to provide the blast mitigation effect and investigated its response with different ingredient proportions and determined the optimized thickness of foamed cement-based sacrificial cladding.

On the other hand, forming artificial discontinuity functions as a barrier to stress wave transmission is another solution. The artificial discontinuity can be presplit, barrier hole, and a trench. For presplit blasting, Lu et al. [18] studied the vibration isolating mechanism and effect of presplit crack. Lou and Long [19] conducted the field test to study the effect of the presplit in propagation of blasting seismic waves, with the result showing that damping effect of the presplit is related with the distance between the presplit and the point of the seismic wave data collected, and the damping ratio will be in the range of 15%~30%. Luo et al. [20] studied the relation between the effect of presplitting crack on damping vibration and the length, depth of presplitting crack, and distance between presplitting crack and blasting source by matlab software. For trench blasting, Fourney et al. [21] investigated the effects of joints and bedding planes on seismic vibration, revealing that as thickness of discontinuity increased, seismic vibration decreased between blasting point and measurement station. Song [22] explained the essence of decreasing vibration methods by energy-origin, energy-transfer media, and energy-transfer process. Kattis et al. [23] examined that an open trench was more effective for decreasing vibration than a filled one by research on open and concentrate-filled trenches. Prakash et al. [24] studied effect of trench on vibration level and reported vibration reduction of 16–55%. Adam and Von Estorff [25] opened trenches near railways and achieved reduction in vibration of up to 80%. Bogunovic and Kecojevic [26] experimentally studied the influence on vibration reduction by different combinations of artificial screen sizes and positions with blasting source and measurement point, making vibration reduce by 30–58%. Ak and Konuk [7] researched impacts of discontinuity frequency parameter derived through geological measurements. The mechanism of blasting seism is complicated with numerous influencing factors. Zhang et al. [27] studied controlling factors of blasting seismic effect by grey correlation theory of grey system and pointed out that the superdeep drilling and pore network parameters are the controlling factors of seismic effect. Uysal et al. [11] conducted a series of field experiments to investigate the effect of barrier holes on blast-induced vibration, and the results revealed that a decrease in PPV of up to 18% has been detected just behind the barrier holes. Park et al. [28] studied the influence on screening effectiveness by the spacing and diameter of drilling holes and obtained the design details for field application by numerical simulation. Gao et al. [29] studied the vibration-isolation from three dimensions and analyzed the relevant parameters; the results revealed that the reductions are generally more efficient for smaller separation between piles, and the increasing length of piles

has a great influence on the reduction of the surface wave field.

Regarding the above studies, it can be concluded that the essence of most common methods for blast-induced vibration reduction is to decrease the initial energy of stress wave or to change stress wave propagation path. Therefore, the method for blast-induced vibration reduction with water jet assistance was put forward by combining with the unique advantages of high-pressure water jet, such as no wear and tear, no spark, energy concentration, and directional cutting. Then, the mechanism of vibration-isolation with water jet assistance was analyzed, and the stress wave energy attenuation models were established based on blasting theory and stress wave theory. Finally, FEM software ANSYS/LS-DYNA was used to verify the validity of the theoretical results and qualitatively obtain their influence rules on blast-induced vibration effect.

The differences between the present study and the research performed by other researchers are as follows:

- (1) The method for blast-induced vibration reduction with water jet assistance is designed to weaken the effect that stress waves have on the protected objects and is applicable for the occasion in which the protected objects are in the vicinity of blasting source. However, the present technologies aim at weakening the effect that blasting seismic waves have on the protected objects, and, generally comparing with the former method, the work field is further from the protected objects.
- (2) This paper focuses on the shock wave energy reduction, while all the above-mentioned researches put emphasis on the seismic wave isolation. In this paper, the model of energy of stress wave was established and demonstrated by FEM software of ANSYS/LS-DYNA.

## 2. Experimental Study of Hard Rock Cutting by Water Jet

Hard rock is a common material and also is an intractable material for the construction of oriented slot and the VIS, since buildings must be constructed on the solid foundation. Therefore, test experiment on cutting hard rock by water jet was conducted to obtain the suitable work parameters. The test system is a set of hard rock cutting experimental system with water jet assistance according to principle of water jet technique. Its schematic diagram is shown in Figure 1. In this experiment, four cone convergent nozzles were adopted. Their convergences are  $17^\circ$ . And their diameters are 2.0 mm, 2.5 mm, 3 mm, and 3.5 mm, respectively. The experimental sample ( $1\text{ m} \times 1\text{ m} \times 0.5\text{ m}$  in size) is a mixture of sand, cement, and water (mass ratio 1.2:1:2) and is air-dried for 28 days, as shown in Figure 2. The sample has a uniaxial compressive strength of 89 MPa, uniaxial tensile strength is 17 Mpa, and its Protodikonov hardness coefficient is 9.

A series of tests have been performed to obtain the relationship between the size of water jet slot and cutting time, pump pressure, and the nozzle diameter. The water

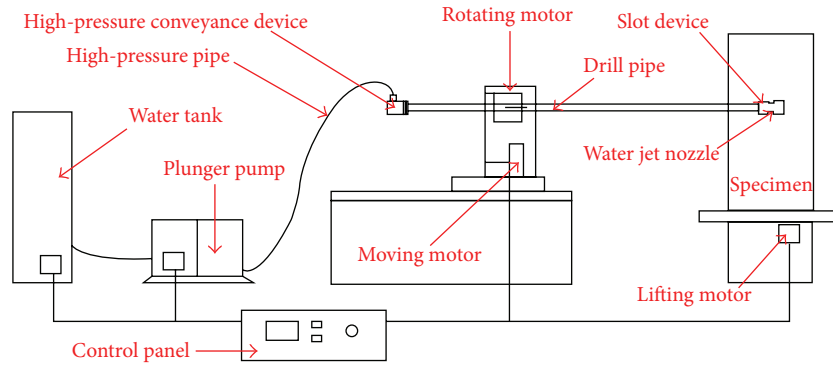


FIGURE 1: Schematic diagram of water jet test system.



FIGURE 2: Test specimen.



FIGURE 3: Water jet.

jet was shown in Figure 3. Depth and width of water jet cutting under each condition are shown in Figures 4 and 5, respectively. As it can be seen from the two figures, with the increase of pump pressure, water jet cutting depth and water jet cutting width increase obviously. Nevertheless, with the increase of pump pressure, growth rate of water jet cutting depth is different. When nozzle diameter is 2.0 mm, water jet cutting depth is 0.1566 m and 0.4242 m under the condition of pressure of 10 MPa and 28 MPa, and the maximum cutting depth is increased by 170.88%. And when nozzle diameter is 3.5 mm, water jet cutting depth is 0.1123 m and 0.1722 m, the maximum cutting depth is increased by 53.34%.

On the other hand, with the increase of nozzle diameter, the water jet cutting depth decreases while the water jet cutting width increases. That is because the divergence segment width of water jet increases while the energy of core section of water jet decreases with the increase of nozzle diameter.

### 3. Mechanism of Blast-Induced Vibration Reduction Assisted by Water Jet

**3.1. Method for Vibration-Isolation with Assistance of Water Jet Slot.** The process of blast-induced vibration reduction with water jet assistance can be divided into the following parts. First, drill boreholes according to design scheme. Second, use water jet to make oriented slots in the surface of the periphery

boreholes along the excavation outline. Finally, drill empty holes between the periphery boreholes and the protected objects, and construct the vibration-isolation slot (VIS) with water jet. Its technical sketch was shown in Figure 6.

Previous studies have proved that the slot at the sides of the periphery boreholes can generate stress concentration in the process of explosion and function as a guidance of blasting energy, expanding blast-induced cracks along the excavation outline and reducing stress in other directions. In addition, the VIS can change the propagation path of stress wave, sharply reducing the energy of stress wave which acts on protected object so as to achieve directional fracture and blast-induced vibration reduction.

**3.2. Energy Attenuation Models of Stress Wave.** Stress wave energy attenuates in the process of propagation and has different attenuation coefficients in the different media. Furthermore, different kinds of stress waves experience attenuation in different degrees [30, 31]. In this paper, major energy attenuation caused by the VIS was focused on and divided into three parts. The first part is the energy dissipating in the form of reflected wave at the first interface between rock and the VIS, which can be expressed by  $E_1$ . The second is energy dissipating during the propagation of stress wave in the VIS and can be expressed by  $E_2$ . The third is the energy dissipating in the form of reflected wave at the second interface between rock and the VIS and can be expressed by  $E_3$ . Assume  $E_t$  is the total energy reduced by VIS, it can be written as follows:

$$E_t = E_1 + E_2 + E_3. \quad (1)$$

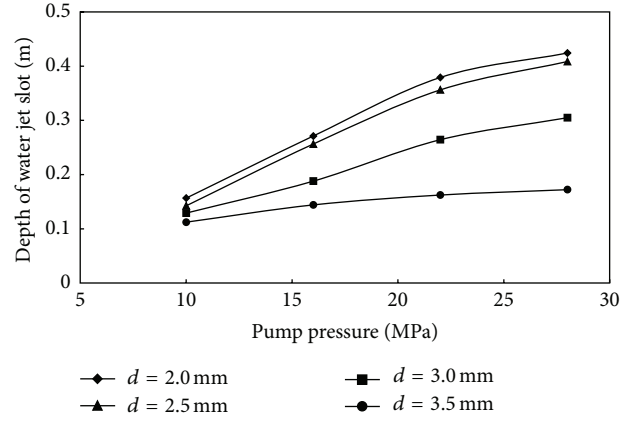


FIGURE 4: Curve of cutting depth of water jet.

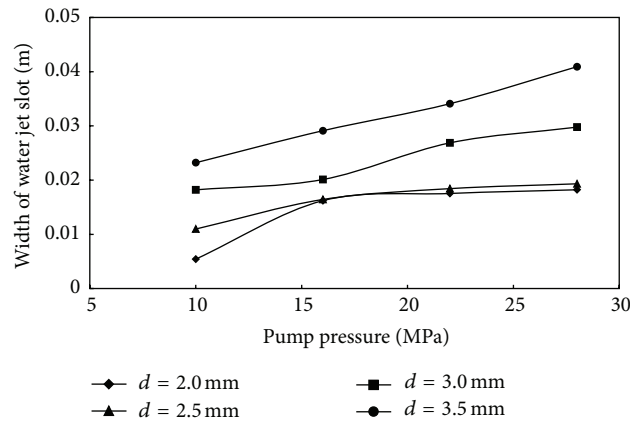


FIGURE 5: Curve of cutting width of water jet.

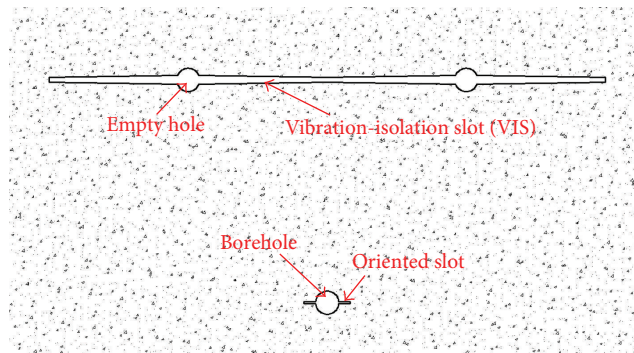


FIGURE 6: Technical sketch of blast-induced vibration reduction with water jet assistance.

According to elasticity theory [32, 33], stress wave energy can be calculated by

$$E = \frac{1}{\rho C} \int_{t_1}^{t_2} \sigma^2 dt, \quad (2)$$

where  $E$  is the stress wave energy,  $\rho$  is density of the medium,  $C$  is the velocity of stress wave in the medium,  $t_1$  is the start time that stress wave starts to act on the medium,  $t_2$  is the end time that stress wave stops acting on the medium, and  $\sigma$  is the stress that acts on the medium.

On the basis of the above analysis of the energy characters of stress wave in the process of propagation, when the VIS is located in the shock wave zone and assuming that the rock was not crushed by explosive shock wave, the relationship between the initial pressure of shock wave produced by explosive and the pressure of shock wave arriving at the VIS can be written as follows:

$$P_1 = \sigma_r = P_0 \left( \frac{d}{r_0} \right)^{-2-\mu/(1+\mu)}, \quad (3)$$

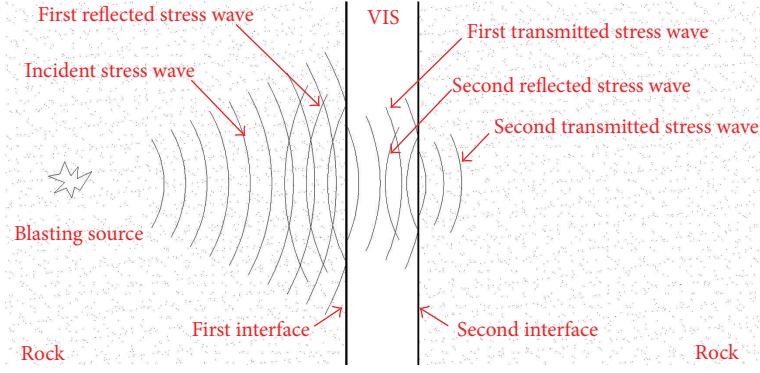


FIGURE 7: Schematic diagram of stress wave propagation.

where  $P_0$  is the initial pressure of shock wave produced by explosive,  $d$  is the distance from explosion source,  $\mu$  is Poisson ratio of rock, and  $P_1$  is the pressure of shock wave arriving at the VIS.

According to blasting theory, if the charge structure of borehole is coupled, the initial pressure of shock wave produced by explosive can be calculated by Formula (4); if the charge structure is uncoupled, the initial pressure of shock wave produced by explosive can be calculated by Formula (5) [34]:

$$P_0 = \frac{2\rho_2 C_2}{\rho_e \nu_D + \rho_2 C_2} P_d, \quad (4)$$

$$P_0 = \frac{1}{8} \rho_e \nu_D^2 \left( \frac{V_c}{V_b} \right)^3 n, \quad (5)$$

where  $\rho_2$  is the density of rock,  $\rho_e$  is the density of explosive,  $\nu_D$  is detonation velocity of explosive,  $P_d$  is detonation pressure of explosive, and  $C_2$  is sound velocity of rock.  $V_c$  is volume of explosive package,  $V_b$  is volume of explosive compartment, and  $n$  is magnification factors and its value is 8~11.

In addition, reflection and transmission occur at the interface when stress wave encounters the VIS. Its schematic diagram was shown in Figure 7. And the relationship between incident wave and reflected wave can be written as [34, 35]

$$\begin{aligned} \sigma_{R_1} &= \frac{\rho_2 C_2 - \rho_1 C_1}{\rho_2 C_2 + \rho_1 C_1} \sigma_I \\ &= P_0 \left( \frac{d}{r_b} \right)^{-2-\mu/(1+\mu)} \frac{\rho_2 C_2 - \rho_1 C_1}{\rho_2 C_2 + \rho_1 C_1}, \\ \sigma_{T_1} &= \frac{2\rho_1 C_1}{\rho_2 C_2 + \rho_1 C_1} \sigma_I \\ &= P_0 \left( \frac{d}{r_b} \right)^{-2-\mu/(1+\mu)} \frac{2\rho_1 C_1}{\rho_2 C_2 + \rho_1 C_1}, \end{aligned} \quad (6)$$

where  $\sigma_I$  is incident stress,  $\sigma_{R_1}$  is reflected wave stress,  $\sigma_{T_1}$  is transmitted wave stress,  $\rho_1$  is density of material filling the

VIS,  $\rho_2$  is density of rock,  $C_1$  is sound velocity of material filling the VIS, and  $C_2$  is sound velocity of rock.

Combining with the above formulas, when the VIS is located in the shock wave zone and the charge structure of borehole is coupling charge, then the shock wave energy attenuation caused by the VIS can be calculated by Formula (7). And when the VIS is located in the shock wave zone and the charge structure is uncoupled charge, then the shock wave energy attenuation caused by the VIS can be calculated by Formula (8):

$$\begin{aligned} E_{\text{tsh}} &= \frac{4\rho_2 C_2 (\rho_2 C_2 - \rho_1 C_1)^2}{(\rho_e \nu_D + \rho_2 C_2)^2 (\rho_2 C_2 + \rho_1 C_1)^2} (P_d)^2 \\ &\cdot \int_0^{t_4} (\xi_1)^2 \left( \frac{d}{r_b} \right)^{-4-2\mu/(1+\mu)} dt \\ &+ \frac{16(\rho_2 C_2)^2 \rho_1 C_1}{(\rho_e \nu_D + \rho_2 C_2)^2 (\rho_2 C_2 + \rho_1 C_1)^2} (P_d)^2 \\ &\cdot \int_0^{t_5} \left( \frac{d}{r_b} \right)^{-4-2\mu/(1+\mu)} dt \\ &+ \frac{64(\rho_1 C_1)^2 \rho_2 C_2}{(\rho_e \nu_D + \rho_2 C_2)^2 (\rho_2 C_2 + \rho_1 C_1)^4} (P_d)^2 \\ &\cdot \int_0^{t_6} (\xi_1)^2 \left( \frac{d}{r_b} \right)^{-4-2\mu/(1+\mu)} dt, \\ E_{\text{tsh}} &= \frac{(\nu_D)^4 (\rho_e n)^2 (\rho_2 C_2 - \rho_1 C_1)^2}{64\rho_2 C_2 (\rho_2 C_2 + \rho_1 C_1)^2} \left( \frac{V_c}{V_b} \right)^6 \\ &\cdot n^2 \int_0^{t_4} (\xi_1)^2 \left( \frac{d}{r_b} \right)^{-4-2\mu/(1+\mu)} dt \\ &+ \frac{(\nu_D)^4 (\rho_e n)^2 \rho_1 C_1}{16(\rho_2 C_2 + \rho_1 C_1)^2} \left( \frac{V_c}{V_b} \right)^6 \int_0^{t_5} \left( \frac{d}{r_b} \right)^{-4-2\mu/(1+\mu)} dt \end{aligned} \quad (7)$$

$$\begin{aligned}
& + \frac{(\nu_D)^4 (\rho_e n)^2 (\rho_1 C_1)^2}{4\rho_2 C_2 (\rho_2 C_2 + \rho_1 C_1)^4} \left(\frac{V_c}{V_b}\right)^3 \\
& \cdot \int_0^{t_6} (\xi_1)^2 \left(\frac{d}{r_b}\right)^{-4-2\mu/(1+\mu)} dt,
\end{aligned} \tag{8}$$

where  $E_{\text{tsh}}$  is shock wave energy attenuation caused by the VIS,  $\xi_1$  is stress attenuation function of reflected shock wave,  $t_4$  is the time it takes the first reflected shock wave to act on rock,  $t_5$  is the time it takes transmitted shock wave to propagate through VIS, and  $t_6$  is the time it takes second reflected shock wave to act on rock.

In the same way, when the VIS is located in compressive wave zone, the relationship between the initial pressure of shock wave produced by explosive and the pressure of compressive wave arriving at the VIS can be written as follows:

$$P_2 = \sigma_r = P_0 \left(\frac{d}{r_0}\right)^{-2+\mu/(1-\mu)}, \tag{9}$$

where  $P_2$  is compressive pressure.

Therefore, when the VIS is located in the compressive wave zone and the charge structure of borehole is coupling charge, the compressive wave energy attenuation by VIS can be calculated by Formula (10). And when the VIS is located in the compressive wave zone and the charge structure of borehole is coupling charge, the compressive wave energy attenuation by VIS can be calculated by Formula (11):

$$\begin{aligned}
E_{\text{tco}} &= \frac{4\rho_2 C_2 (\rho_2 C_2 - \rho_1 C_1)^2}{(\rho_e \nu_D + \rho_2 C_2)^2 (\rho_2 C_2 + \rho_1 C_1)^2} (P_d)^2 \\
& \cdot \int_0^{t_7} (\xi_2)^2 \left(\frac{d}{r_b}\right)^{-4+2\mu/(1-\mu)} dt \\
& + \frac{16\rho_1 C_1 (\rho_2 C_2)^2}{(\rho_e \nu_D + \rho_2 C_2)^2 (\rho_2 C_2 + \rho_1 C_1)^2} (P_d)^2 \\
& \cdot \int_0^{t_8} \left(\frac{d}{r_b}\right)^{-4+2\mu/(1-\mu)} dt \\
& + \frac{64\rho_2 C_2 (\rho_1 C_1)^2}{(\rho_e \nu_D + \rho_2 C_2)^2 (\rho_2 C_2 + \rho_1 C_1)^4} (P_d)^2 \\
& \cdot \int_0^{t_9} (\xi_2)^2 \left(\frac{d}{r_b}\right)^{-4+2\mu/(1-\mu)} dt, \\
E_{\text{tco}} &= \frac{(\rho_e n)^2 (\nu_D)^4 (\rho_2 C_2 - \rho_1 C_1)^2}{64\rho_2 C_2 (\rho_2 C_2 + \rho_1 C_1)^2} \left(\frac{V_c}{V_b}\right)^6 \\
& \cdot \int_0^{t_7} (\xi_1)^2 \left(\frac{d}{r_b}\right)^{-4+2\mu/(1-\mu)} dt
\end{aligned} \tag{10}$$

$$\begin{aligned}
& + \frac{(\rho_e n)^2 (\nu_D)^4 \rho_1 C_1}{16 (\rho_2 C_2 + \rho_1 C_1)^2} \left(\frac{V_c}{V_b}\right)^6 \\
& \cdot \int_0^{t_8} \left(\frac{d}{r_b}\right)^{-4+2\mu/(1-\mu)} dt \\
& + \frac{(\rho_e n)^2 (\nu_D)^4 (\rho_1 C_1)^2}{4\rho_2 C_2 (\rho_2 C_2 + \rho_1 C_1)^2} \left(\frac{V_c}{V_b}\right)^6 \\
& \cdot \int_0^{t_9} (\xi_1)^2 \left(\frac{d}{r_b}\right)^{-4+2\mu/(1-\mu)} dt,
\end{aligned} \tag{11}$$

where  $E_{\text{tco}}$  is compressive wave energy attenuation caused by the VIS,  $\xi_2$  is stress attenuation function of reflected compressive wave.  $t_7$  is the time it takes the first reflected compressive wave to act on rock,  $t_8$  is the time it takes transmitted compression wave to propagate through VIS,  $t_9$  is the time it takes the second reflected compressive wave to act on rock.

By analyzing Formula (7), Formula (8), Formula (10), and Formula (11), some conclusions can be drawn as bellow:

- (1) In Formula (7), except for  $d$ , other parameters can be seen as constants and they are greater than zero identically. On the contrary,  $-2 + \mu/(1 - \mu)$  is less than zero. Therefore, with the increase of  $d$ , the shock wave energy attenuation caused by the VIS decreases. Similarly, Formula (8), Formula (10), and Formula (11) share the same trend. In other words, the smaller the distance between borehole and VIS, the better the blast-induced reduction effect achieved.
- (2)  $(16(\rho_2 C_2)^2 \rho_1 C_1 / (\rho_e \nu_D + \rho_2 C_2)^2 (\rho_2 C_2 + \rho_1 C_1)^2) (P_d)^2 \int_0^{t_5} (d/r_b)^{-4-2\mu/(1+\mu)} dt$  stands for the energy dissipating during the propagation of stress wave in the VIS, and  $t_5$  is the time it takes transmitted shock wave to propagate through VIS. Therefore, with the increase of the width of VIS, the energy dissipating during this process increases, and the better blast-induced vibration reduction effect will be achieved.
- (3) The smaller the wave impedance of material filling VIS is, the bigger the stress wave energy attenuation of VIS is. In other words, the material with low wave impedance is suitable for the material filling VIS to achieve the good blast-induced vibration effect.

#### 4. Numerical Simulations

In this section, FEM software (ANSYS/LS-DYNA) was used for numerical simulation studies on blasting-induced vibration reduction effect influenced by the distance between VIS and borehole and the material filling VIS, which aims at verifying the validity of the theoretical results and qualitatively obtaining their influence rules on blast-induced vibration effect.

TABLE 1: Case defined.

Case number	$D$ (m)	Material filling the VIS	Material filling the oriented slot
1	0.1	Air	Air
2	0.2	Air	Air
3	0.3	Air	Air
4	0.4	Air	Air
5	0.5	Air	Air
6	0.1	Water	Air
7	0.2	Water	Air
8	0.3	Water	Air
9	0.4	Water	Air
10	0.5	Water	Air

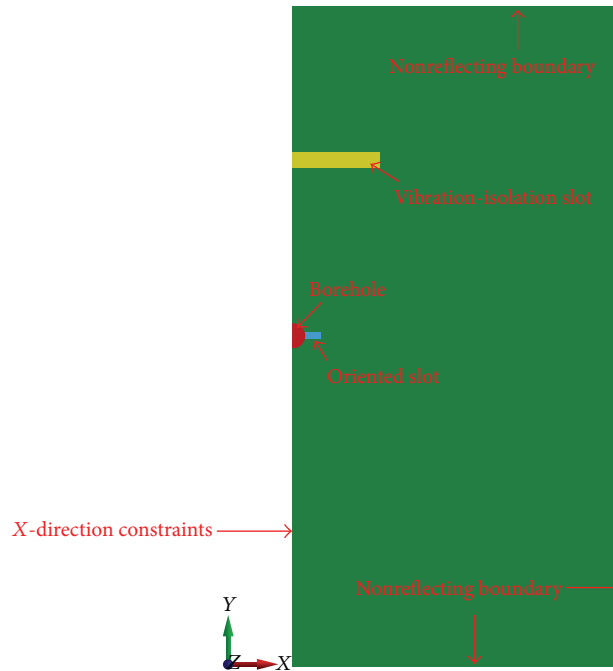


FIGURE 8: Numerical simulation model of Case 4.

**4.1. Simulation Model and Simulated Cases.** The blast-induced vibration reduction effect of area near blasting source is numerically simulated in ten different cases to compare the contribution of the VIS, in which we define  $D$  as the distance between VIS and borehole, and the ten cases are shown in Table 1.

Due to the symmetry of the simulated object, a half model with symmetrical constraints in  $X$  direction was applied. And in each case, rock is  $0.75 \text{ m} \times 1.5 \text{ m} \times 0.03 \text{ m}$  in size, borehole is  $0.05 \text{ m}$  in diameter, oriented slot is  $0.04 \text{ m} \times 0.03 \text{ m} \times 0.03 \text{ m}$  in size, and the VIS is  $0.2 \text{ m} \times 0.05 \text{ m} \times 0.03 \text{ m}$  in size. The simulation model of Case 4 is shown as in Figure 8.

To avoid the large deformation problem of explosive during the blasting process, fluid-solid coupling algorithm was adopted, in which ALE algorithm is used for explosive and material filling oriented slot, Lagrange algorithm for rock, and material filling VIS. At the same time, meshes of explosive and air filling oriented slot were joined with common nodes,

TABLE 2: Parameters of rock.

$\rho_2$ (kg/m <sup>3</sup> )	$E$ (MPa)	$P_R$	$Y_{\text{SIG}}$ (MPa)	$E_{\text{TAN}}$ (MPa)	$F_S$
$2.55 \times 10^3$	$2.25 \times 10^4$	0.22	3.24	$4.25 \times 10^3$	0.06

and the meshes of rock and the material filling VIS share the same nodes. Then, the fluid-solid coupling was defined by the keyword of `CONSTRAINED_LAGRANGE_IN_SOLID` [36].

On the other hand, according to the characteristics of blasting process, the time step of the simulation is 0.67, and the computation time is 0.002 s.

#### 4.2. Material Model

**4.2.1. Material Model for Rock.** According to experiment test on physical property of rock, material type 3 of LS-DYNA (\*MAT\_PLASTIC\_KINEMATIC) is suitable, and Table 2

TABLE 3: Parameters of explosive and its EOS equation.

$\rho_e$ (kg/m <sup>3</sup> )	$\nu_D$ (m/s)	$P_{\text{cut}}$ (MPa)	$A$ (MPa)	$B$ (MPa)	$R_1$	$R_2$	$\omega$
$1.93 \times 10^3$	$9.93 \times 10^3$	$3.37 \times 10^4$	$3.71 \times 10^5$	$7.43 \times 10^3$	4.15	0.95	0.30

TABLE 4: Parameters of air and its EOS equation.

$\rho_a$ (kg/m <sup>3</sup> )	$C_0$	$C_1$	$C_2$	$C_3$	$C_4$	$C_5$	$C_6$	$E_{a0}$	$V_{a0}$
$1.25 \times 10^3$	$-1 \times 10^{-6}$	0.00	0.00	0.00	0.40	0.40	0.00	$2.5 \times 10^{-6}$	1.0

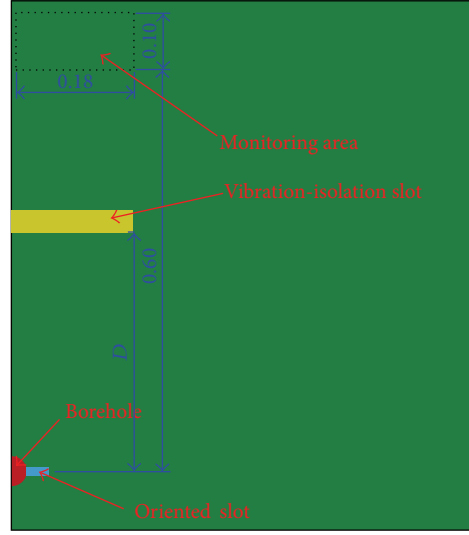


FIGURE 9: Layout of monitoring area.

gives its parameters, where  $\rho_2$  is density of rock,  $E$  is Young modulus,  $P_R$  is Poisson ratio of rock,  $Y_{\text{SIG}}$  is Yield stress of rock,  $E_{\text{TAN}}$  is Tangent modulus, and  $F_S$  is Failure strain for eroding elements [37].

**4.2.2. Material Model for Explosive.** Explosive was modeled by the material type 8 of LS-DYNA (\*MAT\_HIGH\_EXPLOSIVE\_BURN) [37], and the Jones-Wilkens-Lee (JWL) equation of state was used for the pressure applied by the detonation product gases. It can be calculated by

$$P_e = A \left( 1 - \frac{\omega}{R_1 V_e} \right) e^{-R_1 V_e} + B \left( 1 - \frac{\omega}{R_2 V_e} \right) e^{-R_2 V_e} + \frac{\omega E_e}{V_e}, \quad (12)$$

where  $P_e$  is pressure applied by the detonation product gases,  $\rho_e$  is density of explosive,  $\nu_D$  is detonation velocity of explosive,  $P_{\text{cut}}$  is Chapman-Jouget pressure,  $\omega$ ,  $A$ ,  $B$ ,  $R_1$ , and  $R_2$  are user defined input parameters,  $V_e$  is relative volume, and  $E_e$  is internal energy per initial volume, as shown in Table 3.

**4.2.3. Material Model for Air.** Air was modeled by material type 9 of LS-DYNA (\*MAT\_NULL) with LINEAR\_POLYNOMIAL equation, the pressure  $P_a$  can be calculated by [37]

$$P_a = C_0 + C_1 \mu + C_2 \mu^2 + C_3 \mu^3 + (C_4 + C_5 \mu + C_6 \mu^2) E_a, \quad \mu = \frac{1}{V_a} - 1, \quad (13)$$

where  $C_0$ ,  $C_1$ ,  $C_2$ ,  $C_3$ ,  $C_4$ ,  $C_5$ , and  $C_6$  are user defined constants,  $\rho_a$  is density of air,  $V_a$  is the relative volume,  $V_{a0}$  is the initial relative volume of air,  $E_a$  is internal energy, and  $E_{a0}$  is the initial internal energy of air, as shown in Table 4.

**4.2.4. Material Model for Water.** The water was modeled by the material type 9 of LS-DYNA (\*MAT\_NULL) with Gruneisen equation, the pressure  $P_w$  can be calculated by [37]

$$P_w = \frac{\rho_0 C^2 \mu [1 + (1 - \gamma_0/2) \mu - (a/2) \mu^2]}{[1 - (S_1 - 1) \mu - S_2 (\mu^2 / (\mu + 1)) - S_3 (\mu^3 / (\mu + 1)^2)]^2} + (\gamma_0 + a \mu) E_w, \quad \mu = \frac{\rho}{\rho_0} - 1, \quad (14)$$

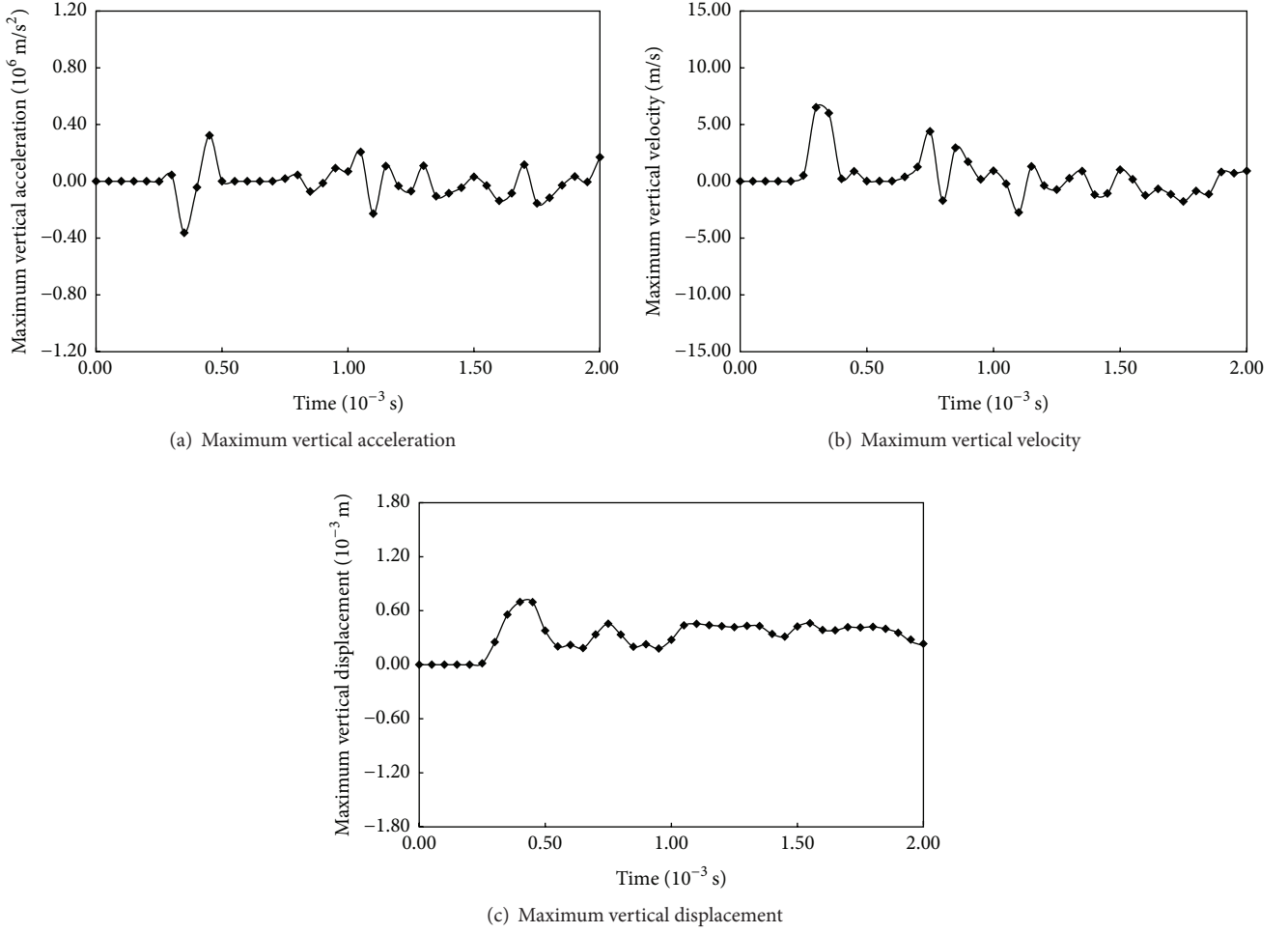


FIGURE 10: Blast-induced vibration parameters of Case 1.

where  $E_w$  is internal energy per initial volume,  $\rho_w$  is density of water,  $C$  is intercept of  $u_s-u_p$  curve,  $S_1$ ,  $S_2$ , and  $S_3$  are coefficients of the slope of the  $u_s-u_p$  curve,  $\gamma_0$  is the Gruneisen gamma,  $a$  is the first-order volume correction to  $\gamma_0$ , constants  $S_1$ ,  $S_2$ , and  $S_3$ ,  $\gamma_0$ , and  $a$  are all input parameters, and  $E_{w0}$  is the initial internal energy of water, as shown in Table 5.

#### 4.3. Numerical Results and Discussions

**4.3.1. Influence of Distance between VIS and Borehole.** The effect of varying the distance between borehole and VIS of the blast-induced vibration was investigated by varying the distance between borehole and VIS from 0.1 m to 0.5 m at 0.1 m intervals. Meanwhile, a rectangular region ( $0.1 \text{ m} \times 0.18 \text{ m}$ ) behind the VIS was set as monitoring area for blast-induced vibration condition of stress wave under each condition, as shown in Figure 9. The distance between monitored area and explosion source remained

TABLE 5: Parameters of water and its EOS equation.

$\rho_w \text{ (kg/m}^3\text{)}$	$C$	$S_1$	$S_2$	$S_3$	$E_{w0}$
$1.02 \times 10^3$	1.65	1.92	$-0.96 \times 10^{-1}$	0.00	0.00

0.6 m, and we define  $D$  as the distance between VIS and borehole. Then, the maximum vertical acceleration, maximum vertical velocity, and maximum vertical displacement in the monitored area under each condition were drawn in Figures 10–14.

Figures 10–14 show the blast-induced vibration parameters under each condition. Compared with the curves in Figures 10–14, with the increase of distance between the VIS and borehole, the vibration parameters almost show a linear increase. When the distance between the VIS and explosion source is 0.1 m, the maximum acceleration, maximum velocity, and maximum displacement are  $3.23 \times 10^5 \text{ m/s}^2$ , 6.52 m/s, and  $6.97 \times 10^{-4} \text{ m}$ , respectively. When the

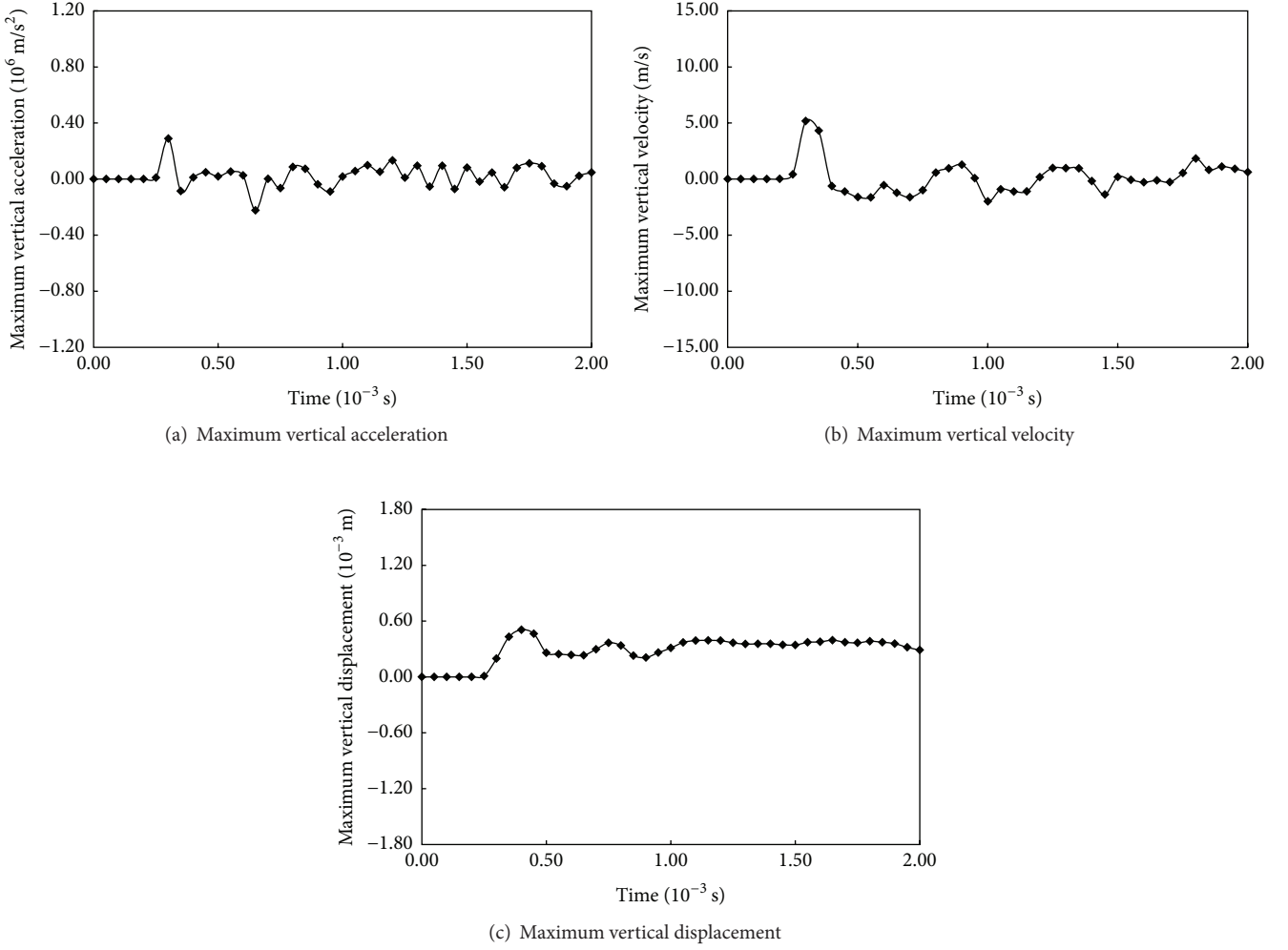


FIGURE 11: Blast-induced vibration parameters of Case 2.

distance between VIS and borehole is 0.5 m, the maximum acceleration, maximum velocity, and maximum displacement are  $9.92 \times 10^5 \text{ m/s}^2$ ,  $1.02 \times 10 \text{ m/s}$ , and  $1.66 \times 10^{-3} \text{ m}$ , respectively, and the parameters increase by 207.12%, 56.44%, and 138.16%, respectively. Particularly, compared with the vibration parameters under the condition of distance 0.1 m and vibration parameters under the condition of distance 0.2 m, the vibration parameters decrease with the increase of distance. When the distance between the VIS and borehole is 0.2 m, the maximum acceleration, maximum velocity, and maximum displacement decrease by 10.84%, 20.71%, and 27.4%, respectively. It is because the distance between VIS and borehole is too small, which leads to the rock being crushed by shock wave and sharply reducing the energy of shock wave after it goes through the VIS, as shown in Figure 15. Therefore, it can be concluded that when the distance between the protected objects and blasting source

remains certain, the smaller the distance is, the more efficient the blast-induced effect is. This is also confirmed by Section 3.

4.3.2. *Influence of Material Filling the VIS.* Attenuation ratio of vibration parameters can be calculated by [34]

$$\eta = \frac{c - d}{c} * 100\%, \quad (15)$$

where  $\eta$  is attenuation ratio,  $c$  is maximum blast-induced vibration parameter in front of VIS,  $d$  is maximum blast-induced vibration parameter behind VIS. The attenuation ratio of vibration parameters are shown in Tables 6 and 7, and the relationship between distance and attenuation ratio under each condition is shown in Figure 16.

TABLE 6: Attenuation ratio of vibration parameters (VIS filled with air).

Distance (m)	Velocity		Acceleration		Displacement				
	Maximum velocity in front of slot (m/s)	Maximum velocity behind slot (m/s)	Attenuation ratio (%)	Maximum acceleration in front of slot ( $m/s^2$ )	Maximum acceleration behind slot ( $m/s^2$ )	Attenuation ratio (%)	Maximum displacement in front of slot (m)	Maximum displacement behind slot (m)	Attenuation ratio (%)
0.1	$2.81 \times 10^{-1}$	$1.11 \times 10^{-2}$	96.07	$1.40 \times 10^{-2}$	$6.80 \times 10^{-4}$	95.14	2741	8.43	69.23
0.2	$1.51 \times 10^{-2}$	$3.10 \times 10^{-3}$	79.47	$1.20 \times 10^{-3}$	$1.98 \times 10^{-4}$	83.5	4.22	0.18	95.71
0.3	$8.10 \times 10^{-3}$	$1.94 \times 10^{-3}$	76.05	$1.18 \times 10^{-3}$	$2.80 \times 10^{-4}$	76.33	2.52	0.22	91.27
0.4	$6.10 \times 10^{-3}$	$1.65 \times 10^{-3}$	72.95	$8.20 \times 10^{-3}$	$2.40 \times 10^{-4}$	70.73	1.28	0.24	81.25
0.5	$4.10 \times 10^{-3}$	$1.10 \times 10^{-3}$	72.93	$5.20 \times 10^{-3}$	$1.80 \times 10^{-4}$	65.38	0.87	0.22	75.29

TABLE 7: Attenuation ratio of vibration parameters (VIS filled with water).

Distance (m)	Velocity		Acceleration				Displacement		Attenuation ratio (%)
	Maximum velocity in front of slot (m/s)	Maximum velocity behind slot (m/s)	Attenuation ratio (%)	Maximum acceleration in front of slot ( $m/s^2$ )	Maximum acceleration behind slot ( $m/s^2$ )	Maximum displacement in front of slot (m)	Maximum displacement behind slot (m)		
0.1	$9.12 \times 10^{-2}$	$7.51 \times 10^{-2}$	17.65	$0.26 \times 10^{-1}$	$1.85 \times 10^{-2}$	31.43	24.51	22.02	
0.2	$6.10 \times 10^{-3}$	$4.80 \times 10^{-3}$	21.31	$1.30 \times 10^{-3}$	$5.80 \times 10^{-4}$	0.81	0.59	27.16	
0.3	$6.20 \times 10^{-3}$	$3.89 \times 10^{-3}$	37.26	$8.90 \times 10^{-3}$	$4.10 \times 10^{-4}$	0.73	0.41	43.84	
0.4	$5.80 \times 10^{-3}$	$2.85 \times 10^{-3}$	50.86	$8.60 \times 10^{-3}$	$3.20 \times 10^{-4}$	0.64	0.28	55.94	
0.5	$4.20 \times 10^{-3}$	$2.09 \times 10^{-3}$	50.26	$5.80 \times 10^{-3}$	$2.23 \times 10^{-4}$	0.53	0.22	58.71	

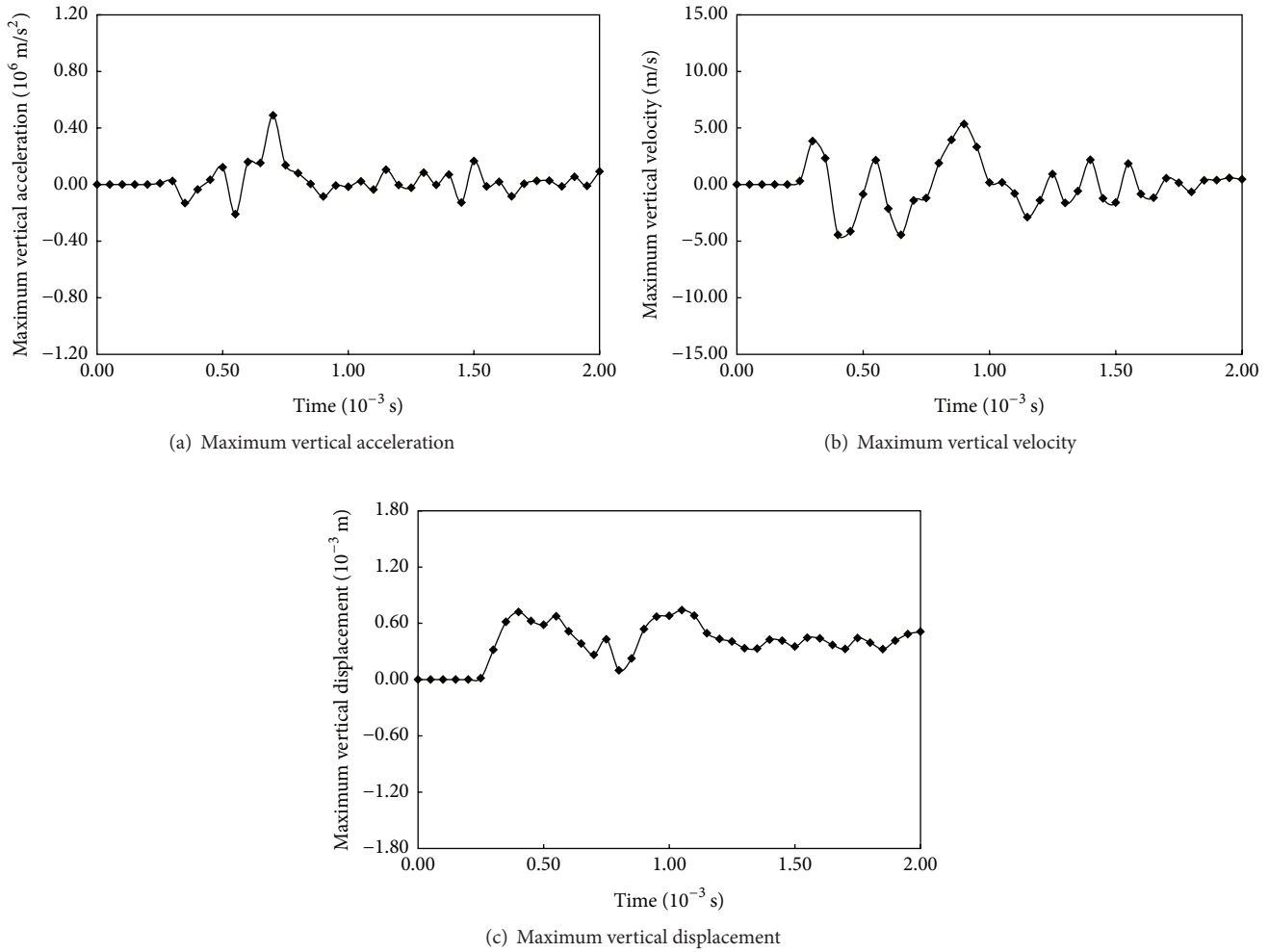


FIGURE 12: Blast-induced vibration parameters of Case 3.

Figure 16 shows the attenuation ratio of VIS under each condition. For the VIS filled with air, its attenuation ratio decreases with increase of distance between VIS and borehole. Particularly, with the increase of the distance between VIS and borehole, attenuation ratio of displacement shows a tendency to increase at first and then decrease. And for the VIS with water, its attenuation ratio increases with the increase of distance between VIS and borehole. These trends above agree with theoretical analysis roughly.

On the other hand, compared with Figures 16(a) and 16(b), attenuation ratio of vibration parameters caused by VIS filled with air is greater than that caused by VIS filled with water. When the distance from VIS to explosion source is 0.2 m, attenuation ratios of acceleration, velocity, and displacement caused by VIS filled with air are increased by 20.88%, 68.76%, and 71.63%, respectively, compared with those caused by VIS filled with water. The reason for that is because air is different from water in compressibility. Figures 17 and 18 present the evolution law

of shock wave when it propagated through the VIS. As it can be seen when shock wave propagate through VIS filled with air, reflection and transmission occur at the interface, shock wave energy sharply reduces, and shock wave form is also changed. However, when shock wave propagates through VIS filled with water, shock wave form is barely changed.

In addition, sharply reducing the distance between VIS and borehole is not a good choice to achieve good directional blasting effect and blast-induced vibration reduction effect. This is because if the distance from VIS to explosion source is too short, the rock will be crushed by shock wave when the reflected wave stress exceeds the dynamic tensile strength of rock and because the process can further affect the directional blasting effect by oriented slot, just as shown in Figure 17. Therefore, it is necessary to set the suitable distance and choose material filling VIS so as to achieve good directional blasting effect and blast-induced vibration reduction effect.

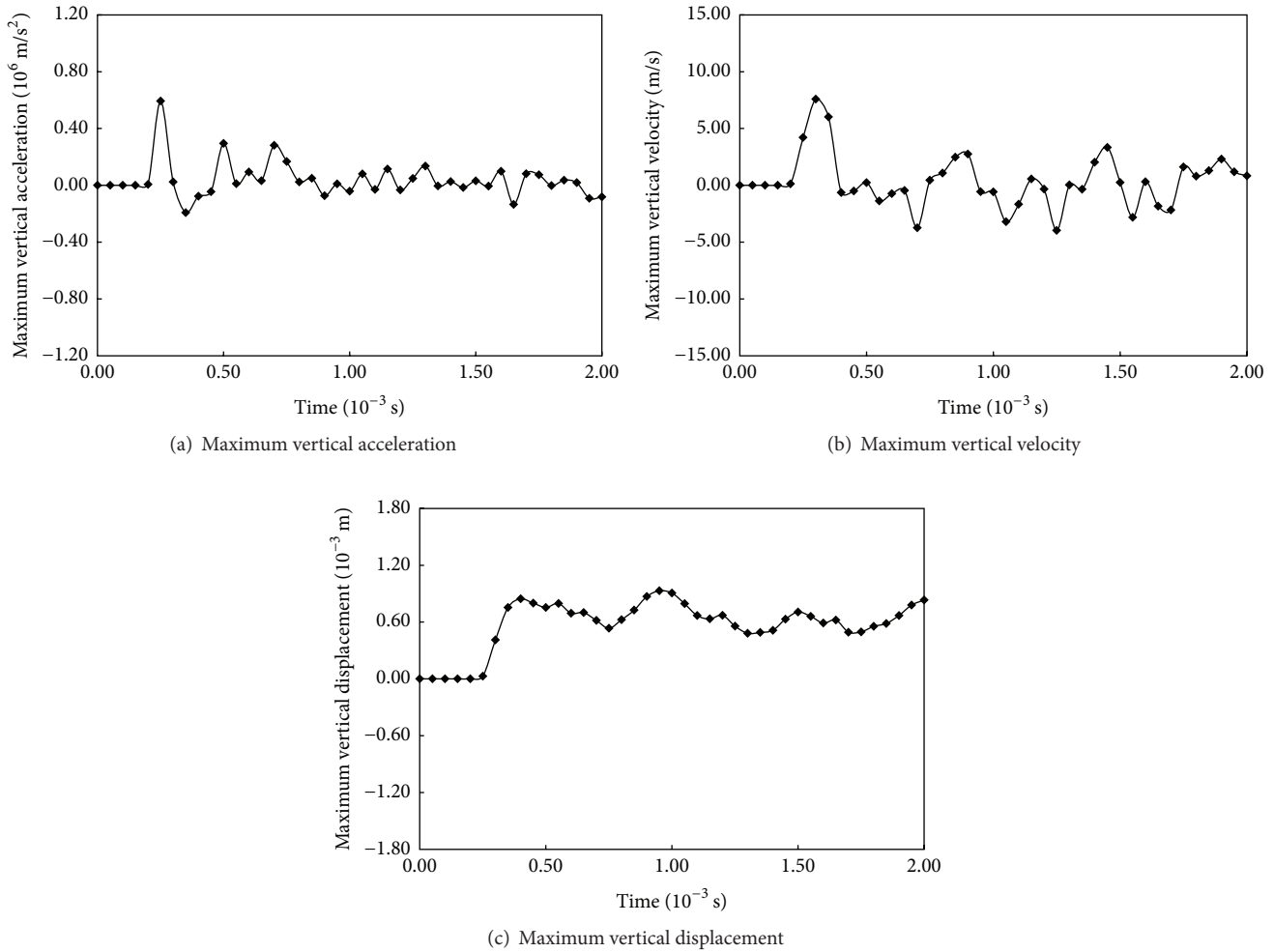


FIGURE 13: Blast-induced vibration parameters of Case 4.

## 5. Conclusions

- (1) Blast-induced vibration reduction method with water jet assistance was put forward. Hard rock experiment was conducted to obtain the suitable work parameter. The mechanism of vibration-isolation by water jet was analyzed, and the stress wave energy attenuation model by VIS near blasting source was established according to stress wave theory and blast theory.
- (2) Influence law on shock wave attenuation by VIS was simulated by ANSYS/LS-DYNA. The results indicate that, for the VIS filled with water, attenuation ratio of vibration parameters increases with the increase of distance between VIS and borehole. For the VIS filled with air, with the decrease of distance between VIS and borehole, attenuation ratio of vertical acceleration and vertical velocity increase, and attenuation ratio of displacement, however, shows a tendency of increase at first and then decrease. In addition,

under the same condition, attenuation ratio of blast-induced vibration parameters for VIS filled with air is greater than the attenuation ratio of blast-induced vibration parameter for VIS filled with water. The critical value for distance between borehole and VIS filled with air can achieve good directional blasting effect and blast-induced vibration reduction effect.

In this study, the verification of shock wave energy attenuation model and the studies of influence rules on blast-induced vibration effect were only performed numerically. Therefore, in the future, the laboratory experimental and the field experimental study to verify the results will be performed.

## Competing Interests

The authors declare that there is no conflict of interests regarding the publication of this paper.

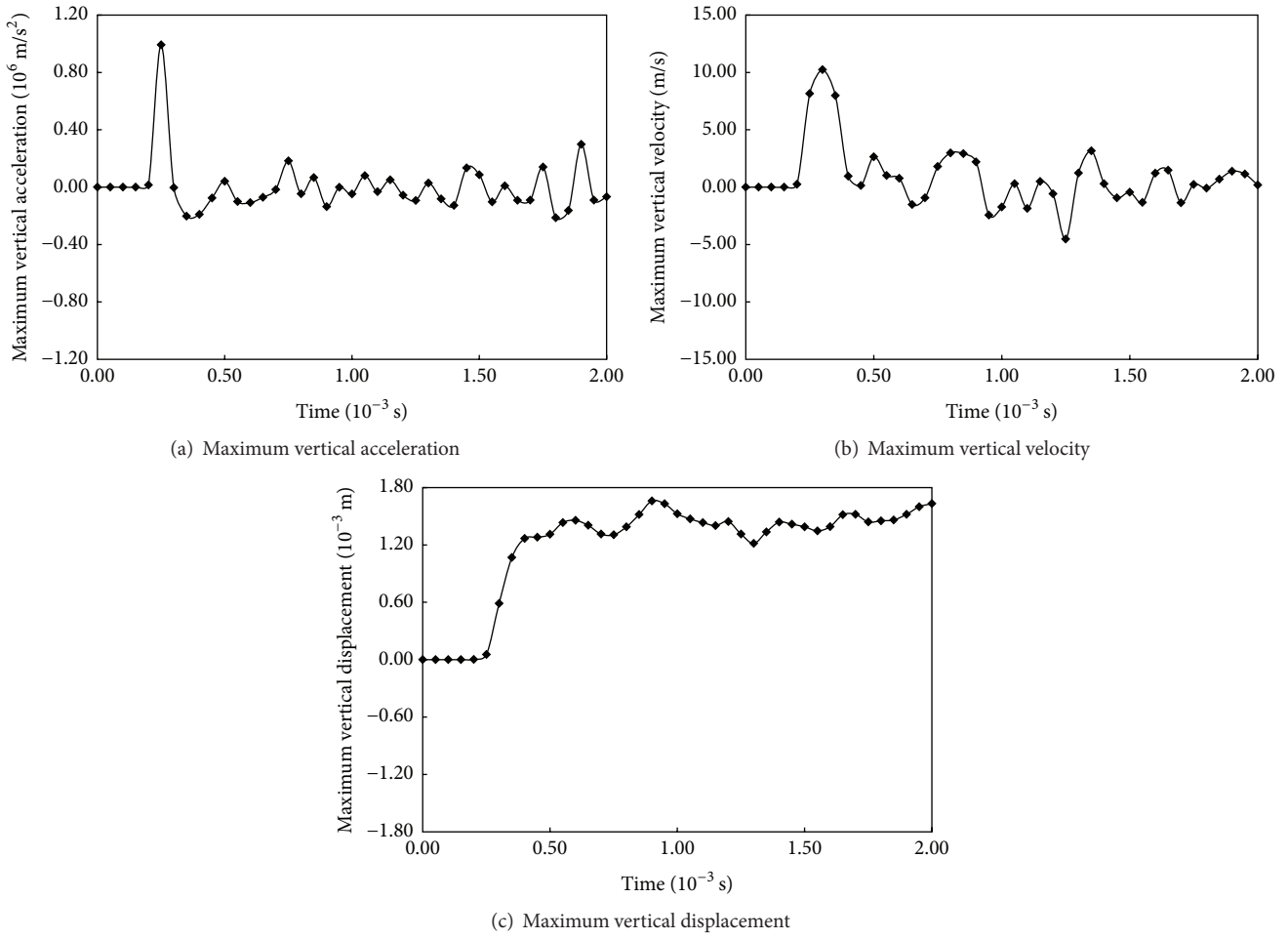


FIGURE 14: Blast-induced vibration parameters of Case 5.

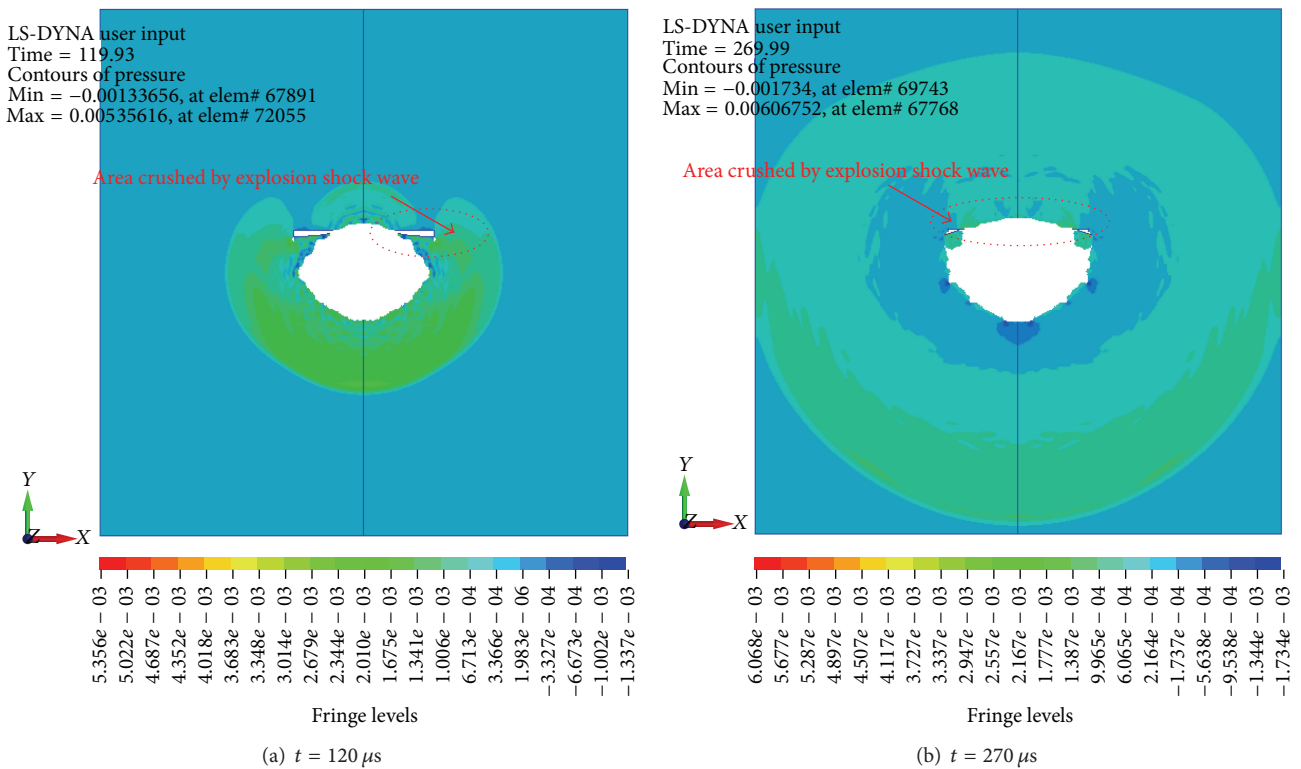


FIGURE 15: Diagram of crushed zone formation ( $D = 0.1 m$ ).

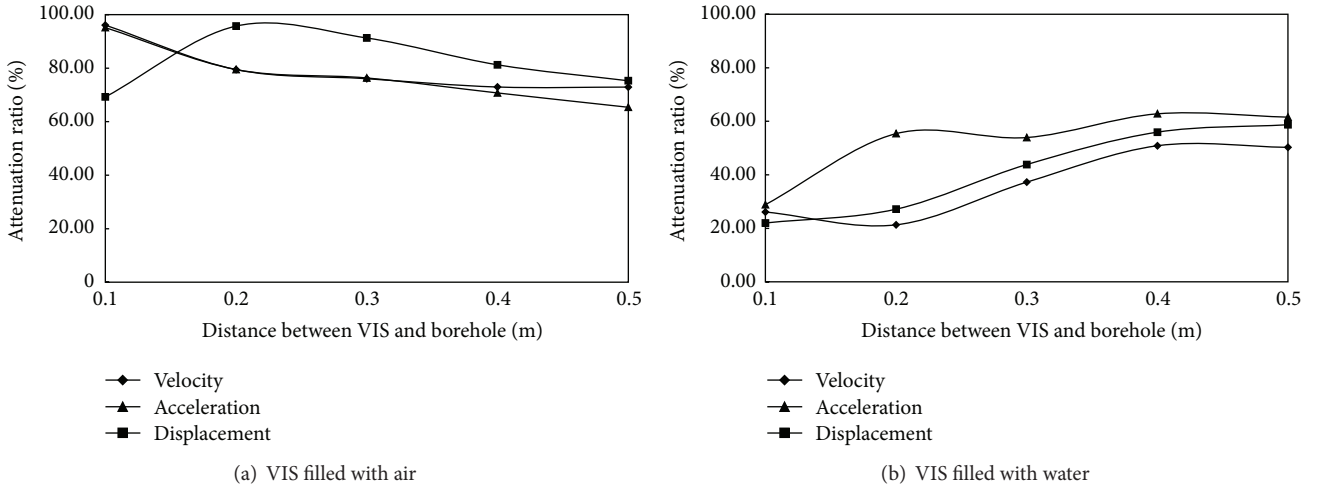


FIGURE 16: Curve of attenuation ratio under each condition.

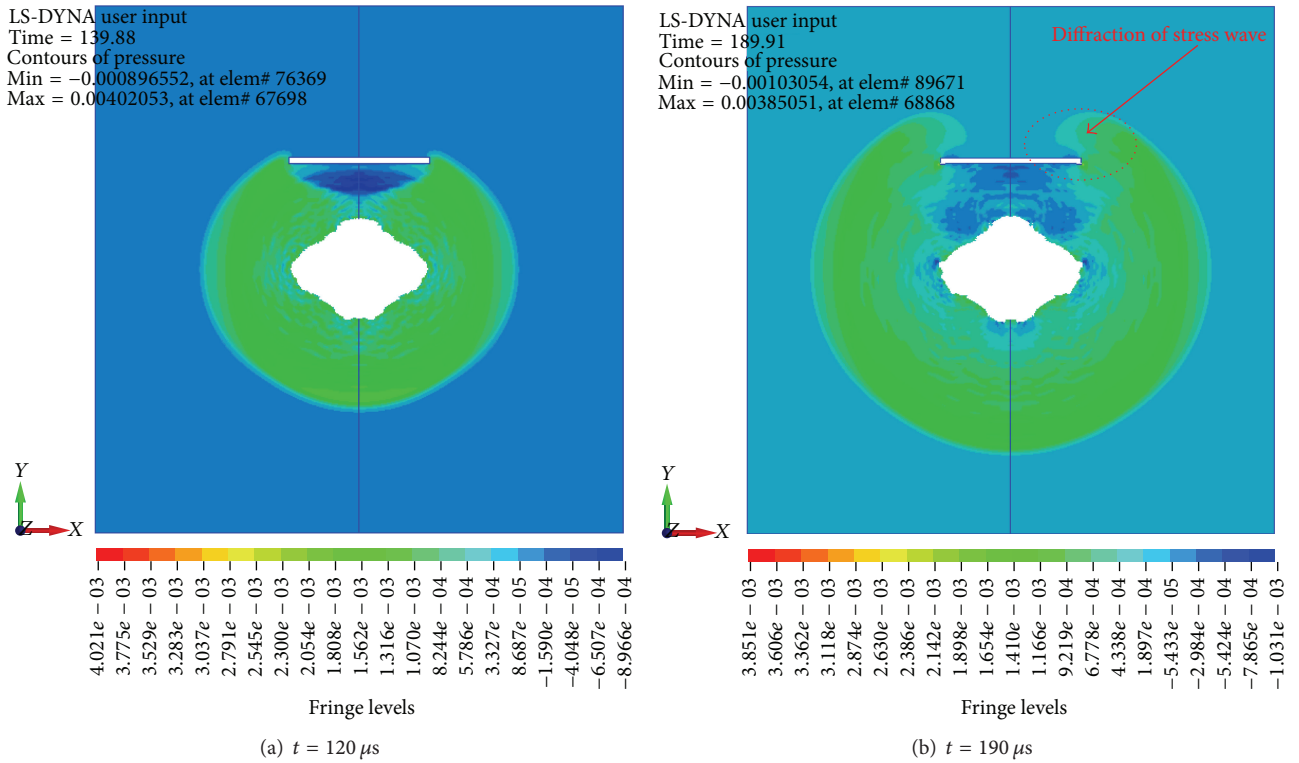


FIGURE 17: Evolution of shock wave through VIS filled with air ( $D = 0.3$  m).

### Acknowledgments

This paper is jointly supported by National Key Basic Research Program of China (no. 2014CB239203), Program for New Century Excellent Talents in University

(NCET-12-0424), and the Open Projects of State Key Laboratory of Coal Mine Disaster Dynamics and Control (Chongqing University 2011DA105287—FW201205). The authors would like to thank the State Key Laboratory of Coal Mine Disaster Dynamics and Control (Chongqing

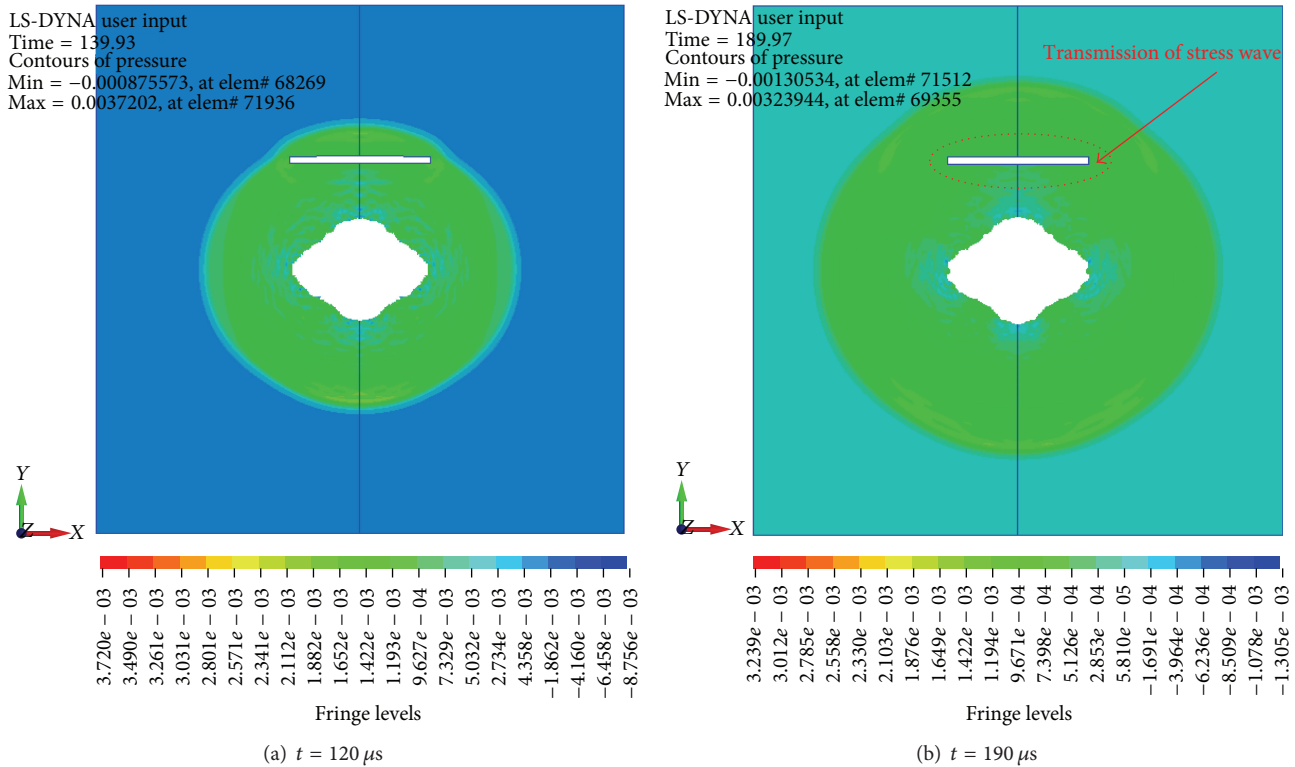


FIGURE 18: Evolution of shock wave through VIS filled with water ( $D = 0.3 \text{ m}$ ).

University) and Hubei Key Laboratory of Waterjet Theory and New Technology (Wuhan University).

## References

- [1] T. N. Singh and V. Singh, "An intelligent approach to prediction and control ground vibration in mines," *Geotechnical and Geological Engineering*, vol. 23, no. 3, pp. 249–262, 2005.
- [2] S. Jones, *Transportation and Construction-Induced Vibration Guidance Manual*, California Department of Transport, Noise, Vibration, and Hazardous Waste Management Office, Sacramento, Calif, USA, 2004.
- [3] W. Cao, X. Li, M. Tao, and Z. Zhou, "Vibrations induced by high initial stress release during underground excavations," *Tunnelling and Underground Space Technology*, vol. 53, pp. 78–95, 2016.
- [4] H. Ak, M. Iphar, M. Yavuz, and A. Konuk, "Evaluation of ground vibration effect of blasting operations in a magnesite mine," *Soil Dynamics and Earthquake Engineering*, vol. 29, no. 4, pp. 669–676, 2009.
- [5] C. Kuzu and E. Guclu, "The problem of human response to blast induced vibrations in tunnel construction and mitigation of vibration effects using cautious blasting in half-face blasting rounds," *Tunnelling and Underground Space Technology*, vol. 24, no. 1, pp. 53–61, 2009.
- [6] M. Monjezi, M. Ghafurikalajahi, and A. Bahrami, "Prediction of blast-induced ground vibration using artificial neural networks," *Tunnelling and Underground Space Technology*, vol. 26, no. 1, pp. 46–50, 2011.
- [7] H. Ak and A. Konuk, "The effect of discontinuity frequency on ground vibrations produced from bench blasting: a case study," *Soil Dynamics and Earthquake Engineering*, vol. 28, no. 9, pp. 686–694, 2008.
- [8] A. P. Rustan, "Micro-sequential contour blasting—how does it influence the surrounding rock mass?" *Engineering Geology*, vol. 49, no. 3–4, pp. 303–313, 1998.
- [9] Z. Wang, C. Fang, Y. Chen, and W. Cheng, "A comparative study of delay time identification by vibration energy analysis in millisecond blasting," *International Journal of Rock Mechanics and Mining Sciences*, vol. 60, pp. 389–400, 2013.
- [10] M. Monjezi, M. Ahmadi, M. Sheikhan, and A. Bahrami, "Predicting blast induced ground vibration using various types of neural networks," *Soil Dynamics and Earthquake Engineering*, vol. 30, no. 11, pp. 33–63, 2010.
- [11] O. Uysal, K. Erarslan, M. Akif Cebi, and H. Akcakoca, "Effect of barrier holes on blast induced vibration," *International Journal of Rock Mechanics and Mining Sciences*, vol. 45, no. 5, pp. 712–719, 2008.
- [12] X. Z. Shi and S. R. Chen, "Delay time optimization in blasting operations for mitigating the vibration-effects on final pit walls' stability," *Soil Dynamics and Earthquake Engineering*, vol. 31, no. 8, pp. 1154–1158, 2011.
- [13] S. Guruprasad and A. Mukherjee, "Layered sacrificial claddings under blast loading. Part I-analytical studies," *International Journal of Impact Engineering*, vol. 24, no. 9, pp. 957–973, 2000.
- [14] M. D. Theobald and G. N. Nurick, "Experimental and numerical analysis of tube-core claddings under blast loads," *International Journal of Impact Engineering*, vol. 37, no. 3, pp. 333–348, 2010.
- [15] S. Palanivelu, W. V. Paepegem, J. Degrieck et al., "Crushing and energy absorption performance of different geometrical shapes of small-scale glass/polyester composite tubes under

- quasi-static loading conditions," *Composite Structures*, vol. 93, no. 2, pp. 992–1007, 2011.
- [16] F. Tarlochan, S. Ramesh, and S. Harpreet, "Advanced composite sandwich structure design for energy absorption applications: blast protection and crashworthiness," *Composites Part B: Engineering*, vol. 43, no. 5, pp. 2198–2208, 2012.
- [17] H. Zhao, H. Yu, Y. Yuan, and H. Zhu, "Blast mitigation effect of the foamed cement-base sacrificial cladding for tunnel structures," *Construction and Building Materials*, vol. 94, no. 6891, pp. 710–718, 2015.
- [18] W. B. Lu, S. H. Lai, and Z. H. Dong, "Analysis of vibration isolating effect of pre-slitting cracking in rock excavation by blasting," *Explosion and Shock Waves*, vol. 17, pp. 193–198, 1997.
- [19] J. W. Lou and Y. Long, "Study on the effect of the pre-splitting propagation of the blasting seismic waves," *Blasting*, vol. 22, pp. 1–5, 2005.
- [20] Y. Luo, Y. Y. Liu, and C. P. Yi, "Numerical simulation analysis of the effect of pre-splitting crack parameters on damping vibration," *Blasting*, vol. 24, pp. 25–27, 2007.
- [21] W. L. Fourney, R. D. Dick, D. F. Fordyce, and T. A. Weaver, "Effects of open gaps on particle velocity measurements," *Rock Mechanics and Rock Engineering*, vol. 30, no. 2, pp. 95–111, 1997.
- [22] G. M. Song, "Approach to effect of blast vibration and methods to decrease vibration," *The World Mining Letters*, vol. 15, pp. 26–29, 1999.
- [23] S. E. Kattis, D. Polyzos, and D. E. Beskos, "Modelling of pile wave barriers by effective trenches and their screening effectiveness," *Soil Dynamics and Earthquake Engineering*, vol. 46, pp. 713–728, 1999.
- [24] A. J. Prakash, P. Palroy, and D. D. Misra, "Analysis of blast vibration characteristics across a trench and a pre-split plane," *Fragblast*, vol. 8, no. 1, pp. 51–60, 2004.
- [25] M. Adam and O. Von Estorff, "Reduction of train-induced building vibrations by using open and filled trenches," *Computers and Structures*, vol. 83, no. 1, pp. 11–24, 2005.
- [26] D. Bogunovic and V. Kecojevic, "Artificial screen for reducing seismic vibration generated by blasting," *Environmental Geology*, vol. 53, no. 3, pp. 517–525, 2007.
- [27] Y. F. Zhang, D. P. Yao, Z. Z. Xie, Y. X. Xu, G. M. Li, and Y. Q. Ye, "Analysis of master control factor of blasting seismic effect and discussion on shock absorption measures," *Rock and Soil Mechanics*, vol. 31, no. 1, pp. 304–308, 2010.
- [28] D. Park, B. Jeon, and S. Jeon, "A numerical study on the screening of blast-induced waves for reducing ground vibration," *Rock Mechanics and Rock Engineering*, vol. 42, no. 3, pp. 449–473, 2009.
- [29] G. Y. Gao, Z. Y. Li, C. Qiu, and Z. Q. Yue, "Three-dimensional analysis of rows of piles as passive barriers for ground vibration isolation," *Soil Dynamics and Earthquake Engineering*, vol. 26, no. 11, pp. 1015–1027, 2006.
- [30] D. S. Kim and J. S. Lee, "Propagation and attenuation characteristics of various ground vibrations," *Soil Dynamics and Earthquake Engineering*, vol. 19, no. 2, pp. 115–126, 2000.
- [31] J. Dai, *Dynamic Behaviors and Blasting Theory of Rock*, Metallurgical Industry Press, Beijing, China, 2013.
- [32] W. H. Wang, X. B. Li, Z. L. Zhou, and Y. P. Zhang, "Energy-transmitted rule of various stress waves across open joint," *Journal of Central South University (Science and Technology)*, vol. 37, no. 2, pp. 376–380, 2006.
- [33] L. L. Wang, *Foundation of Stress Waves*, National Defense Industry Press, 2005.
- [34] Z. C. Zhang, *Directional Pressure Relief Vibration Isolation Blasting*, Chongqing University Press, Chongqing, China, 2013.
- [35] X. B. Guo and J. C. Zhang, *Blasting Engineering*, China Communication Press, 2007.
- [36] D. Y. Shi, Y. C. Li, and S. M. Zhang, *The Analysis of Explicit Explosion Mechanics Base on Ansys/Ls-dyna8.1*, Tsinghua University Press, Beijing, China, 2005.
- [37] Livermore Software Technology Corporation, *LS-DYNA Keyword User's Manual*, Livermore Software Technology Corporation, Livermore, Calif, USA, 2007.

## Research Article

# Numerical Analysis on Failure Modes and Mechanisms of Mine Pillars under Shear Loading

Tianhui Ma,<sup>1,2</sup> Long Wang,<sup>1</sup> Fidelis Tawiah Suorineni,<sup>2</sup> and Chunan Tang<sup>1</sup>

<sup>1</sup>State Key Laboratory of Coastal and Offshore Engineering, Dalian University of Technology, Dalian 116024, China

<sup>2</sup>School of Mining Engineering, Faculty of Engineering, UNSW Australia, Sydney, NSW 2051, Australia

Correspondence should be addressed to Tianhui Ma; [tianhuima@dlut.edu.cn](mailto:tianhuima@dlut.edu.cn)

Received 13 January 2016; Accepted 11 April 2016

Academic Editor: Marcin A. Lutyński

Copyright © 2016 Tianhui Ma et al. This is an open access article distributed under the Creative Commons Attribution License, which permits unrestricted use, distribution, and reproduction in any medium, provided the original work is properly cited.

Severe damage occurs frequently in mine pillars subjected to shear stresses. The empirical design charts or formulas for mine pillars are not applicable to orebodies under shear. In this paper, the failure process of pillars under shear stresses was investigated by numerical simulations using the rock failure process analysis (RFPA) 2D software. The numerical simulation results indicate that the strength of mine pillars and the corresponding failure mode vary with different width-to-height ratios and dip angles. With increasing dip angle, stress concentration first occurs at the intersection between the pillar and the roof, leading to formation of microcracks. Damage gradually develops from the surface to the core of the pillar. The damage process is tracked with acoustic emission monitoring. The study in this paper can provide an effective means for understanding the failure mechanism, planning, and design of mine pillars.

## 1. Introduction

Studies on pillar size and stability have been conducted for many years. The main research methods include the safety factor, probabilistic analysis, numerical modeling, empirical methods, and physical testing methods. Brady et al. [1] developed a pillar strength formula accounting for pillar size and geometry based on the existing representative design theory for pillar spacing. Bieniawski [2] considered that the compressive strength of coal cubes (short-term strength) decreases with an increase in size and reaches an asymptotic value at a cube size of about 1.5 m which, according to him, was the critical size for coal. Lunder and Pakalnis [3] considered the role of confinement in hard rock pillar strength. González-Nicieza et al. [4] proposed a new formula considering Bieniawski's rock mass quality classification and the shear-resistance safety factor of pillars. Esterhuizen [5] investigated some of the issues affecting pillar strength at low width-to-height ratios in hard brittle rock and concluded that the strength of slender pillars was more variable than that of wider pillars. Mortazavi et al. [6] suggested that, at high WH ratios, pillars behave in a very stiff manner in the elastic range,

demonstrating a high load-bearing capacity. Esterhuizen et al. [7] developed a pillar strength equation based on stable and failed pillars observed. Ghasemi and Shahriar [8] proposed a new coal pillar design method. Suorineni et al. [9, 10] developed new knowledge on why pillars in ore bodies in shear are more prone to catastrophic failures than would normally be expected. They introduced the concept of shear loading in orebodies and pillars.

Many scholars in China have carried out in-depth studies on pillar stability. Liu and Xu [11] estimated rock mass strength for the gob area of a phosphate mine according to rock mass classification, analyzed stability of pillars in the gob area using the safety factor and reliability analysis methods, and represented the safety factor of pillars by the average safety factor. Yang [12] proposed a new design method for pillar spacing, which has been applied effectively in engineering practice. Wang and Li [13] proposed the concept of shear-resistance safety factor for mine pillars, considering that pillars generally fail in shear. They suggested that pillars were safe and reliable when the shear-resistance safety factor was greater than 1.2. Wang et al. [14] proposed a formula for pillar width for deep stope mining and suggested

that the key factors affecting the proper pillar width were the stopping span and depth. The relevant theory was verified by field tests.

In summary, proper pillar design is the key to prevention of pillar failure and reduction of related accidents [15]. Pillar design is mostly based on empirical formulas, limit equilibrium, loading theory, and other analysis methods [12, 16] at present. Due to differences in geological conditions in various regions and complex mining conditions, the above-mentioned methods are not optimized approaches for the design of pillars. Small pillar sizes would lead to surface subsidence and affect the stability of mines, while too thick pillars lead to waste of resources [17]. In this study, the rock failure process analysis program, RFPA2D [18–21], was used to simulate pillars of various sizes and to investigate the failure mechanisms. The simulation results provide further understanding of pillar mechanics and can be used for safer design and construction of underground mine pillars.

## 2. Principles of RFPA

When rock is under load, it continuously gets microcracks after a certain stress level resulting in nonlinear deformation. The development and the accumulation of these microcracks eventually lead to a final macrofailure of the rock. The nonlinear deformation of rocks can be simulated with Finite Element Method (FEM), but it only stays on macrodeformation of the rocks; it cannot describe the development of the microcracking process leading to the formation of the macrofailure plane formation. In order to simulate the process of rock failure, many numerical modeling methods such as Finite Difference Method (FDM), Boundary Element Method (BEM), Half Analytical Element Method (HAEM), Discrete Element Method (DEM), and Extend Finite Element Method (EFEM) have been applied for fully solving some difficult rock engineering problems. These methods still have many imperfections, for instance, problems of nonlinearity and discontinuities of rocks, problems relating the effects of step excavation, and backfill practice on stability of rock masses. To solve these problems, in 1995, a new numerical modeling method referred to as rock failure process analysis (RFPA) was developed to conduct stress analysis based on Finite Element Method and nonlinearity, nonhomogeneity, and the anisotropic properties of rocks. The RFPA code has several special features:

- (1) The macrofailure is an accumulation of microdamage. Elastic-brittle constitutive criterion is applied to each element. When the stresses of some elements reach peak strength, failure occurs. By this method, physically discontinuous problems can be resolved with continuum mechanics.
- (2) Heterogeneity of rock is accounted for in the elements using Weibull distribution in the code for modulus of elasticity, strength, and some other parameters of the elements.
- (3) Acoustic emission associated with the progressive failure process is included in the code by recording the event-rate of failed elements.

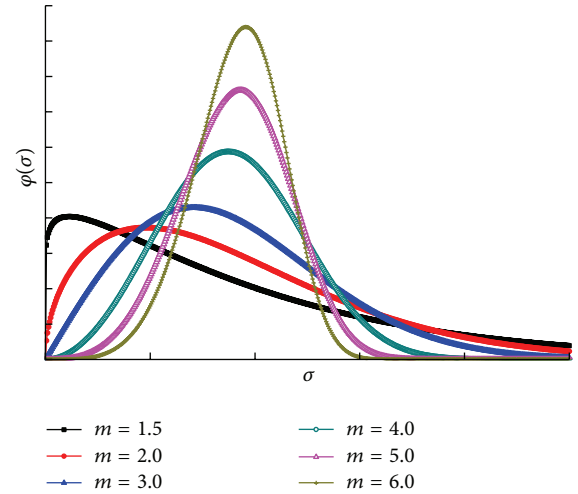


FIGURE 1: Weibull distribution for mechanical properties of rock materials with different homogeneity indices  $m$ .

In RFPA2D, Weibull statistical distribution is introduced to describe the discrete physical-mechanical property as in the following formula:

$$\varphi(\sigma) = \frac{m}{\sigma_0} \left( \frac{\sigma}{\sigma_0} \right)^{m-1} \exp \left[ - \left( \frac{\sigma}{\sigma_0} \right)^m \right]. \quad (1)$$

In the formula,  $\sigma$  is a parameter for one element,  $\sigma_0$  is the mean value of the same parameter for all the elements in one grain, and  $m$  is a shape parameter. The shape parameter  $m$  is defined as the homogeneity index of the rock.

For a practical rock material, the type of the statistical distribution needs to be determined in the laboratory. At this time, we assume the physical-mechanical properties of the elements follow (1). A larger  $m$  implies a more homogeneous material and vice versa. Figure 1 shows the shape of the probability density function for various homogeneity indices.

Once the material fails, the mechanical property and the ability to bear load will be changed. Usually, the change is a degradation process, that is, reduction of the physical-mechanical property parameter. Based on the above-mentioned theory, RFPA2D deals with element failure by introducing degradation of the element property. When the stresses in some elements satisfy the Mohr-Coulomb shear failure criterion or maximum tensile strain criterion, the element is damaged and becomes weak according to the rules specified by the strength criterion. The stress and deformation distributions throughout the model are then adjusted instantaneously after each rupture to reach the equilibrium state. The stresses in some elements might be increased due to stress redistribution. These updated stresses may exceed the critical value specified by the strength criterion. Further ruptures may, therefore, be caused. The process is repeated till no stable elements are present. By this way, the continuous media mechanics method can be used to deal with the discontinuous problem. And the Finite Element Method can be used to simulate the whole failure process of rock material from deformation, microfailure to macroscopic failure.

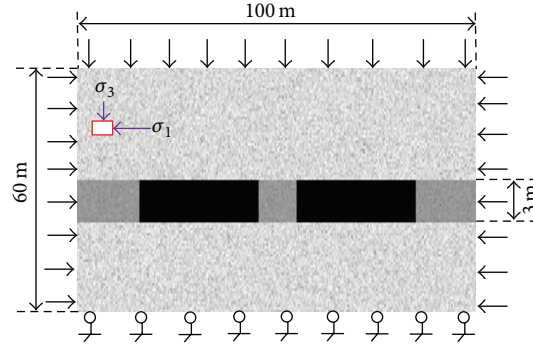


FIGURE 2: Numerical model and boundary condition.

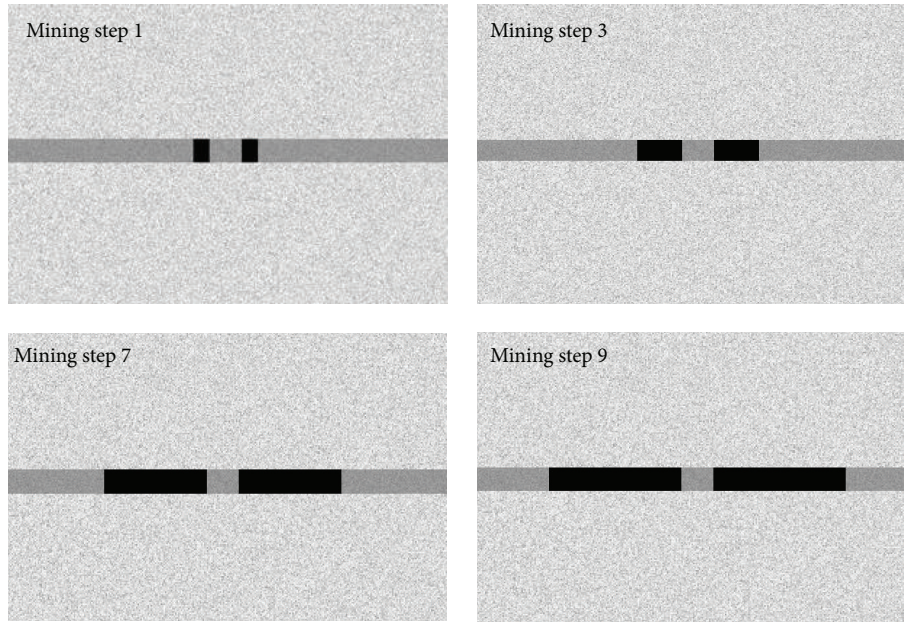


FIGURE 3: Mining sequence and pillar geometry within the RFPA2D model.

### 3. Numerical Modeling of Pillars Using RFPA

**3.1. Model Overview.** Following the procedure used by Suorinen et al. [9, 10] the effects of pillar dip angle, width-to-height ratio, and a certain stress ratio on the stability of pillars in a room-and-pillar mine are investigated using five width-to-height ratios, namely, 0.5, 1.0, 1.5, 2.0, and 2.5, at various degrees of orebody inclination, namely,  $0^\circ$  (Horizontal orebody resulting in vertical pillars),  $10^\circ$ ,  $20^\circ$ ,  $30^\circ$ , and  $40^\circ$  (orebody dip angles result in inclined pillars). A typical numerical model setup in RFPA2D is shown in Figure 2. For comparative analysis of the impact and role of various factors, the extraction ratio is kept constant at 75% in accordance with Suorinen et al. [10]. The model dimension is  $100 \text{ m} \times 60 \text{ m}$ . The height of orebody is 3 m. The model consists of  $500 \times 300 = 150000$  elements. The loading was applied in three stages. Firstly, loading was applied in both X and Y directions at  $k_0$  ratios of 0.5, 1.0, 1.5, and 2.0. Then, the stress in the X and Y directions remained unchanged and the excavation steps were carried out as shown in Figure 3

until the extraction ratio of 75% is reached for the given pillar size. After finishing all the excavation steps, the loading in the X direction remained unchanged, and the loading in the Y direction was gradually increased until failure. The loading was increased by 0.2 MPa per step.

**3.2. Model Input Mechanical Parameters.** The strength and elastic modulus of each element were assigned according to the Weibull distribution so as to reflect the rock mass heterogeneity. The coefficient  $m$  reflects the degree of homogeneity of rock mass properties. The higher the coefficient  $m$  is, the more homogeneous the rock mass properties are; the smaller the coefficient  $m$  is, the more heterogeneous the rock mass properties are. The coefficient  $m$  is determined by an empirical formula [22]:

$$\frac{\sigma_c}{\sigma_0} = 0.85298 - 0.80668 \exp\left(-\frac{m}{10.68877}\right) \quad (2)$$

$$\frac{E_c}{E_0} = 1.02453 - 0.62081 \exp\left(-\frac{m}{2.59074}\right),$$

TABLE I: Mechanical properties of the model.

Parameter	Coefficient of homogeneity ( $m$ )	Uniaxial compressive strength ( $\sigma_c$ )/MPa	Elastic modulus ( $E_c$ )/MPa	Poisson's ratio ( $\nu$ )	Angle of internal friction ( $\varphi$ )/°
Rock mass	4	170	70000	0.25	40
Orebody	7	60	20000	0.22	35

where  $\sigma_c$  and  $E_c$  are, respectively, the simulated uniaxial compressive strength and the elastic modulus and  $\sigma_0$  and  $E_0$  are, respectively, the characteristic compressive strength and the characteristic elastic modulus of mesoscopic elements. According to the real mechanical parameters of rock masses in a mine, the macroscopic parameters can be converted to mesoscopic element parameters according to the above empirical formulas. The material parameters for the rock masses and orebody in the model are listed in Table I.

## 4. Simulation Results and Analyses

**4.1. Failure Characteristics of Vertical Pillars with Different Width-to-Height Ratios.** Mine pillars are in situ rock left after mining to ensure mine safety. The determination of pillar sizes dictates the cost of mining and mine safety. Pillar instability refers to the compressional-shear or splitting failure under uniaxial stresses when external loading reaches a limit value. Upon failure, the pillar loses its bearing capacity and can no longer transfer stresses from the overlying strata [17] to the floor.

Accompanying these damage processes, an elastic stress wave is generated, which travels from the point of origin within the rock to a boundary, where it is observed as an acoustic emission signal [23]. In rock, acoustic emission is generated by crack formation under high stress [24]. This phenomenon provides a basis for a method which is able to detect zones of microcracking or macrocracking or highly stressed zones in rock without any knowledge of the mechanical properties or the state of stress [24]. Currently, acoustic emission is the most direct method to monitor and predict the process of rock burst [25]. This study mainly focuses on pillar rock burst. Here, only the failure processes of pillars with various sizes under various  $k_0$  pressures of 0.5, 1.0, 1.5, and 2.0 are presented. In the plot of acoustic emissions, the size of circles represents the magnitude of energy released during acoustic emissions, and the number of circles indicates the amount of acoustic emissions. As shown in Figure 4, the location of pillar monitoring point was set at pillar midheight.

Figure 6 shows the corresponding shear stresses to the various loading stages in Figure 5. As shown in Figures 5 and 6, at the initial loading stage, since the loading is low no acoustic emission is observed (Figure 5(a)) and only a few microcracks appear at some locations where the compressive strength is low or tensile stress is high and a small amount of acoustic emissions is detected (Figure 5(b)). The microcracking gradually propagates towards the pillar surface and tends to develop towards the four corners (Figure 5(b): step 82-1). At this point, cracks have not coalesced yet and the pillar still has certain support capacity. With further increase in load, the axial stress in the pillar increases and microcracks in the

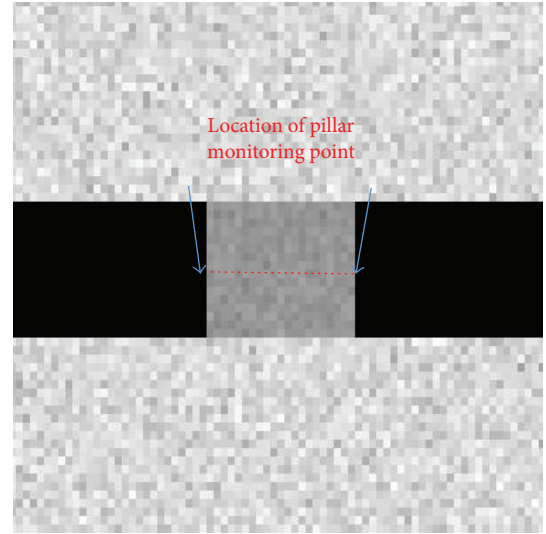


FIGURE 4: Location of stress and deformation monitoring points.

pillar propagate and coalesce as shown in Figure 5(c). Figures 5 and 6 both show that a shear failure zone is eventually formed in the pillar and the pillar is completely failed (Figures 5(c) and 6(c)).

The corresponding stress-strain curve to the loading steps in Figures 5 and 6 is shown in Figure 7. Figure 7 shows that the stress-strain curve is approximately linear up to the point of failure. The figure shows that the maximum average axial stress in the pillar is 32.8 MPa. This is the pillar strength. The figure also shows that the pillar has a residual strength of about 12.5 MPa.

As shown in Figures 8, 9, 11, and 12 microcracks propagate more from the outside of the pillar towards the pillar core and the bearing capacity also increases with increasing pillar size as shown in Figures 7, 10, and 13. In these figures the pillar strengths are 32.8 MPa, 33.2 MPa, and 34.2 MPa for pillar  $W/H$  ratios of 0.5, 1, and 1.5, respectively.

When the width-to-height ratio is 2.0, a small amount of acoustic emissions and microcracks occurs first at the pillar corners (Figure 14(b)) and increases towards the centre of the pillar as shown in Figure 14(c) where there is a great amount of acoustic emissions occurring at that loading stage, indicating that the pillar has reached its ultimate support capacity. It can be seen from the corresponding stress-strain curve shown in Figure 16 that the average pillar strength is 43.4 MPa. As shown in Figure 14(c), cracks are formed on the pillar surface and coalesce at the central region, leading to formation of a compressive failure zone. Figure 15 shows plot of shear stresses around a pillar with width-to-height ratio = 2.0.

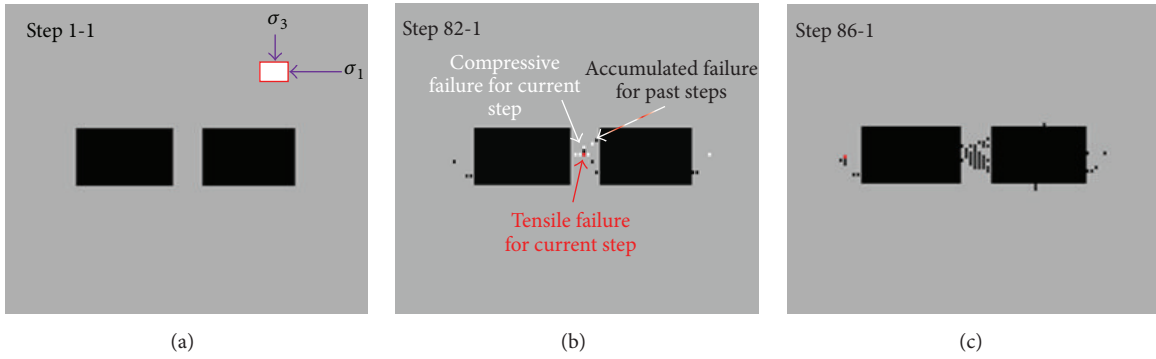


FIGURE 5: Plot of acoustic emissions for a pillar with width-to-height ratio = 0.5.

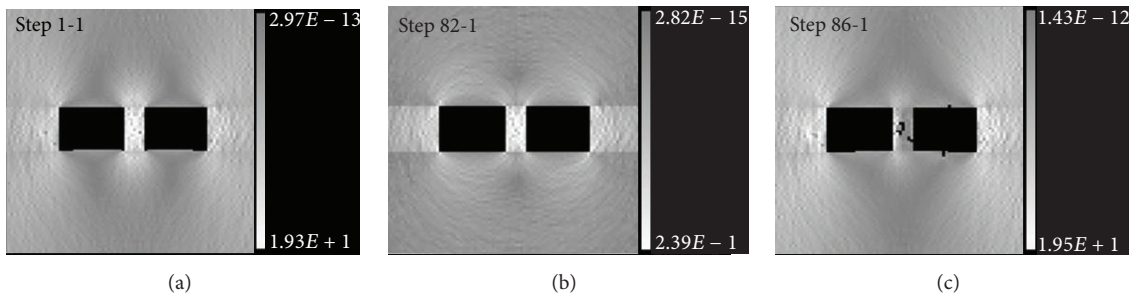


FIGURE 6: Plot of shear stresses around a pillar with width-to-height ratio = 0.5.

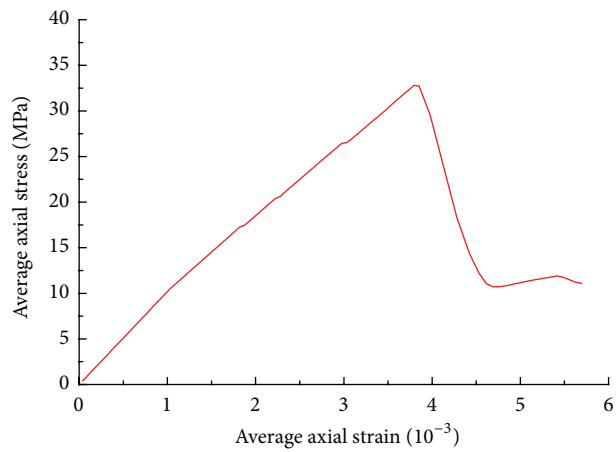


FIGURE 7: Average axial stress-strain curve for a pillar with width-to-height ratio = 0.5.

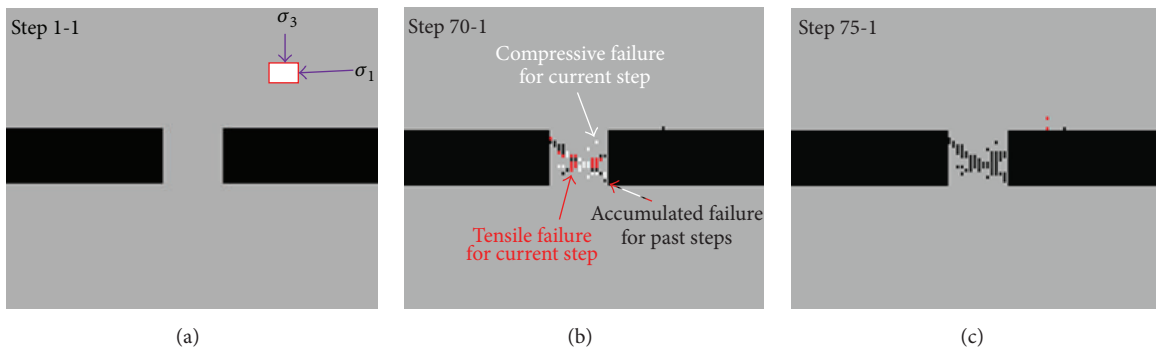


FIGURE 8: Plot of acoustic emissions for a pillar with width-to-height ratio = 1.0.

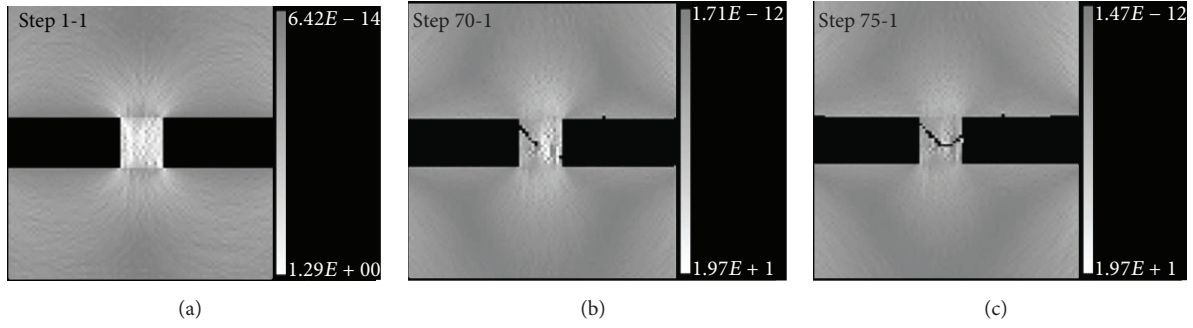


FIGURE 9: Plot of shear stresses around a pillar with width-to-height ratio = 1.0.

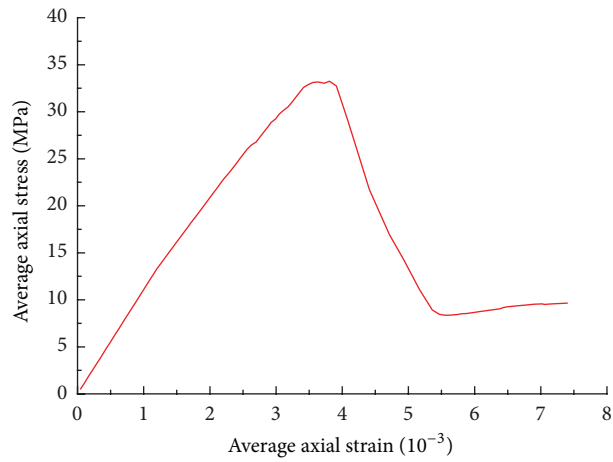


FIGURE 10: Average axial stress-strain curve for a pillar with width-to-height ratio = 1.0.

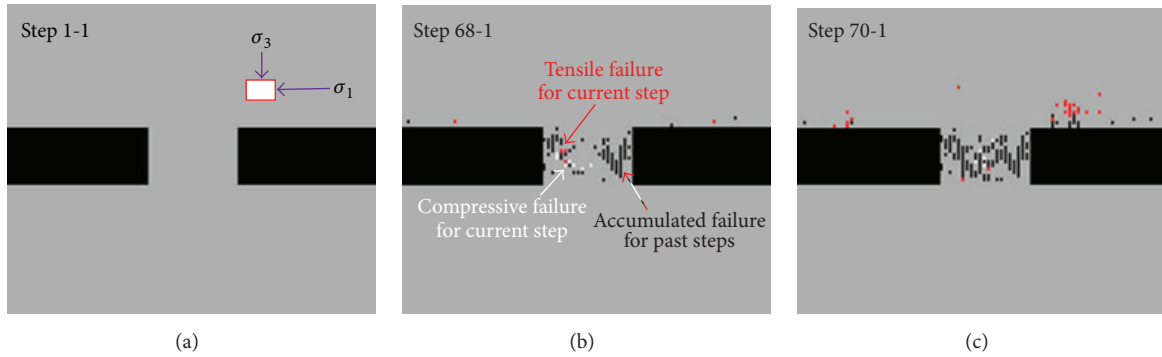


FIGURE 11: Plot of acoustic emissions for a pillar with width-to-height ratio = 1.5.

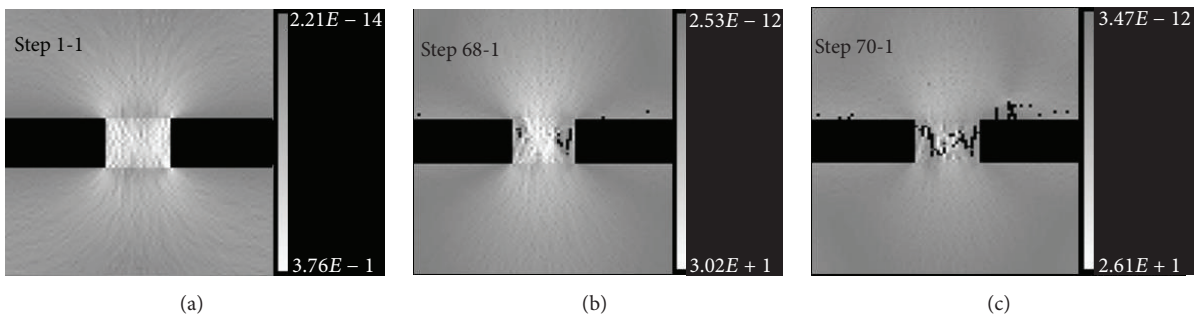


FIGURE 12: Plot of shear stresses around a pillar with width-to-height ratio = 1.5.

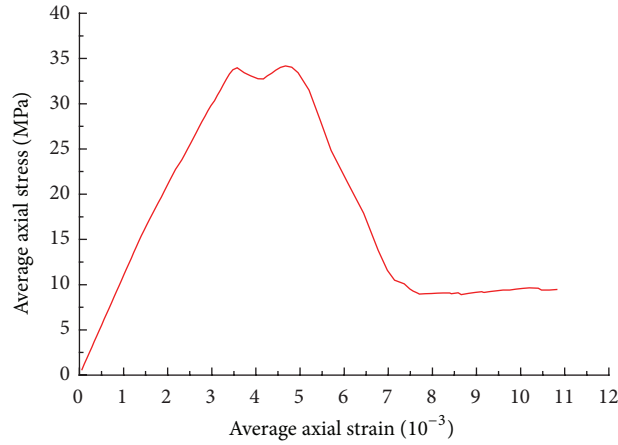


FIGURE 13: Average axial stress-strain curve for a pillar with width-to-height ratio = 1.5.

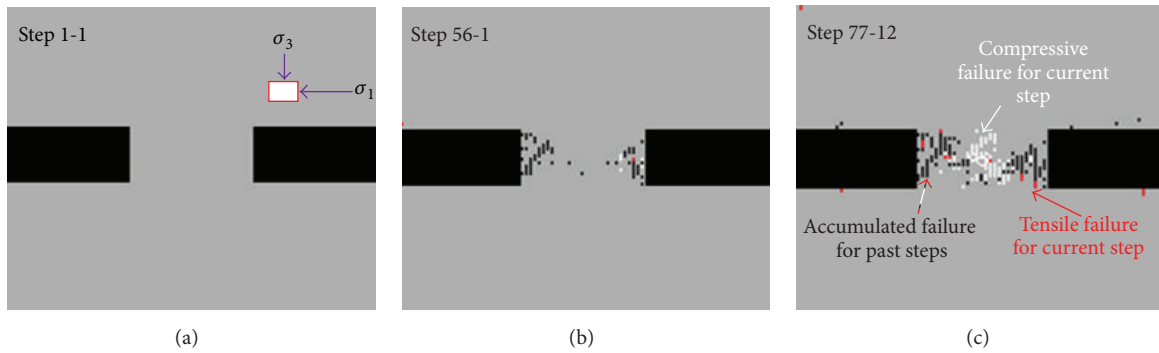


FIGURE 14: Plot of acoustic emissions for a pillar with width-to-height ratio = 2.0.

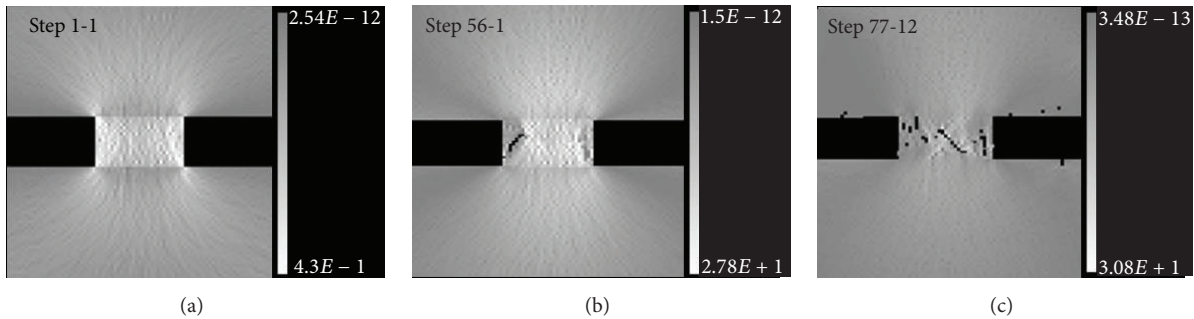


FIGURE 15: Plot of shear stresses around a pillar with width-to-height ratio = 2.0.

As can be seen from Figures 17 and 18, the failure modes of the pillars with width-to-height ratios of 2 and 2.5 are similar. The average pillar strength is 44.9 MPa for the pillar  $W/H$  ratio of 2.5 indicating an increased pillar strength by 3.4% compared to the case with  $W/H = 2.0$  (Figure 19).

The simulation results indicate that, with increasing pillar size, shear band failure from the surface to the interior is the main failure mode. Elastic stresses start to build up at the pillar edges and stress concentration rises at these points, and the pillar edge failure leads to stress concentration shifting towards the pillar core. Therefore, failure first occurs on the pillar surface and gradually develops towards the core of the pillar.

*4.2. Effects of Various Pillar Inclination on Pillar Strength.* As shown in Figure 20, the pillar strength increases with increasing width-to-height ratio. When the orebody is horizontal, the strength that the pillar can sustain is higher than that in case of an inclined orebody and confirms the findings by Suorineni et al. [10].

Generally speaking, larger rocks contain greater amount of weak structural planes, which is the main cause of lower pillar strength for the pillar with certain width-to-height ratio. Hence, the bearing capacity of the pillar increases and then keeps constant when the width-to-height ratio increases to enough large value (the height remains constant).

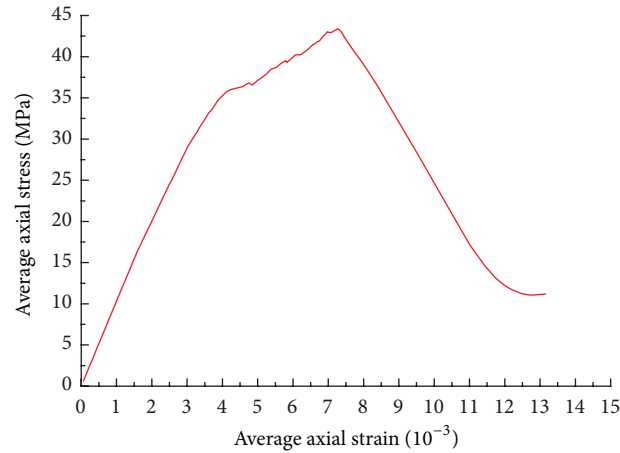


FIGURE 16: Average axial stress-strain curve for a pillar with width-to-height ratio = 2.0.

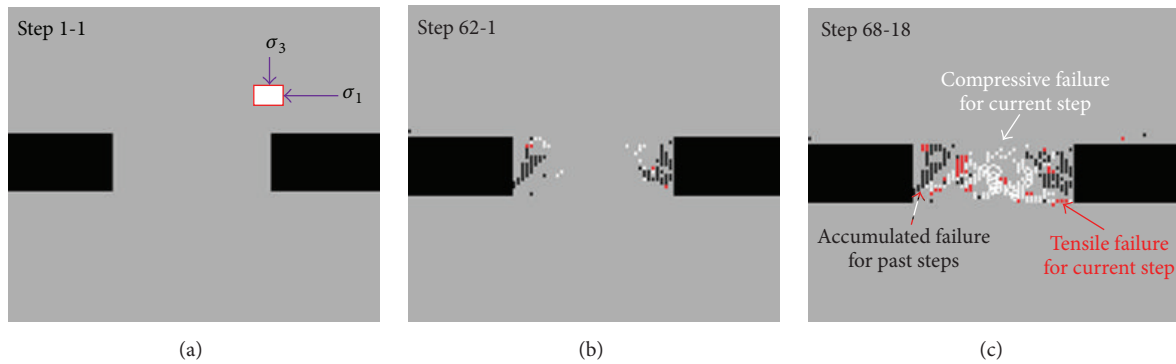


FIGURE 17: Plot of acoustic emissions for a pillar with width-to-height ratio = 2.5.

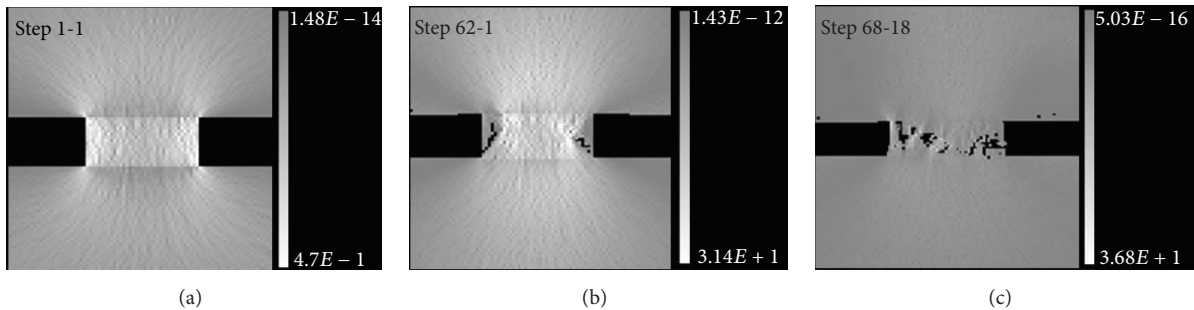


FIGURE 18: Plot of shear stresses around a pillar with width-to-height ratio = 2.5.

For the pillar with the width-to-height ratio of 2.0 under various  $k_o$  pressures, the principal stress difference and axial displacement are plotted in Figure 21.

As known from triaxial compression tests, brittleness and plasticity are not intrinsic properties of rock, instead, dependent on the stress state. Rock brittleness and plasticity can be converted with each other with changing stress state  $k_o$  [26]. It can be seen from Figure 21, when the pressure ratio  $k_o$  is equal to 2.0, the principal stress difference increases to a peak value first and then drops rapidly. The failure mode of the pillar is brittle failure. With decreasing the pressure ratio  $k_o$ , the stress curves become gentle, indicating that plasticity

is more dominant. Therefore, the failure mode of the pillar is plastic failure when the pressure ratio  $k_o$  decreases. The higher the pressure ratio  $k_o$  is, the more prominent the brittle failure characteristics are.

**4.3. Pillar Stresses in Inclined Pillars.** When mine pillars have sharp corners stress concentration usually occurs at the sharp corners. Hoek and Brown [27] suggest that in calculating average pillar stresses the corner stresses should be ignored. In this paper, the stresses and failure process of pillars at various dip angles are simulated using the RFP2D program. The major principal stresses  $\sigma_1$  on the two diagonals and the

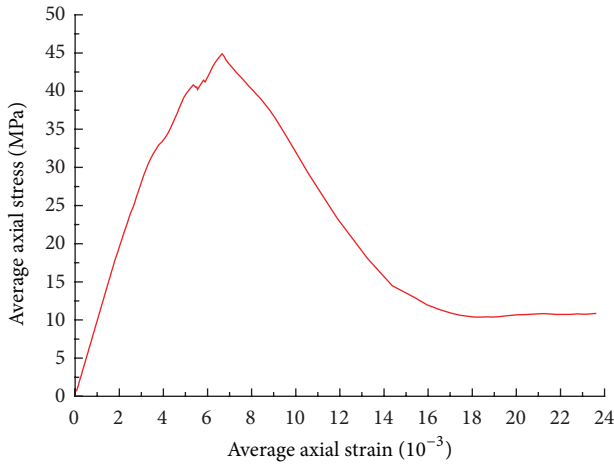


FIGURE 19: Average axial stress-strain around a pillar with width-to-height ratio = 2.5.

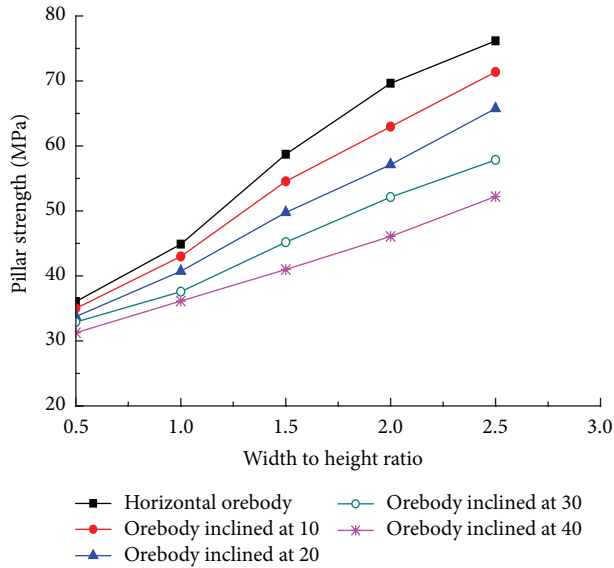


FIGURE 20: Pillar strength at various inclinations for various width-to-height ratios for  $k_o$  of 1.5.

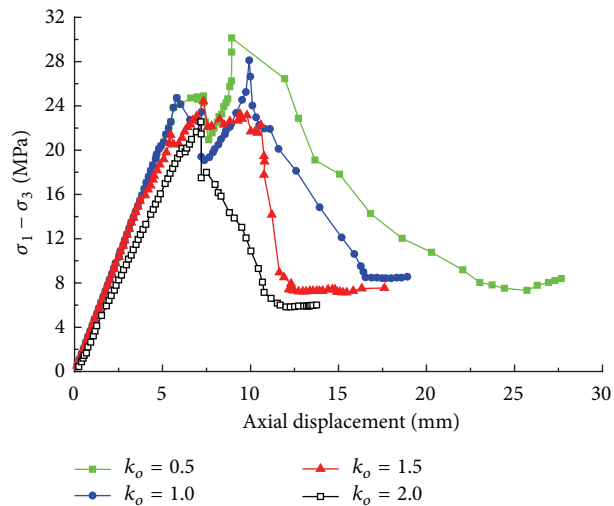


FIGURE 21: Variations of principal stress difference with axial displacement for various pressures ratios,  $k_o$ .

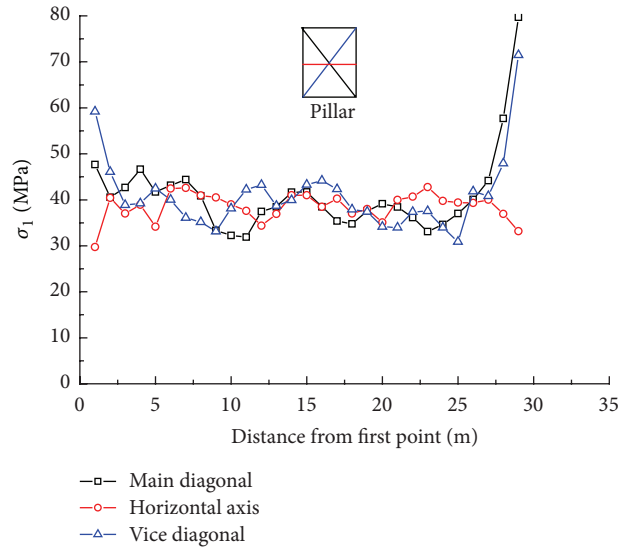


FIGURE 22: Variation of  $\sigma_1$  with distance from the first point (dip angle =  $0^\circ$ ).

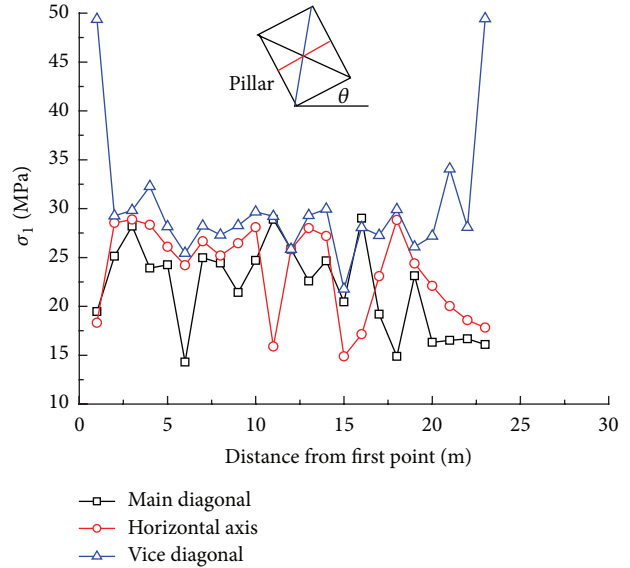


FIGURE 23: Variation of  $\sigma_1$  with distance from the first point (dip angle =  $10^\circ$ ).

horizontal axis at midheight of the pillar are plotted as shown in Figures 22 and 23 for a vertical pillar and an inclined pillar, respectively.

As can be seen from Figures 22 and 23, stress concentration occurs in the four corners of the pillar. In order to better explain microcracking initiated at the four corners, acoustic emissions in a pillar with a width-to-height ratio of 2.0 under the pressure ratio  $k_o$  of 1.0 are shown as an example.

It can be seen from Figure 24 that acoustic emissions or microcracking first occurs near the four corners. With the increase of loading, acoustic emissions propagate across the pillar. At the same time, microcracks lead to the formation of a shear band across the pillar.

Suorineni et al. [9, 10] asked if the empirical pillar strength formulas are still applicable to pillars subjected to shear

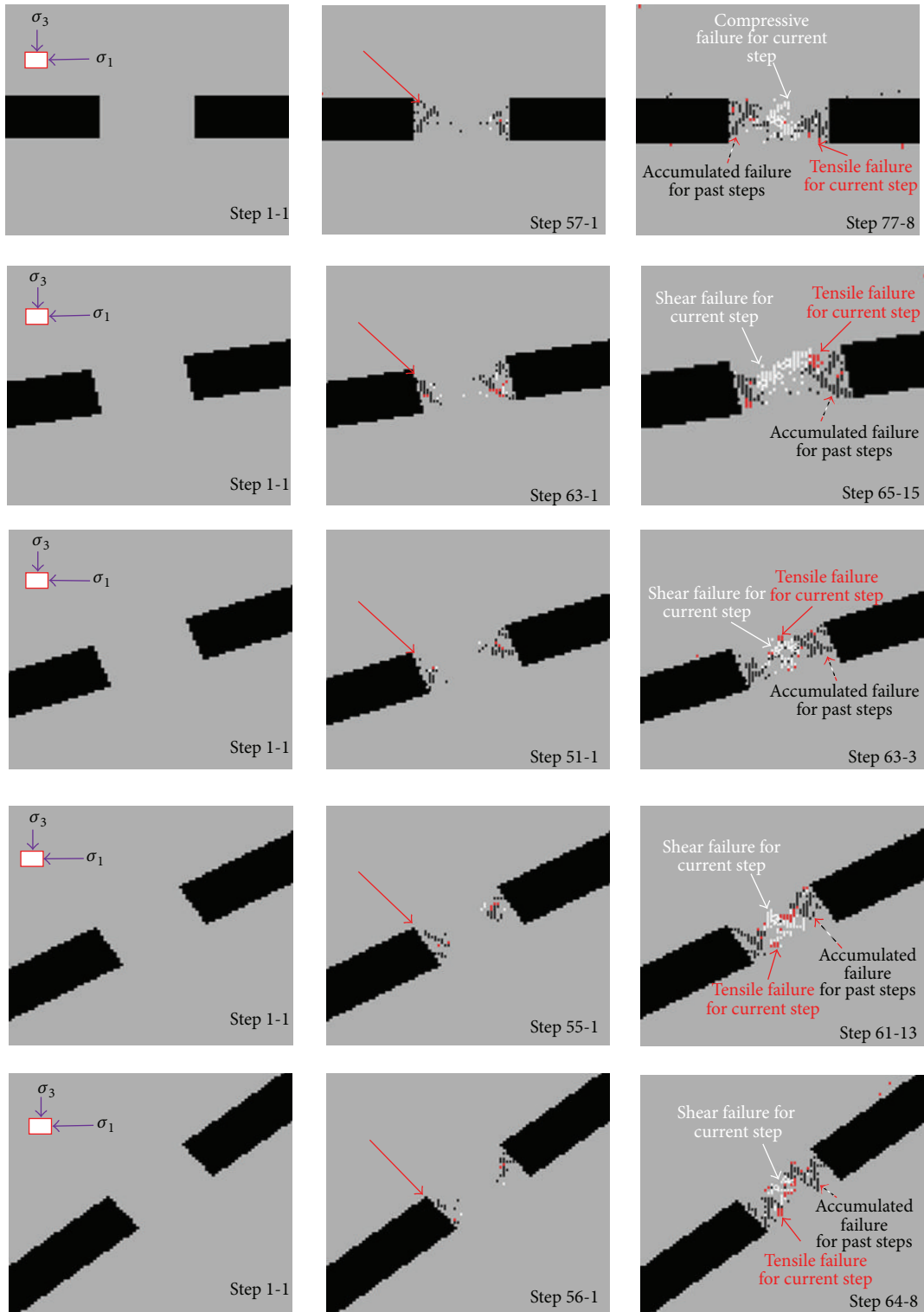


FIGURE 24: Acoustic emissions in the pillar when the dip angle is between 0° and 40°.

loading. The empirical pillar strength formulas for hard rocks are shown in Table 2.

$W$  is the pillar width,  $H$  is the pillar height,  $\sigma_c$  is the uniaxial compressive strength of the pillar intact rock, and  $\sigma_{rm}$  is the pillar rock mass strength.

Why inclined pillars are more prone to shear failure? In Figure 25,  $\sigma_1$  can be decomposed into the axial stress perpendicular to the pillar surface,  $\sigma_1 \cos \theta$  ( $\theta$  is the dip angle of the pillar) and the shear stress acting downward along the pillar surfaces,  $\sigma_1 \sin \theta$ . As the pillar is under

TABLE 2: Empirical formulae for hard rock pillar strength.

Empirical formula	Reference
$\sigma_{rm} = 133 \frac{W^{0.5}}{H^{0.75}}$	[30]
$\sigma_{rm} = 65 \frac{W^{0.46}}{H^{0.66}}$	[31]
$\sigma_{rm} = 35.4 \left( 0.778 + 0.222 \frac{W}{H} \right)$	[32]
$\sigma_{rm} = 0.42 \sigma_c \frac{W}{H}$	[33]
$\sigma_{rm} = 74 \left( 0.778 + 0.222 \frac{W}{H} \right)$	[34]

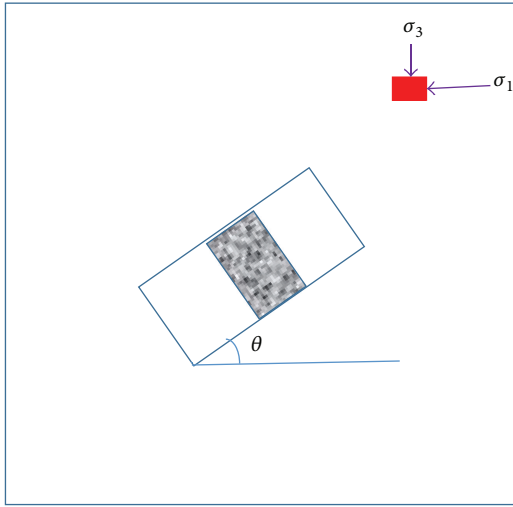


FIGURE 25: Direction of  $\sigma_1$  acting on the pillar at various angles.

compression, its bearing capacity is enhanced. The shear stress acting downward along the pillar surface is a driving force for sliding. The overall shear resistance of the pillar is  $\tau = c + \sigma_1 \cos \theta \tan \varphi - \sigma_1 \sin \theta$  ( $\varphi$  is the angle of internal friction). It indicates that the pillar is more prone to shear failure when the dip angle is greater. This is in agreement with the simulation results by RFPA2D.

4.4. *Verification of Numerical Results against Field Data.* As illustrated in Figure 26 most of failed pillars lie within the 0.5–1.5 width-to-height ratio. It is also noticeable that there are few recorded failed pillars with width-to-height ratio greater than two. Looking at field data very similar trend can be observed. Therefore, the application of empirical formulas is limited to the width-to-height ratios smaller than two. Actually, the empirical curves [28] have wrong trends after width-to-height ratio greater than two. If considering this issue by limit analysis method, the average pillar stress would be infinite, as width-to-height ratio reaches infinite and does not keep a constant like empirical curves.

4.5. *Stress Distribution of Failure Process due to Excavation.* In order to demonstrate the stress distribution of room excavation and pillar failure process, two groups of models were built with inhomogeneous and homogeneous materials

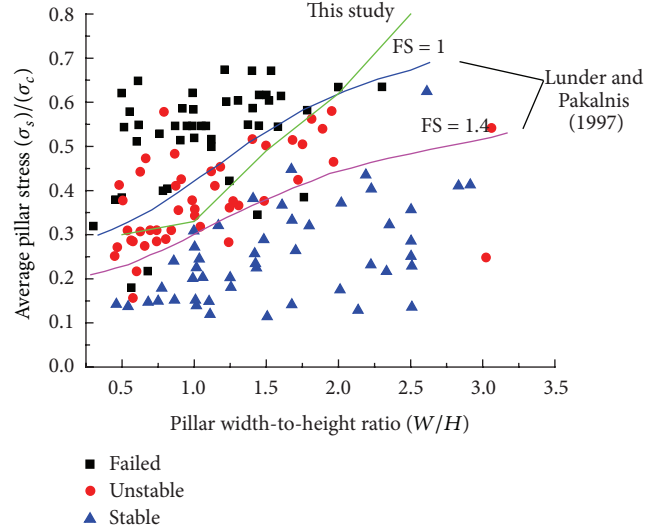


FIGURE 26: The study result superimposed on Lunder and Pakalnis [28] empirical design chart.

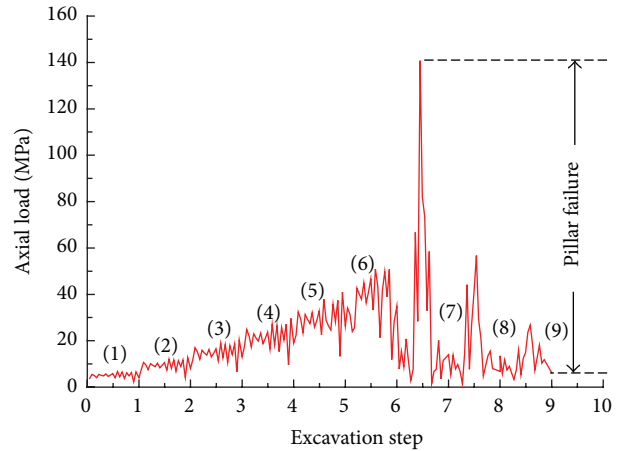


FIGURE 27: Pillar load history as a function of excavation step.

under certain loading condition with the factor of safety less than 1.0. It is easy to observe the failure process during the excavation. The data from Figures 27 to 30 were derived from the midheight of pillar as shown in Figure 4.

(1) *For Inhomogeneous Rock Materials ( $m = 4$ ).* Rock is a kind of inhomogeneous material which embedded much structure planes. Under the external loading, the macroscopical deformation and failure characteristics for rock were determined by the interaction of crack initiation, crack propagation, and crack coalescence. We define  $m$  as the homogeneity index of the rock, which satisfied Weibull distribution. A larger value of  $m$  represents a more homogeneous material and vice versa [29].

Figure 27 illustrated the pattern of stress change within the pillar during the excavation process for width-to-weight ratio equal to 1.5. It can be seen from this figure that, in mining step 7, pillar load drops noticeably indicating the pillar failure. Figure 28 showed the maximum principal stress in the pillars

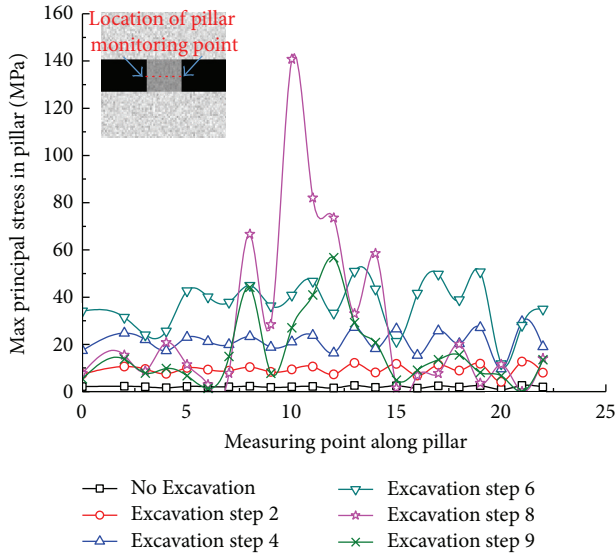


FIGURE 28: Pattern of stress change within the pillar during the excavation process,  $W/H = 1.5$ .

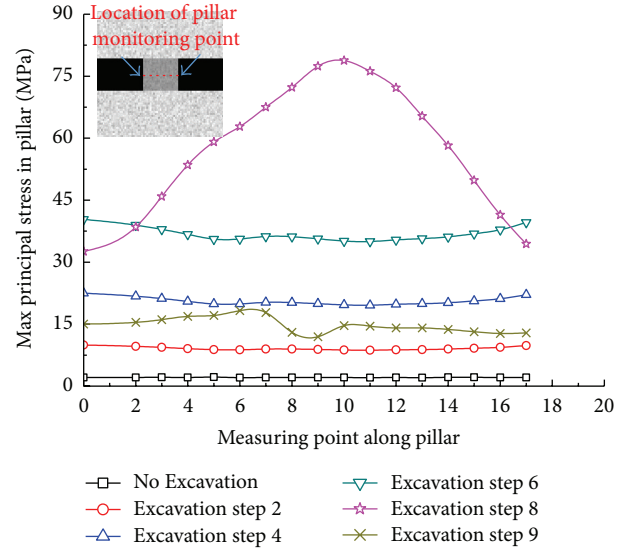


FIGURE 30: Pattern of stress change within the pillar during the excavation process,  $W/H = 1.5$ .

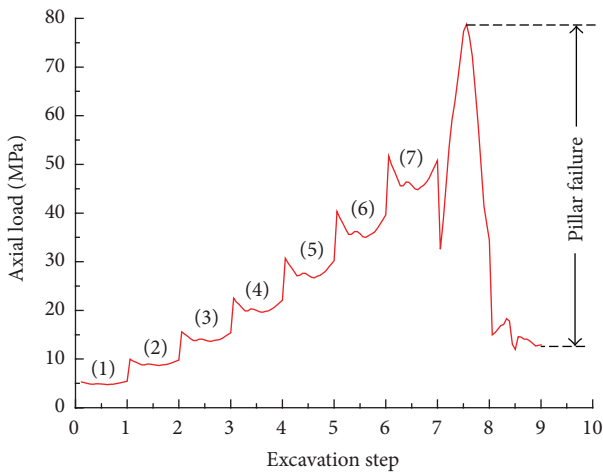


FIGURE 29: Pillar load history as a function of excavation step.

during excavation process. As can be seen from the figure, before excavation, the magnitude of maximum principal stress is equal to the in situ principal stress. As excavation started on both sides of pillar, the maximum principal stress started to build up at the edges of pillars. This is followed by the pillar edge failure leading to stress concentration shifting towards the pillar core (shown in Figure 28 step 7). Pillar core failure implied that the entire pillar lost its support capacity and the stress decreased sharply (shown in Figure 28 step 9).

(2) For Homogenous Rock Materials ( $m = 100$ ). Figures 29 and 30 have the same trend with Figures 27 and 28, however, which curves keep more smoother. Moreover, since homogeneous materials were adopted in this case, stress concentration is insignificant and peak value of curves is less than inhomogeneous materials cases.

### 5. Conclusions

By simulating the failure process of pillars with different dip angles and the stress ratio  $k_o$  using the rock failure process analysis program, the following conclusions can be drawn:

- (1) Shear failure often occurs in orebody under shear loading. The failure of pillars subject to shear stresses is related to the increase of the pressure ratio  $k_o$  and the increase of brittleness.
- (2) The application of empirical formulas is limited to the width-to-height ratios smaller than two. Actually, the empirical curves [28] have wrong trends after width-to-height ratio greater than two, as most empirical design charts and formulas for pillars only consider the axial strength and neglect insufficiency in shear strength. Hence, they are not applicable for orebody under shear loading.
- (3) In a dipping orebody,  $\sigma_1$  acts on the orebody similar to gravity. It has an obliquely downward component. As a result, the pillar under shear stress is more prone to failure. Therefore, the angle between  $\sigma_1$  and the orebody is another factor for pillar rock bursts.
- (4) With increasing dip angle of the pillar, stress concentration first appears at the four corners, leading to microcracking. As the stress in the pillar continuously increases, microcracks gradually coalesce. Subsequently, shear band occurs across the pillar and failure occurs. Therefore, it is inappropriate to neglect the corner stresses for determination of average stress in the pillar.
- (5) The pattern of stress changes within the pillar as excavation proceeds. Elastic stresses start to build up at the pillar edges and stress concentration rises at these points, and the pillar edge failure leads to stress

concentration shifting towards the pillar core. The heterogeneity of rock material has an effect on the pattern of stress concentration in pillars.

## Competing Interests

The authors declare that they have no competing interests.

## Acknowledgments

This research work was supported by the Chinese National Key Basic Research Development Plan (973) (Grant no. 2014CB047100), the Science Fund for Creative Research Groups of the National Natural Science Foundation of China (Grant no. 51421064), and the Chinese National Natural Science Foundation (Grant no. 41572249).

## References

- [1] B. G. H. Brady and E. T. Brown, *Rock Mechanics for Underground Mining*, Allen & Unwin, Boston, Mass, USA, 1985.
- [2] Z. T. Bieniawski, "The effect of specimen size on compressive strength of coal," *International Journal of Rock Mechanics and Mining Sciences*, vol. 5, no. 4, pp. 325–335, 1968.
- [3] P. J. Lunder and R. C. Pakalnis, "Determination of the strength of hard-rock mine pillars," *World Mining Express*, vol. 4, pp. 24–28, 1998.
- [4] C. González-Nicieza, M. I. Álvarez-Fernández, A. Menéndez-Díaz, and A. E. Álvarez-Vigil, "A comparative analysis of pillar design methods and its application to marble mines," *Rock Mechanics and Rock Engineering*, vol. 39, no. 5, pp. 421–444, 2006.
- [5] G. S. Esterhuizen, "An evaluation of the strength of slender pillars," in *Transactions of Society for Mining, Metallurgy, and Exploration*, W. R. Yernberg, Ed., vol. 320, pp. 69–76, Society for Mining, Metallurgy, and Exploration, Littleton, Colo, USA, 2006.
- [6] A. Mortazavi, F. P. Hassani, and M. Shabani, "A numerical investigation of rock pillar failure mechanism in underground openings," *Computers and Geotechnics*, vol. 36, no. 5, pp. 691–697, 2009.
- [7] G. S. Esterhuizen, D. R. Dolinar, and J. L. Ellenberger, "Pillar strength in underground stone mines in the United States," *International Journal of Rock Mechanics and Mining Sciences*, vol. 48, no. 1, pp. 42–50, 2011.
- [8] E. Ghasemi and K. Shahriar, "A new coal pillars design method in order to enhance safety of the retreat mining in room and pillar mines," *Safety Science*, vol. 50, no. 3, pp. 579–585, 2012.
- [9] F. T. Suorineni, P. K. Kaiser, J. J. Mgumbwa, and D. Thibodeau, "Mining of orebodies under shear loading part 1—case histories," *Mining Technology: Transactions of the Institutions of Mining and Metallurgy: Section A*, vol. 120, no. 3, pp. 137–147, 2011.
- [10] F. T. Suorineni, J. J. Mgumbwa, P. K. Kaiser, and D. Thibodeau, "Mining of orebodies under shear loading part 2—failure modes and mechanisms," *Mining Technology: Transactions of the Institutions of Mining and Metallurgy Section A*, vol. 123, no. 4, pp. 240–249, 2014.
- [11] M. Y. Liu and C. Y. Xu, "Stability analysis of pillars in mined-out area," *Mining and Metallurgical Engineering*, vol. 20, no. 1, pp. 20–22, 2000.
- [12] M. C. Yang, "Study on size design method of pillars," *Mining Technology*, vol. 5, no. 3, pp. 10–12, 2005.
- [13] Z. Q. Wang and H. F. Li, "Numerical calculation method for shear safety coefficient of mine pillar," *Journal of Mining & Safety Engineering*, vol. 27, no. 2, pp. 277–280, 2010.
- [14] X. J. Wang, X. Feng, T. B. Yang, K. Zhao, and K. Zhao, "Reasonable width calculation and analysis of artificial pillar in deep mining," *Journal of Mining & Safety Engineering*, vol. 29, no. 1, pp. 54–59, 2012.
- [15] E. Ghasemi, M. Ataei, and K. Shahriar, "An intelligent approach to predict pillar sizing in designing room and pillar coal mines," *International Journal of Rock Mechanics & Mining Sciences*, vol. 65, pp. 86–95, 2014.
- [16] Y. H. Li, S. Q. Nan, X. D. Zhao et al., "Stability of boundary pillars for transition from open pit to underground mining," *Chinese Journal of Rock Mechanics and Engineering*, vol. 24, no. 2, pp. 278–283, 2005.
- [17] Y. W. Zhong, W. Wan, Y. L. Zhao et al., "Safety pillar thickness determination and local monitoring in Wengfu phosphate," *Mineral Engineering Research*, vol. 27, no. 3, pp. 28–33, 2012.
- [18] C. Tang, "Numerical simulation of progressive rock failure and associated seismicity," *International Journal of Rock Mechanics and Mining Sciences*, vol. 34, no. 2, pp. 249–261, 1997.
- [19] C. A. Tang and S. Q. Kou, "Crack propagation and coalescence in brittle materials under compression," *Engineering Fracture Mechanics*, vol. 61, no. 3–4, pp. 311–324, 1998.
- [20] C. A. Tang, W. T. Yang, Y. F. Fu, and X. H. Xu, "A new approach to numerical method of modelling geological processes and rock engineering problems—continuum to discontinuum and linearity to nonlinearity," *Engineering Geology*, vol. 49, no. 3–4, pp. 207–214, 1998.
- [21] C. A. Tang and P. K. Kaiser, "Numerical simulation of cumulative damage and seismic energy release in unstable failure of brittle Rock—part I. Fundamentals," *International Journal of Rock Mechanics and Mining Sciences*, vol. 35, no. 2, pp. 113–121, 1998.
- [22] H. Y. Liu, M. Roquete, S. Q. Kou, and P.-A. Lindqvist, "Characterization of rock heterogeneity and numerical verification," *Engineering Geology*, vol. 72, no. 1–2, pp. 89–119, 2004.
- [23] M. C. He, J. L. Miao, and J. L. Feng, "Rock burst process of limestone and its acoustic emission characteristics under true-triaxial unloading conditions," *International Journal of Rock Mechanics & Mining Sciences*, vol. 47, no. 2, pp. 286–298, 2010.
- [24] G. Manthei and J. Eisenblätter, "Acoustic emission in study of rock stability," in *Acoustic Emission Testing*, C. U. Gross and M. Ohtsu, Eds., pp. 239–310, Springer, Berlin, Germany, 2008.
- [25] G. Q. Chen, T. B. Li, G. F. Zhang, H. Yin, and H. Zhang, "Temperature effect of rock burst for hard rock in deep-buried tunnel," *Natural Hazards*, vol. 72, no. 2, pp. 915–926, 2014.
- [26] M. F. Cai, *Rock Mechanics and Engineering*, Science Press, Beijing, China, 2013.
- [27] E. Hoek and E. T. Brown, "Empirical strength criterion for rock masses," *Journal of the Geotechnical Engineering Division ASCE*, vol. 106, no. GT9, pp. 1013–1035, 1980.
- [28] P. J. Lunder and R. C. Pakalnis, "Determination of the strength of hard-rock mine pillars," *Canadian Institute of Mining Bulletin*, vol. 90, no. 1013, pp. 51–55, 1997.
- [29] C. A. Tang, L. G. Tham, S. H. Wang, H. Liu, and W. H. Li, "A numerical study of the influence of heterogeneity on the strength characterization of rock under uniaxial tension," *Mechanics of Materials*, vol. 39, no. 4, pp. 326–339, 2007.

- [30] D. G. F. Hedley and F. Grant, "Stope-and-pillar design for the Elliot Lake Uranium mines," *Bulletin of the Canadian Institute of Mining and Metallurgy*, vol. 65, pp. 37–44, 1972.
- [31] M. R. Von Kimmelman, B. Hyde, and R. J. Madgwick, "The use of computer applications at BCL limited in planning pillarm extraction and design of mining layouts," in *Proceedings of the ISRM Symposium: Design and Performance of Underground Excavations*, E. T. Brown and J. A. Hudson, Eds., pp. 53–63, British Geotechnical Society, Cambridge, UK, September 1984.
- [32] N. Krauland and P. E. Soder, "Determining pillar strength from pillar failure observations," *Engineering & Mining Journal*, vol. 8, pp. 34–40, 1987.
- [33] Y. Potvin, M. R. Hudyma, and H. D. S. Miller, "Design guidelines for open stope support," *Bulletin of the Canadian Institute of Mining and Metallurgy*, vol. 82, pp. 53–62, 1989.
- [34] J. Sjoberg, "Failure modes and pillar behaviour in the Zinkgruvan mine," in *Proceedings of 33rd U.S. Rock Mechanics Symposium*, J. A. Tillerson and W. R. Wawersik, Eds., pp. 491–500, A. A. Balkema, Rotterdam, The Netherlands, 1992.

## Research Article

# Deformation and Failure Mechanism of Roadway Sensitive to Stress Disturbance and Its Zonal Support Technology

Qiangling Yao,<sup>1,2</sup> Xuehua Li,<sup>1,2</sup> Fan Pan,<sup>1,2</sup> Teng Wang,<sup>1,2</sup> and Guang Wang<sup>1,2</sup>

<sup>1</sup>School of Mines, China University of Mining and Technology, Xuzhou 221008, China

<sup>2</sup>Key Laboratory of Deep Coal Resource Mining (CUMT), Ministry of Education, Xuzhou 221008, China

Correspondence should be addressed to Xuehua Li; [xuehua.cumt@163.com](mailto:xuehua.cumt@163.com)

Received 19 October 2015; Accepted 28 March 2016

Academic Editor: Shimin Liu

Copyright © 2016 Qiangling Yao et al. This is an open access article distributed under the Creative Commons Attribution License, which permits unrestricted use, distribution, and reproduction in any medium, provided the original work is properly cited.

The 6, 63 haulage roadway in the Qidong coal mine passes through a fault zone, which causes severe deformation in the surrounding rock, requiring repeated roadway repairs. Based on geological features in the fault area, we analyze the factors affecting roadway deformation and failure and propose the concept of roadway sensitive to stress disturbance (RSSD). We investigate the deformation and failure mechanism of the surrounding rocks of RSSD using field monitoring, theoretical analysis, and numerical simulation. The deformation of the surrounding rocks involves dilatation of shallow rocks and separation of deep rocks. Horizontal and longitudinal fissures evolve to bed separation and fracture zones; alternatively, fissures can evolve into fracture zones with new fissures extending to deeper rock. The fault affects the stress field of the surrounding rock to ~27 m radius. Its maximum impact is on the vertical stress of the rib rock mass and its minimum impact is on the vertical stress of the floor rock mass. Based on our results, we propose a zonal support system for a roadway passing through a fault. Engineering practice shows that the deformation of the surrounding rocks of the roadway can be effectively controlled to ensure normal and safe production in the mine.

## 1. Introduction

Geological faults can seriously affect coal mining activities. An accurate analysis of fault structure is important for the layout of the mining district and for roadway support design [1, 2]. Most theories used for ground control applications in mines are based on a homogeneous and continuous medium, failing to account for the discontinuity surfaces within the strata such as joints, fissures, and faults. However, the reactivation of joints, fissures, and faults existing in the strata by mining activities inevitably undermines the stability of the roof strata. These issues are discussed by many scholars. For example, Phillips and Hellewell investigated the effect of the activated geological fault on its adjacent ground movement [3]. Yu et al. analyzed the fault activation criterion by mining activities and its characteristics [4]. Since the internal architecture, permeability structure, and hydrologic significance of different faults are also differentiated [5], Hu et al. researched the risk of water inrush near the fault [6]. Islam

and Shinjo studied how the mining-activated fault threatens the roadway stability and the mine safety [7]. Previous studies examined the influences of a normal fault on the physical and mechanical properties of the coal mass and on ground pressure behavior [8]. Rocks in the vicinity of the normal fault are fragmented and become weaker the closer they are to the fault. The fissures within the rocks are less developed when the rocks are further from the fault. The sphere of influence of the fault on the mechanical strength of the rocks is two to four times larger than the fault throw. Shen et al. [9] deem that the fault exerts a significant influence on the adjacent stress field, whose stress intensity and direction are closely related to the scale of the fault, the medium of the fault, the geometrical morphology of the fault, and the boundary conditions. The variation of the principal stress in the vicinity of the fault structure varies from 10° to 90°. Yu et al. used the detailed line observation method to conduct a field survey of the structural plane and divided the rock mass surrounding the fault structure into four zones: the fault zone (0–84 m),

the influence zone of fault (84–117 m), the fracture zone (117–146 m), and the joint zone (146–180 m) [10].

Studies concerning the influence of the fault structure on the rocks surrounding the roadway are scarce, and most do not include an in-depth analysis of the influence of the fault structure. This research aims to bridge these gaps. Taking the 6<sub>1</sub>63 haulage roadway in the Qidong coal mine as a case study, we investigate the deformation and failure mechanism of the roadway that passes through the fault structure zone. We analyze the influence of the fault structure on the advancing stress of the driving work face, the stress state within the surrounding rocks after the roadway excavation, and the sphere of influence of the fault on the stress of the surrounding rocks. Moreover, we compare between the stresses at a roadway located in the fault structure zone and those at a roadway located in the normal zone. Finally, we propose a zonal support technology for haulage roadways.

## 2. Description of Study Site

**2.1. Introduction.** The southern area of the 6<sub>1</sub>63 haulage roadway is the central station for the Southern One mining district and its western area is the ventilation roadway. The northern and eastern areas of the roadway contain the coal mass, where the mining and excavating activities have very little influence on the construction of the 6<sub>1</sub>63 haulage roadway. The designed length of the roadway is 1163.89 m. The layout of the 6<sub>1</sub>63 haulage roadway and the roadways around the study site is illustrated in Figure 1. Mining activity is carried out in the #6 coal seam. The thickness of the coal seam varies between 1.9 and 2.2 m with an average thickness of 2.0 m. The dip angle of the coal seam ranges from 15° to 20° with an average angle of 18°. Based on a comprehensive assessment, the coal seam was identified as a regular coal seam. The roof of the coal seam is mudstone with a thickness of 8–12 m and an average thickness of 10 m. The hardness coefficient of the mudstone varies between 2 and 4. The floor of the coal seam is also mudstone with a thickness of 6 m and a hardness coefficient of 2–3. Excavations have uncovered 13 faults, 600 m in front of the 6<sub>1</sub>63 haulage roadway. All the faults are normal faults, with nine having a fault throw below 2 m and four above 2 m.

Figure 1 shows that the dip angle of most of the faults with a fault throw below 2 m is between 30° and 60°. During the excavation of the roadway, these faults had a small effect on the stress of the surrounding rocks. The deformation of the roadway in this condition is relatively large, but it can be effectively controlled by using high-strength and high-rigidity rock bolts and highly pretensioned anchor cables. For most of the faults with a fault throw above 2 m, the dip angle is between 60° and 70°. During the roadway excavation, these faults had a strong effect on the stress of the surrounding rocks, especially around roadway sections F-2, F-11, and F-12. Both the magnitude of the existing stress and the direction of the principal stress changed. Shallow rocks in the roadway were broken and severe deformation of the rocks surrounding the roadway was observed. Many rock bolts were snapped or sheared off. The original support system was no longer effective in controlling the large deformation of the roadway. In this state, the roadway has to be repaired repeatedly.

**2.2. Factors Influencing Deformation and Failure in Rocks Surrounding the Roadway.** Factors such as the depth of the roadway and the properties and strength of the surrounding rocks have an effect on the deformation and failure mode of the surrounding rocks. The depth of the 6<sub>1</sub>63 haulage roadway is 600 m and the vertical stress of the rocks surrounding the roadway is about 15 MPa. The ribs of the roadway are coal while the roof is 10 m thick mudstone and the floor is 6 m thick mudstone. Water can be seen dripping from the roof and once the roof rock absorbs water, its strength decreases significantly. The strength of the rocks surrounding the roadway is generally weak. Under such high stress conditions, excavation stabilizers are installed to support the surrounding rock; however, it continues to deform slowly.

The structure of the fault also affects the stress state of the roadway rock. The fault structure will result in a high concentration of horizontal stress in some areas of the surrounding rock. Within the fault formation, shallow rocks surrounding the fault are severely broken and sagged mesh with rock fragments can be found in many areas of the roadway. Severe rib spalling is observed at the upper part of the rib, while multiple rock bolts are snapped or sheared off at the lower part of the ribs. Many wood plates are crushed and fractured. In this condition, the roadway is subject to serious deformation and needs to be repeatedly repaired during its service life.

**2.3. Connotation of Roadway Sensitive to Stress Disturbance.** The above analysis suggests that, for a roadway with weak surrounding rocks, the fault structure will cause the failure of the shallow rocks of the roadway as well as changes in the stress state of the rocks surrounding the roadway. Additionally, the fault structure plays an important role in the stability of the roadway. In this paper, we define a roadway with low-strength surrounding rocks which is significantly influenced by the fault structure as a roadway sensitive to stress disturbance (RSSD).

## 3. Deformation and Failure Mechanism of the Surrounding Rocks of RSSD

**3.1. Analysis of Mineral Composition.** Various methods (such as optical microscopy, scanning electron microscopy, and transmission electron microscopy) are used to study the microfabric of rocks [11]. In this study, we use an X-ray diffractometer (model D/Max-3B, made by Rigaku Corporation, Japan) to analyze the mineral composition of the roof of the coal seam. The roof of the #6 coal seam is mudstone with an average thickness of 10 m. The diffraction analysis shows that the roof mudstone consists mainly of quartz, siderite, and clay minerals.

The percentage of clay minerals in the roof mudstone is 73.4% (Table 1). The clay minerals are rich in illite, smectite, and chlorite, which can easily swell after absorbing water (Table 2). The I/S mixed layer ratio is 25%, resulting in a low-strength roof and poor adaptation of the roof to the surrounding environment.

**3.2. Microstructure Characteristics.** To gain a better understanding of the microstructures of the roof mudstone, we

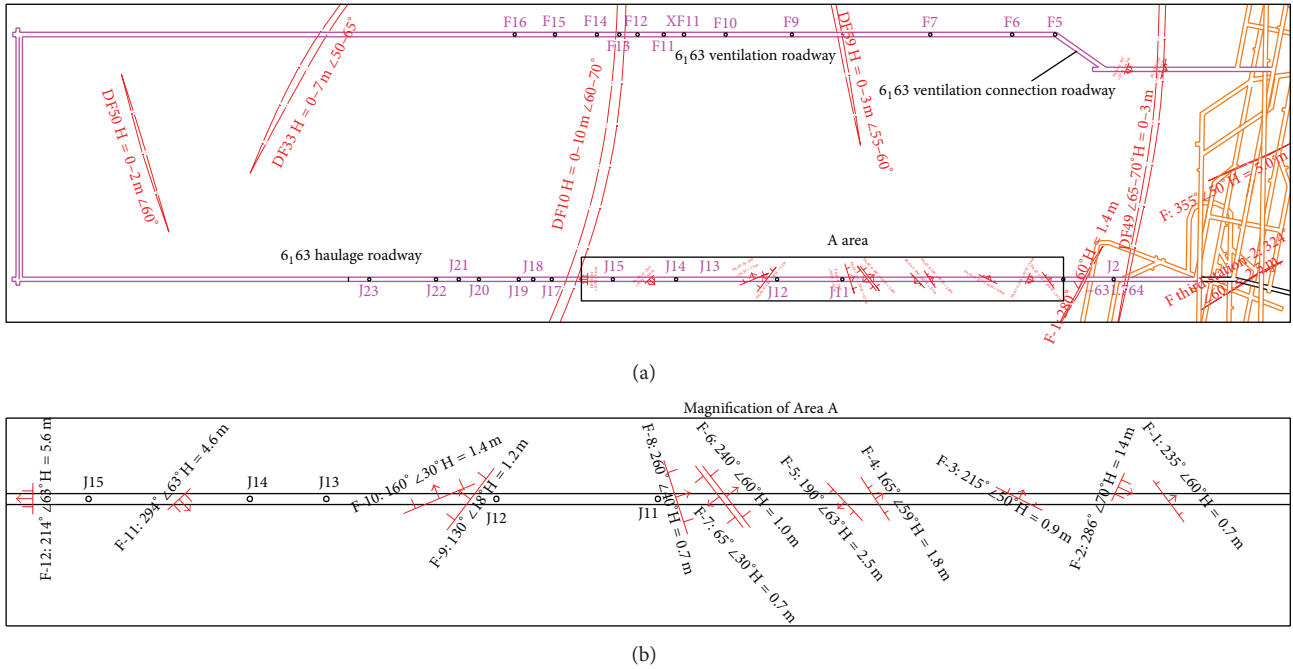


FIGURE 1: Layout of haulage roadway 6<sub>163</sub> and geological conditions around. (a) General view of the roadway; (b) expanded view of Area A.

TABLE 1: X-ray diffraction analysis of roof mudstone.

Stratum	Quartz (%)	Siderite (%)	Clay minerals (%)
Roof mudstone	24.7	1.9	73.4

used the Quanta 200 environmental scanning electron microscope (SEM), made by FEI Corporation, United States, to analyze the mudstone's microstructure characteristics. The SEM images (Figure 2) show that the roof mudstone is very dense and the pores between the clay particles are very small (1–4  $\mu\text{m}$ ). The clay particles are connected in a crystalized manner and the microfractures between the laminated clay beds are large (10–15  $\mu\text{m}$ ). The laminated clay consists mainly of smectite and an illite/smectite mixed layer. The material between the laminated clays is mainly siderite. At magnification of  $\times 3820$  the SEM image shows some clay minerals, which indicates that the laminated clays become soft and decrease in strength after the roof mudstone absorbs water.

**3.3. Fissure Evolution.** A borehole camera (TYGD10, made by Xuzhou Huidun Mining Technology Development Corporation, Ltd., China) was used to record the vertical borehole walls in the 6<sub>163</sub> haulage roadway, providing continuous views of the borehole wall. This provided clear views of the lithology, foliation, bedding planes, and fractures for a comprehensive examination of the fissure evolution in the rocks surrounding the roadway. The borehole detection station was set up in the working face of the roadway (observation station 1) and at a location where the surrounding rocks had already reached stability after excavation (observation station 2). We lay out three boreholes for each station. The boreholes were 32 mm in diameter and 8000 mm long. After analyzing the

records of the six boreholes, we captured some screenshots (Figure 3) and conducted statistical analysis on the fissure images. We found horizontal fissures and longitudinal fissures in the rocks surrounding the roof. The horizontal and longitudinal fissures evolve to bed separation and fracture zones or become fracture zones accompanied by numerous new fissures that extend deeper rock (Figure 4).

Figures 5(a) and 5(b) show the borehole sections of stations 1 and 2, respectively, showing the fissure types and the rock state observed by the borehole camera. The horizontal fissure and longitudinal fissure are the two basic fissure types in the rocks surrounding the roof, with the former being dominant. As the working face of the roadway advances, rocks within 1 m of the roof become fracture zones and fissures within the anchorage zone of the rock bolt start to develop, accompanied by numerous newly created fissures, among which the horizontal fissures are dominant. Of the fissures that are out of the anchorage zone of the rock bolt but within the anchorage zone of the anchor cable, the horizontal ones generally develop to bed separation while both the horizontal and the longitudinal ones can become fracture zones and expand to deeper areas. In this process, numerous new fissures are created, most of them horizontal fissures. The number of fissures, degree of fissure development, and number of newly created fissures are higher in the lower part of the borehole than in the middle part, with the upper part of the borehole having the least amount.

**3.4. Field Monitoring of the Deformation of Rocks Surrounding the Roadway.** To monitor the deformation of the roadway surrounding rock, extensometers recording the rock displacement at different depths were arranged in the roof and rib. The strain is calculated by dividing the relative

TABLE 2: X-ray diffraction analysis of clay minerals.

Stratum	Clay minerals (%)			Mixed layer ratio (%)
	I/S	K	C	I/S
Roof mudstone	33	65	2	25

S: smectite, I: illite, K: kaolinite, C: chlorite, and I/S: illite/smectite mixed layer.

TABLE 3: Physical and mechanical properties of the strata.

Stratum	Density [ $\text{kg}\cdot\text{m}^{-3}$ ]	Bulk modulus [GPa]	Shear modulus [Gpa]	Friction angle [ $^{\circ}$ ]	Cohesion [Mpa]	Tensile strength [Mpa]
Roof	2300	3.3	1.9	23	0.13	0.7
#6 coal seam	1350	2.5	1.45	20	0.15	0.2
Floor	2400	3.6	201	25	0.19	0.8

displacement at the extensometer with its depth. Using the primary and secondary bearing zone theory, we analyzed the monitoring data of the displacement of the deep rocks and divided the deep rocks into those in the tension zone and in the compression zone. The tension zone refers to areas where the strain is positive while the compression zone refers to areas where the strain is negative. In Figure 6, the horizontal axis, denoted by  $L$ , represents the distance to the roadway roof or to the roadway rib; the vertical axis, denoted by  $\epsilon$ , represents the strain value.

The tension zone and compression zone in the roof and the lower rib change alternatively with time (Figure 6), indicating the deformation and stress state of the deep rock surrounding the roof and the lower rib. In the roof, within 0–1 m, the surrounding rock is fragmented; within 1–2.5 m, the rocks are in the tension zone, where the rock deformation is mainly dilation; within 2.5–4.5 m, the rocks gradually transit from the tension zone to the compression zone, indicating the gradual closure of the separating bed; between 4.5 and 7 m, the rocks transit from the compression zone to the tension zone step by step, showing that bed separation is occurring in this zone. The dilation of the shallow rocks and the separation of the deep rocks account for the sagging and deformation of the roof, with the former playing a dominant role. In the lower rib, the surrounding rock deformation is mainly a result of the dilation of the shallow rocks; within 1–2 m, the rocks are in the tension zone, where the rocks deform in the form of dilation; within 2–4 m, the rocks gradually transit from the tension zone to the compression zone, indicating the gradual closure of the separating bed. In the upper rib, the surrounding rock deformation is caused mainly by the dilation of the shallow rocks and the separation of the deep rocks, with the separation greater than the dilation; within 1–3.5 m, the rocks are in the tension zone, where the shallow rocks deform in the form of dilation and the deep rocks deform in the form of separation; within 3.5–4 m, the rocks gradually transit from the tension zone to the compression zone, indicating the closure of the separating bed.

To effectively control the stability of the surrounding rocks and decrease the deformation volume, the traditional way of supporting the roadway should be upgraded. In

addition to the selection of high-strength and high-rigidity rock bolts and anchor cables, the pretension of the bolts and cables must be appropriately considered. In so doing, the dilation of the shallow rocks and the separation of the deep rocks can be better restrained, which will significantly improve the stability of the roadway.

*3.5. Numerical Study of the Influence of the Fault on the Stress State.* The FLAC<sup>3D</sup> numerical simulation software can be used to simulate a discontinuity surface such as a fault or a joint and the Mohr-Coulomb model is adopted [12]. In this study, we used FLAC<sup>3D</sup> to simulate the effect of the fault structure on the stress state of the rocks surrounding the roadway during roadway excavations through the faults (Table 3 and Figure 7).

Based on a previous study [13], we determined the mechanical parameters of the fault as follows: normal stiffness of 1.5 GPa/m, shear stiffness of 0.5 GPa/m, an internal friction angle of 33 $^{\circ}$ , and cohesion of 0 MPa. As mentioned in Section 2, the depth of the #6 coal seam is 600 m and its thickness is 2 m. The roof of the roadway is 10-meter-thick mudstone and the floor of the roadway is 6-meter-thick mudstone. In this study, we use the Interface command to simulate the fault, with a dip angle of 60 $^{\circ}$  and a fault throw of 5 m. The rectangular roadway is 4 m in width and 2 m in height, driving along the roof and floor of the coal seam.

As shown in Figure 8, there are two ways for the roadway to pass through the fault. The first is from the hanging wall to the foot wall, which requires the roadway to rise at an angle of 19 $^{\circ}$  when the horizontal distance between the hanging wall and the fault plane is 12 m. The roadway will be continuously excavated until the foot wall of the fault is uncovered. Then, the roadway will drive along the roof and floor of the coal seam. The second path is from the foot wall to the hanging wall, which requires the roadway to drive along the roof and floor until it reaches the fault plane and then dip at an angle of 19 $^{\circ}$ . The roadway will then be continuously excavated until the hanging wall of the fault is uncovered and then will continue to drive along the roof and floor of the coal seam.

We performed ten simulations of the roadway excavation. For the fourth to seventh simulations, the excavation step

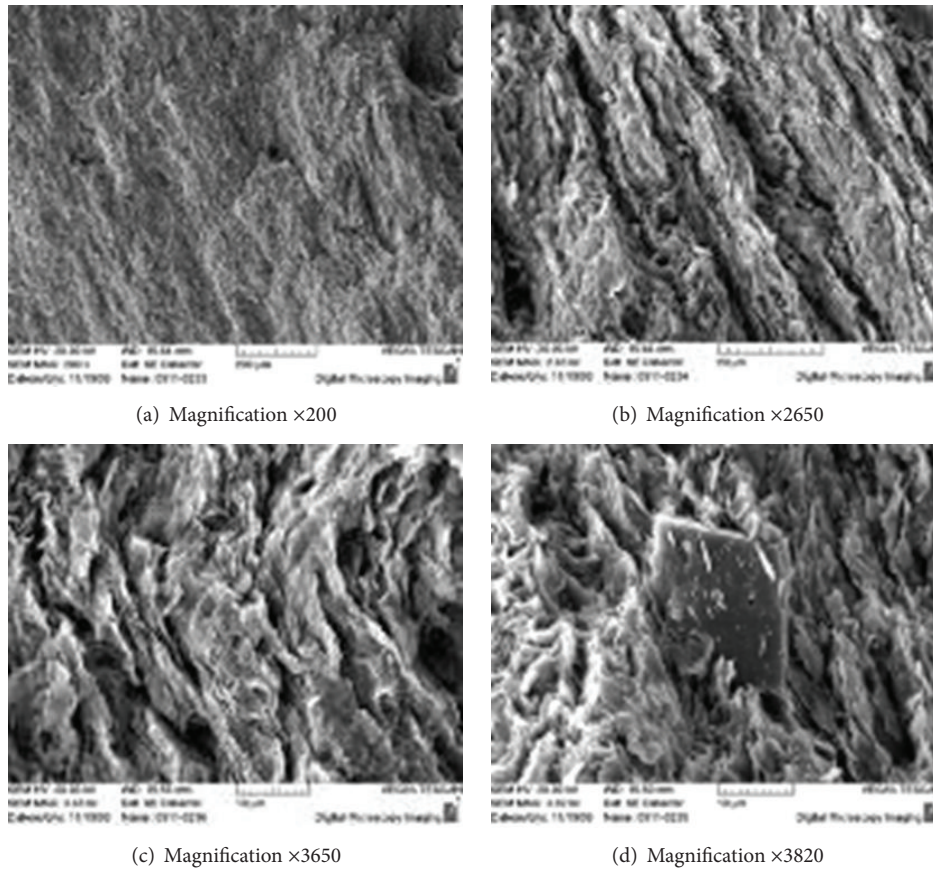


FIGURE 2: Scanned electron microscope images of the mudstone specimens extracted from the roof.

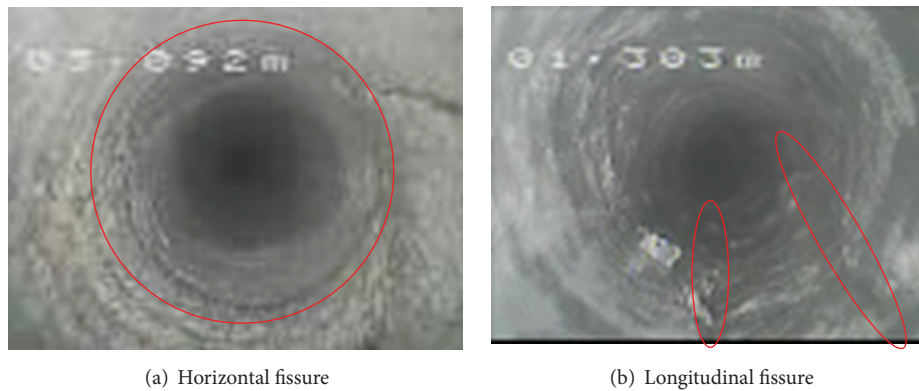
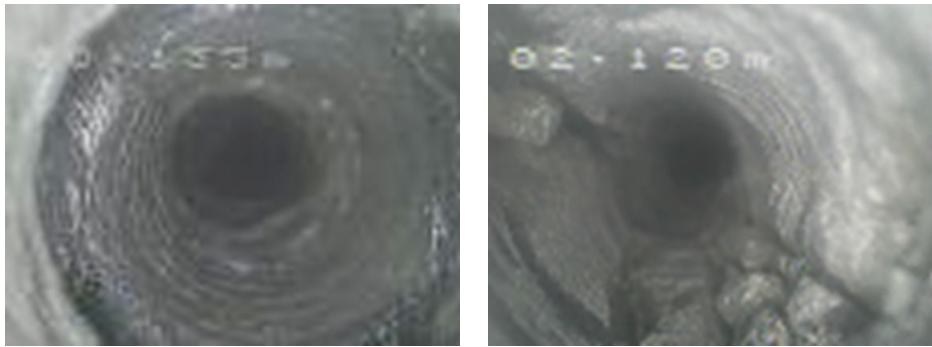


FIGURE 3: Main fissures emerged initially after excavation.

is 4 m while for the other cases the excavation step is 10 m. During the whole excavation, ten simulated observation stations are laid out to monitor the stress changes within the rocks surrounding the roadway. For each station, we set up a monitoring point at a depth of 0.5 m in the roof, rib, and floor. During the simulation run, these monitoring points record the real-time changes of the horizontal stress and vertical stress. The recorded data will help to identify the effect of the fault structure on the stress state of the surrounding rocks.

The vertical stress in the surrounding rocks recorded when the roadway passed from the hanging wall to the foot wall is illustrated in Figures 9 and 10. Through further analysis, we draw the following conclusions:

- (1) During the excavation, the vertical stress caused by the advancing roadway within the fault structure zone is larger than that within the normal zone. The fault exerts a more significant influence on the two ribs of the roadway than on its roof. After passing the fault,



(a) Bed separation

(b) Fractured zone

FIGURE 4: Evolution of fissures into bed separation and a fractured zone.

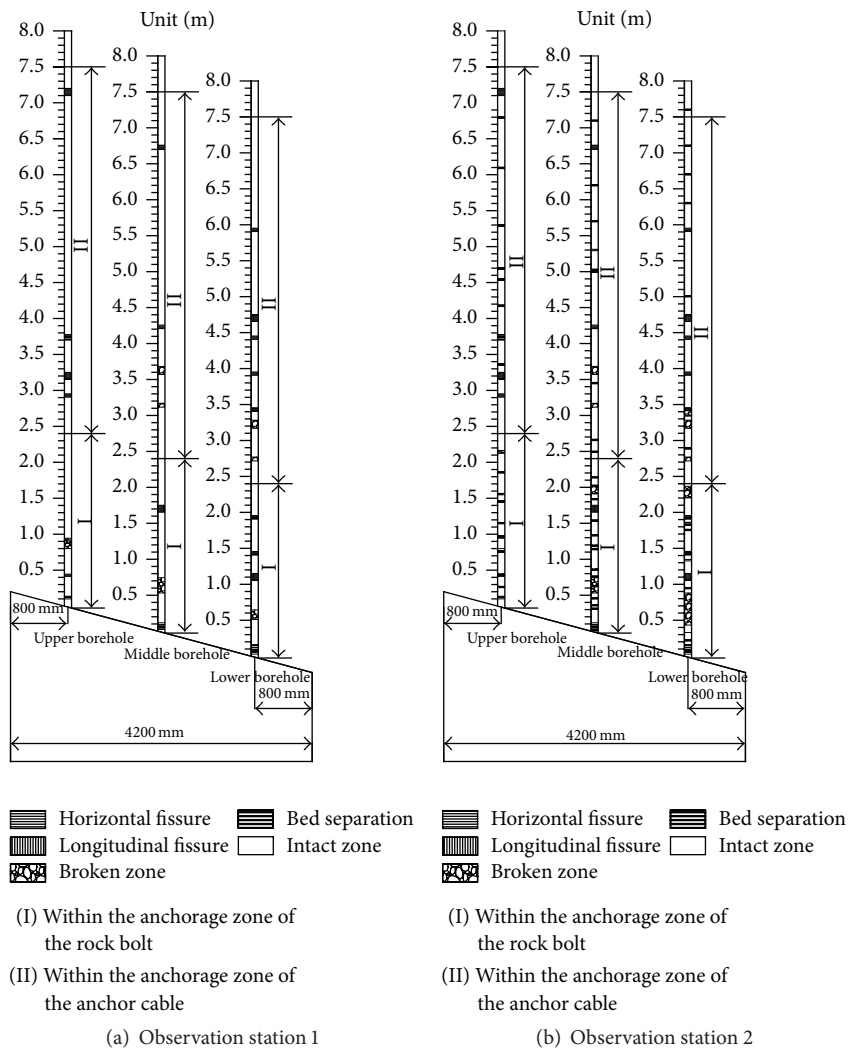


FIGURE 5: Collection of borehole imaging results and its categorization.

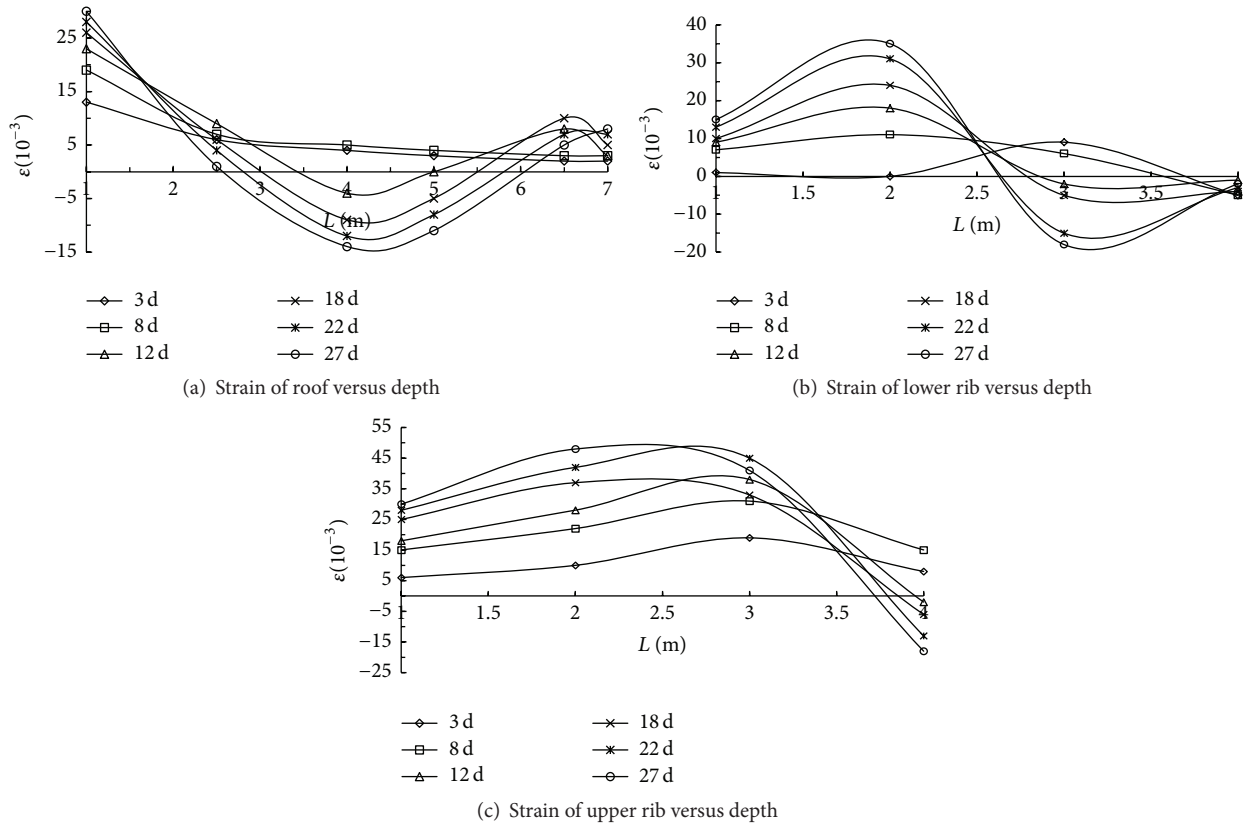


FIGURE 6: Strain of the roadway surrounding rock versus depth (recorded at different times).

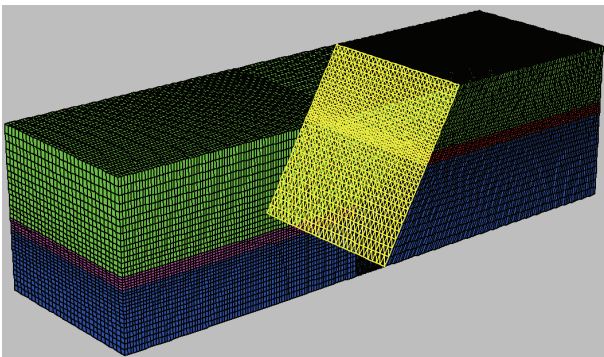


FIGURE 7: Numerical model.

the advancing vertical stress gradually decreases and stabilizes.

- (2) After the excavation, the vertical stress of the roof rock mass within the fault structure zone is slightly different from that in the normal zone. While the stress in the rock mass of the floor and along the ribs is relieved, the vertical stress gradually increases with decreasing distance between the roadway and the fault plane.
- (3) The advancing vertical stress and the vertical stress following the excavation of the roadway within the

fault structure are always larger than those within the normal zone. For the roadway ribs, the advancing vertical stress and the vertical stress after excavation are 1.17 and 1.35 times those in the normal zone, respectively. For the roadway floor, the advancing vertical stress and the vertical stress after excavation are 1.04 times and 2.29 times those in the normal zone, respectively.

The sphere of influence of the fault on the stress of the surrounding rocks is about 30 m. When the roadway passed from the hanging wall to the foot wall, the fault exerts a maximum impact on the vertical stress of the rib rock mass and a minimum impact on the vertical stress of the floor rock mass while the fault's influence on the vertical stress of the rocks surrounding the roof is medium.

Figures 11 and 12 present the monitoring results of the vertical stress of the surrounding rocks when the roadway passes from the hanging wall to the foot wall. Through further analysis, we draw the following conclusions:

- (1) During the excavation, the difference between the advancing horizontal stress in the roof and the rib rock mass of the roadway within the fault structure zone and that within the normal zone is small. The advancing horizontal stress in the floor rock mass of the roadway within the fault structure zone is smaller than that within the normal zone. However, when the roadway is within the influencing sphere of the

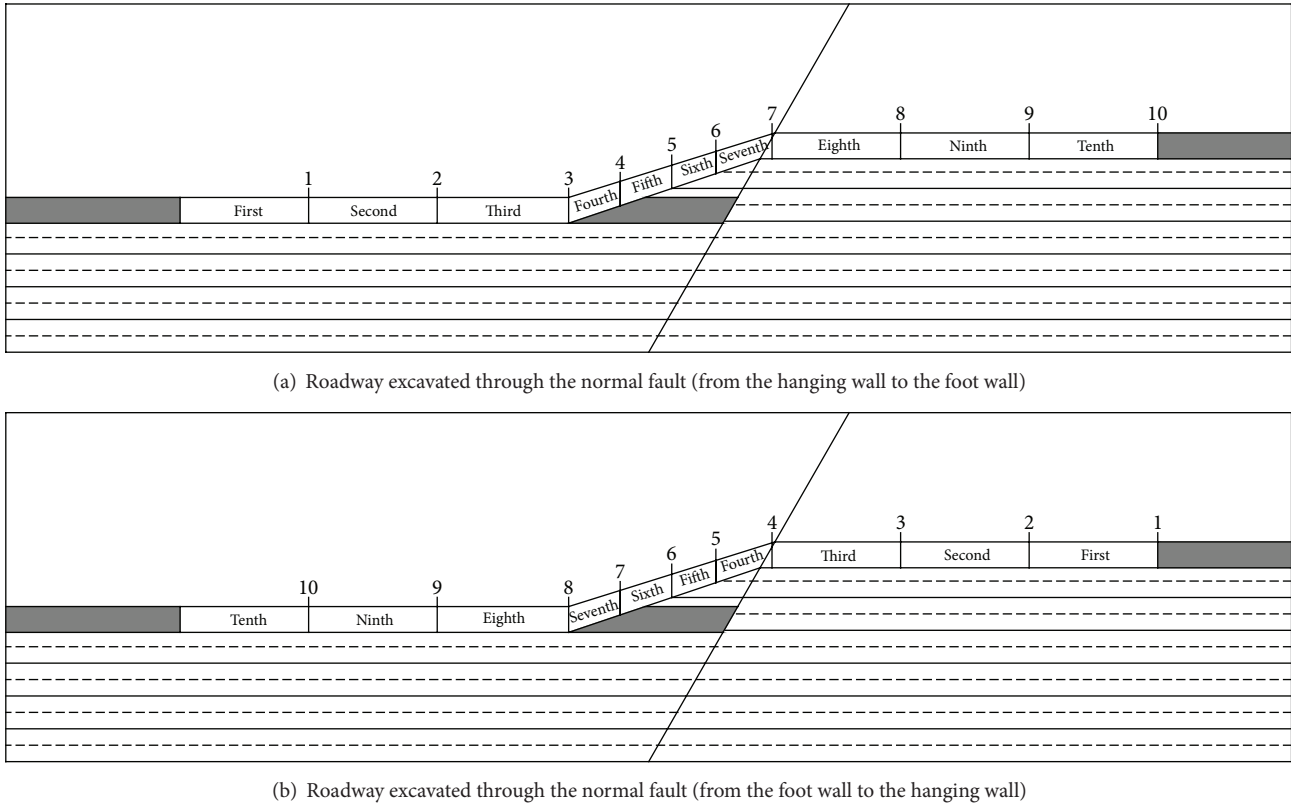


FIGURE 8: Simulated roadway excavation process and the layout of observation stations. Note: first to tenth denotes the excavation sequence; one to ten denotes the observation station.

hanging wall of the fault, the advancing horizontal stress in the floor rock mass gradually increases as the distance between the roadway and the fault plane decreases.

- (2) The advancing horizontal stress and the horizontal stress following the excavation for the roadway within the fault structure are always larger than those within the normal zone. For the roadway roof, the advancing horizontal stress is 1.14 times that in the normal zone and the horizontal stress after excavation is 1.19 times that in the normal zone. After the roadway passes the fault, the horizontal stress in the roof after excavation gradually grows. For the roadway ribs, the advancing horizontal stress is 1.16 times that in the normal zone and the horizontal stress after excavation is 1.72 times that in the normal zone.
- (3) After excavation, the horizontal stress in the floor rock mass for the roadway within the fault structure zone is larger than that within the normal zone. A concentration of horizontal stress is observed in the floor. The concentrated stress is 18.6 MPa, with a concentration coefficient of 1.62.

The sphere of influence of the fault on the stress of the surrounding rocks is about 30 m. When the roadway passes

from the hanging wall to the foot wall, the fault exerts a maximum impact on the horizontal stress of the floor rock mass and a minimum impact on the horizontal stress of the roof rock mass while the influence of the fault on the vertical stress of the roof rock mass is medium.

#### 4. Zonal Support Mechanism and Technology for RSSD

*4.1. Roadway Zonal Support Mechanism.* According to the curves in Figures 9, 10, 11, and 12, which are obtained from the numerical simulation, the effect of the fault on the advancing stress in the rocks surrounding the roadway is small. However, following the excavation of the roadway, the effect of the fault on the stress state of the surrounding rocks is much stronger. The scope of influence of the fault on the stress state of the surrounding rocks varies between 27 and 30 m. Based on the numerical results, we put forward the mechanism of zonal support for RSSD (Figure 13).

The first step in the zonal support system for RSSD is to regionalize the roadway along the excavating direction. Areas within 30 m before and after the fault structure are designated as the fault structure zone, while the remaining areas are regarded as the normal zone (Figure 14). The fault structure zone and the normal zone will be supported

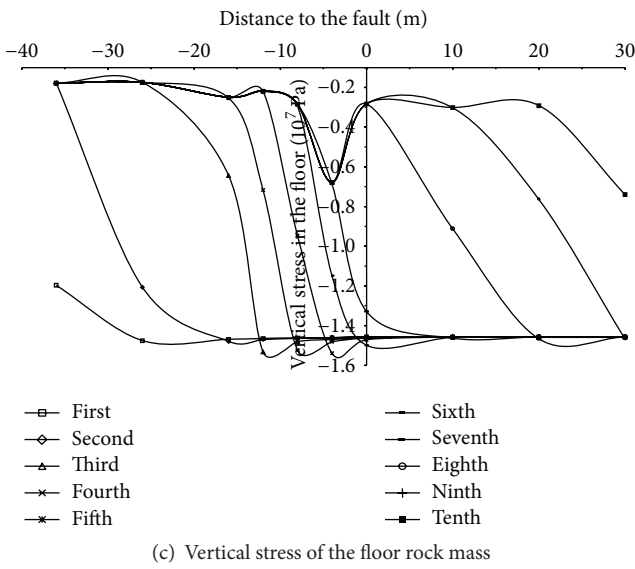
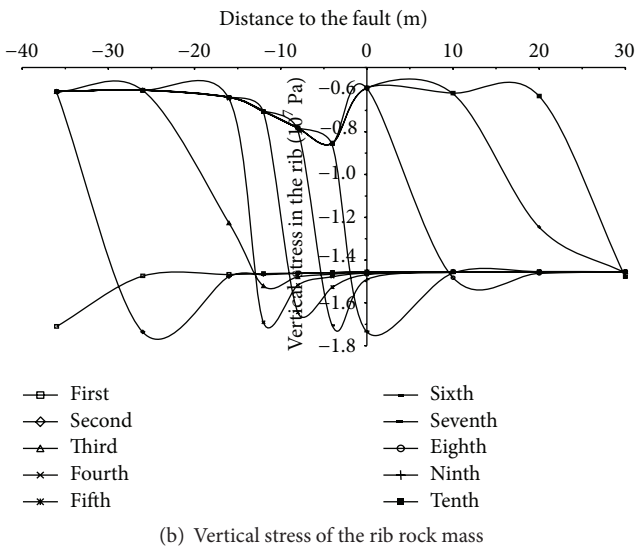
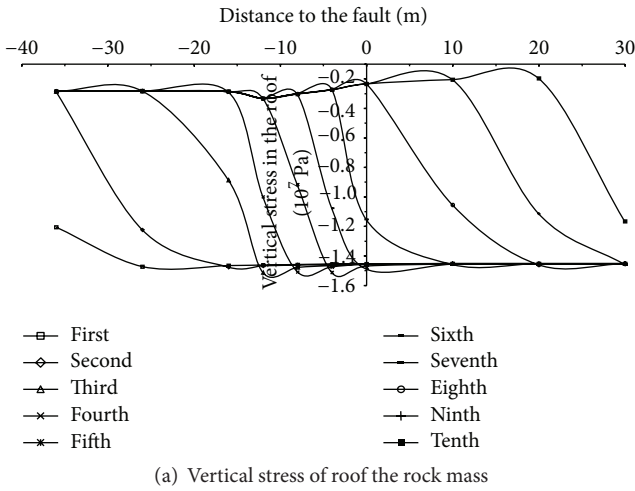


FIGURE 9: Vertical stress of the surrounding rocks when the roadway passes from the hanging wall to the foot wall of the fault. Note: first to tenth denotes the excavation sequence.

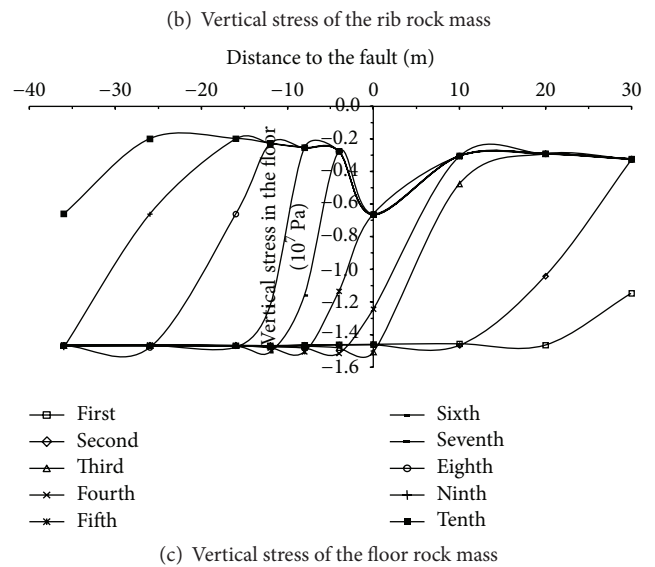
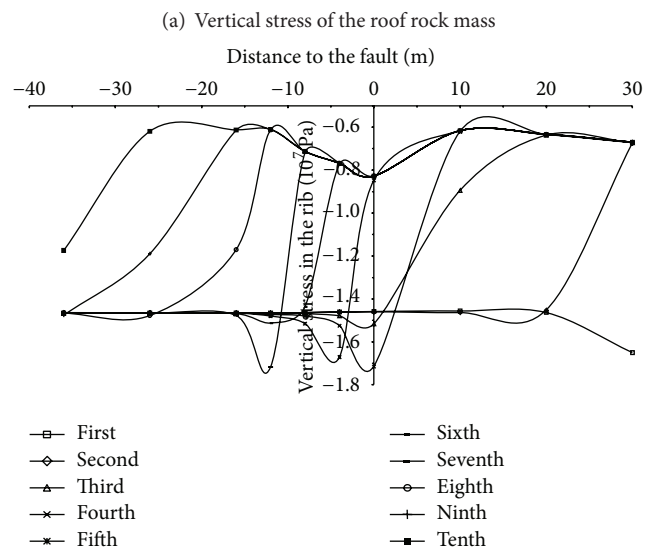
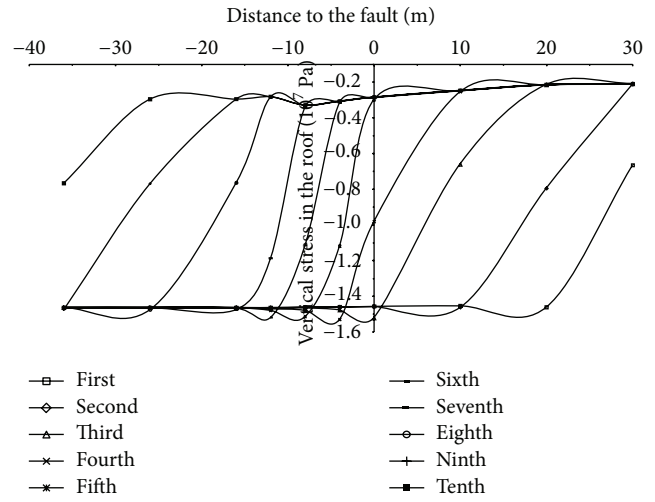
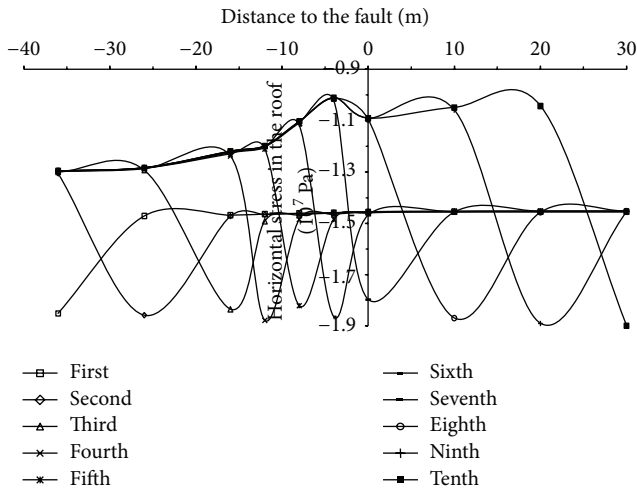
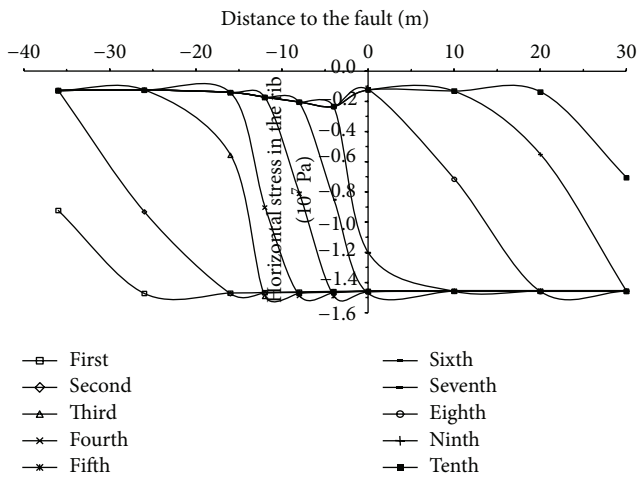


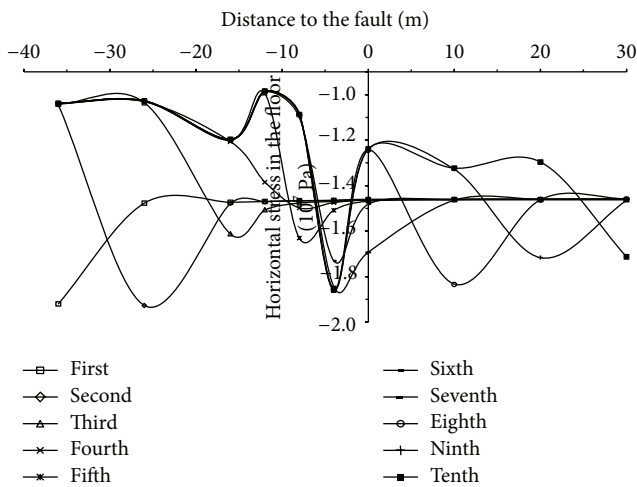
FIGURE 10: Vertical stress of the surrounding rocks when the roadway passes from the foot wall to the hanging wall of the fault. Note: first to tenth denotes the excavation sequence.



(a) Horizontal stress of the roof rock mass

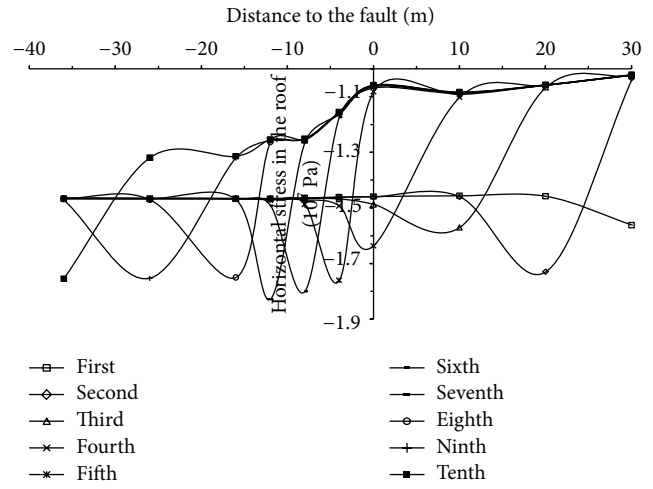


(b) Horizontal stress of the rib rock mass

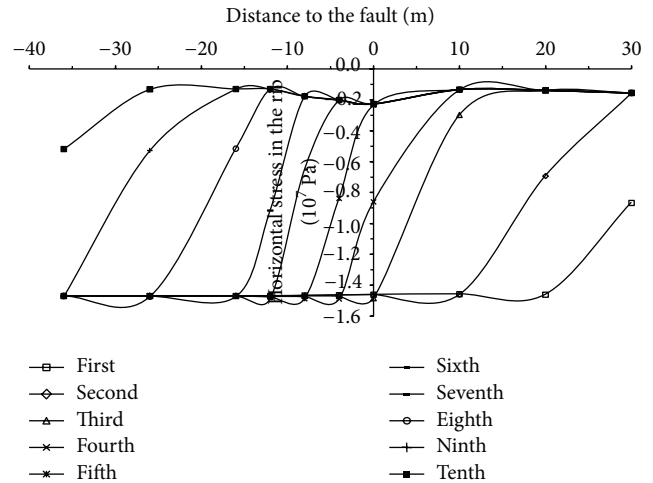


(c) Horizontal stress of the floor rock mass

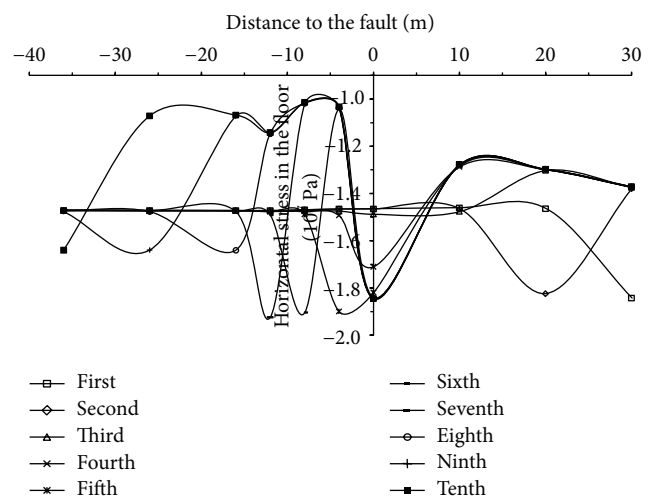
FIGURE 11: Horizontal stress of the surrounding rocks when the roadway passes from the hanging wall to the foot wall of the fault. Note: first to tenth denotes the excavation sequence.



(a) Horizontal stress of the roof rock mass



(b) Horizontal stress of the rib rock mass



(c) Horizontal stress of the floor rock mass

FIGURE 12: Horizontal stress of the surrounding rocks when the roadway passes from the hanging wall to the foot wall of the fault. Note: first to tenth denotes the excavation sequence.

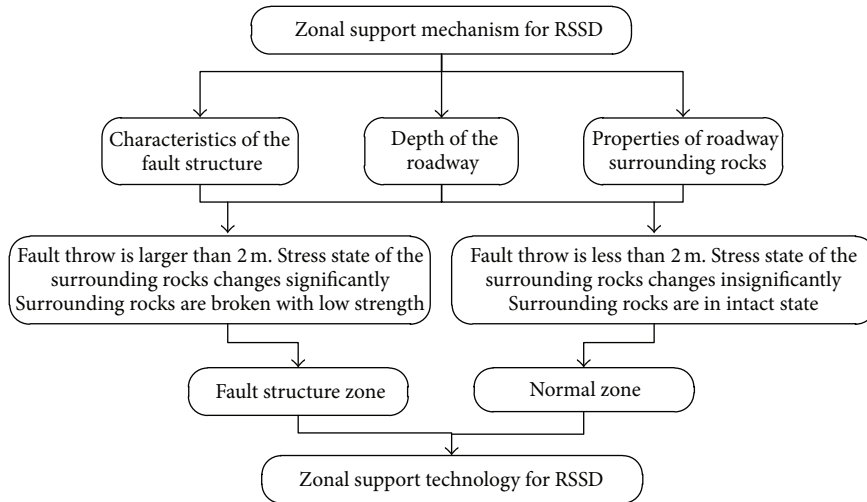


FIGURE 13: Zonal support mechanism for RSSD.

FIGURE 14: Diagram of zonal support for the h<sub>6,63</sub> haulage roadway.

by respective schemes to ensure the stability of the roadway.

**4.2. Roadway Zonal Support Technology.** The preliminary support scheme for the h<sub>6,63</sub> haulage roadway is illustrated in Figure 15. The specific support parameters are as follows:

- (1) The rock bolt and anchor cable use 2 and 3 resin cartridges of the Z2350 type.
- (2) The roof bolts are connected to a steel beam, which has six holes and is 4.2 m long. The rock bolts for the upper rib are connected with two steel straps, which have three holes and are 1.8 m long. The rock bolts for the lower rib are connected with 2.2 m long steel straps with four holes.
- (3) The screen mesh for the roof is steel mesh with rhombic holes, while for the two ribs plastic mesh is fitted. Both the steel mesh and plastic mesh are 1000 × 5000 mm mesh. In the upper corner of the roadway, steel wire is used to bind the steel mesh with the plastic mesh. The overlapping width of the two meshes is larger than 100 mm, while the binding interval is less than 150 mm.

- (4) The pretightening torque of the roof and rib bolts is higher than 200 N·m. The pretension of the anchor cable is higher than 120 kN.

The monitoring results of the ground pressure in the roadway model with the preliminary support scheme show that when the roadway passes near the fault structure, serious deformation of its two ribs is observed as well as considerable settling of the roof. In view of this, we upgraded the preliminary support scheme as illustrated in Figure 16. Several parameters were changed, as follows:

- (1) A right-handed thread steel rock bolt of size  $\Phi 20 \times 2400$  mm replaced the left-handed thread steel rock bolt of size  $\Phi 18 \times 2000$  mm to control the serious deformation of the two ribs. The rod body of the right-handed rock bolt is fully threaded and the nut can be directly installed on the rod body. Thus, once the rib spalls, the rock bolt can be tightened again to maintain its pretension.
- (2) The space of the rock bolt and anchor cable remains unchanged, but the array pitch was changed to 700 mm.
- (3) For the roadway within the fault structure zone, the surrounding rock deformation is caused mainly by

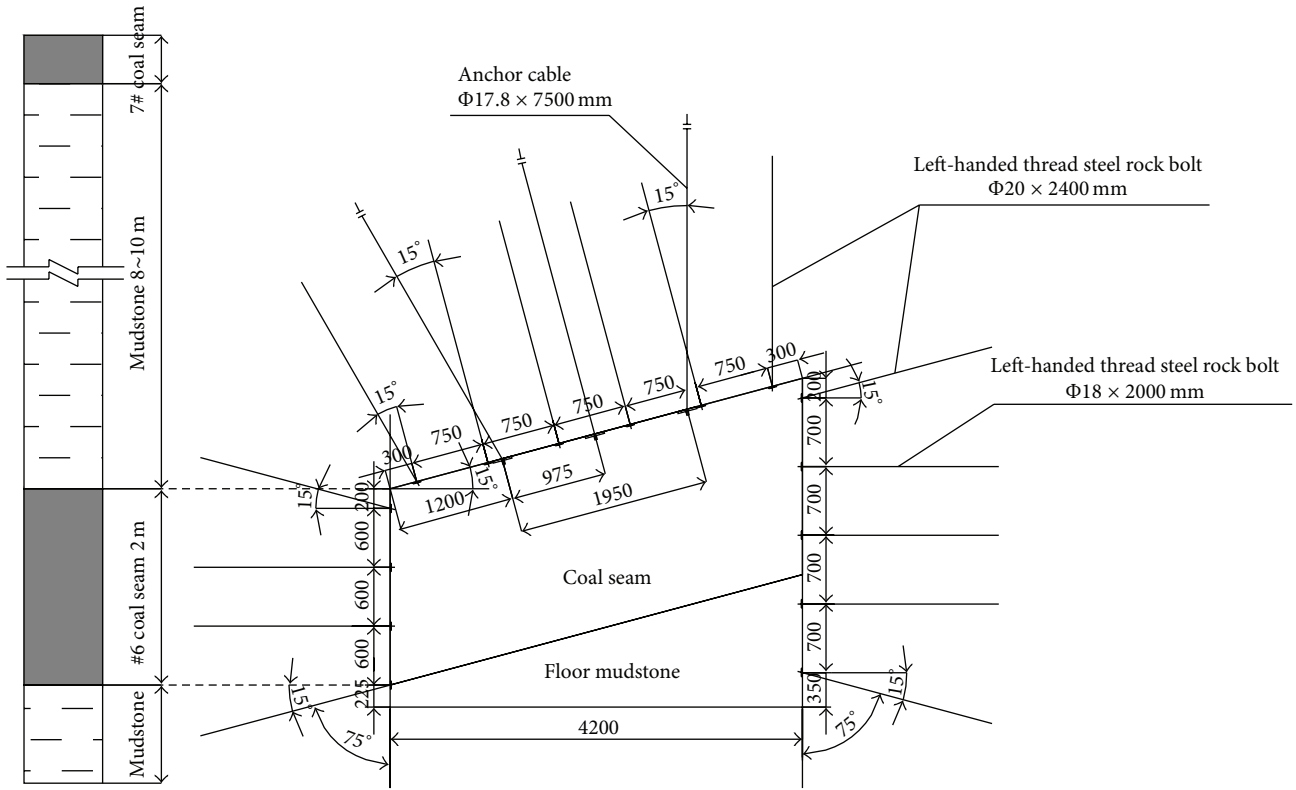


FIGURE 15: Preliminary support scheme.

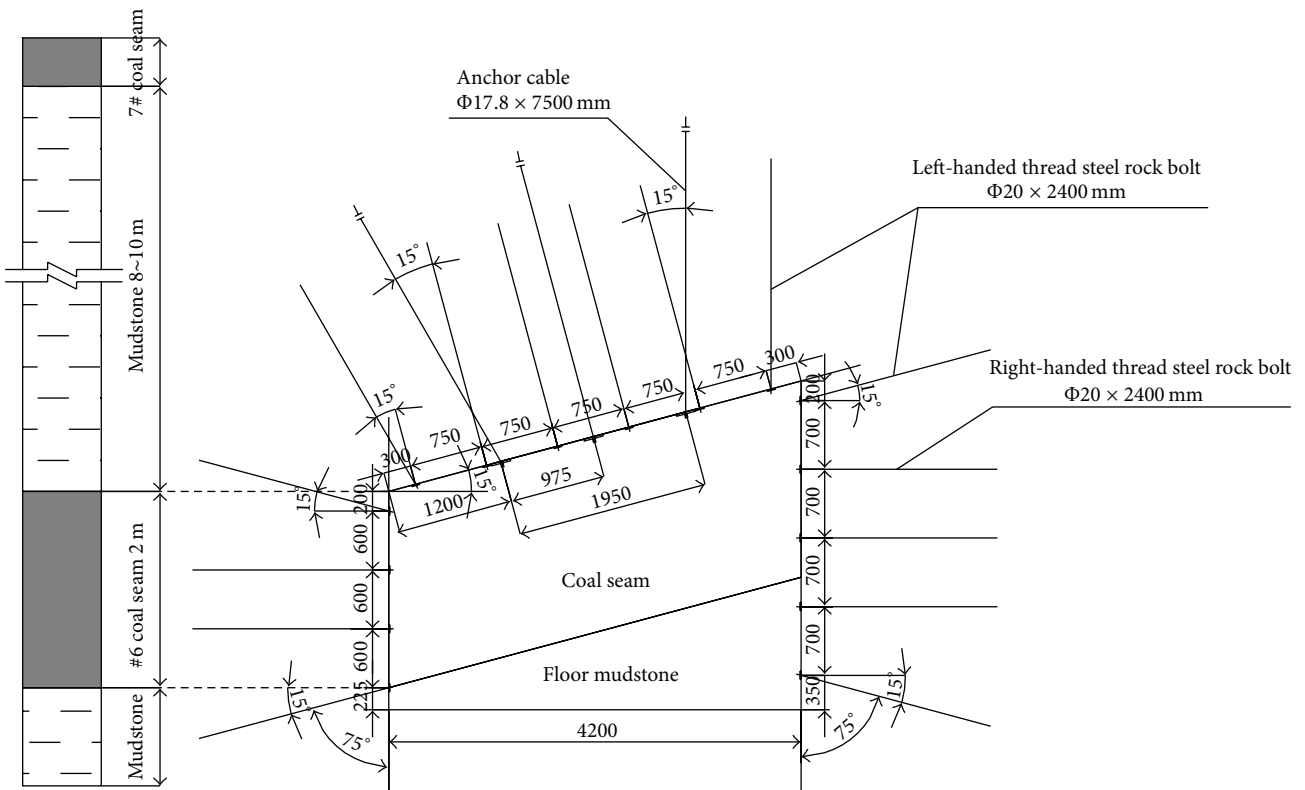


FIGURE 16: Final support scheme for the roadway within the fault structure zone.

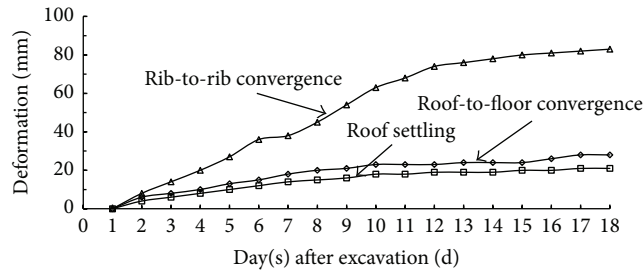


FIGURE 17: Roadway deformation after excavation versus time.

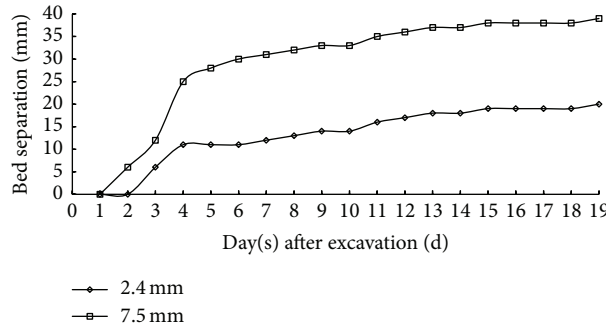


FIGURE 18: Bed separation of the roof after excavation versus time.

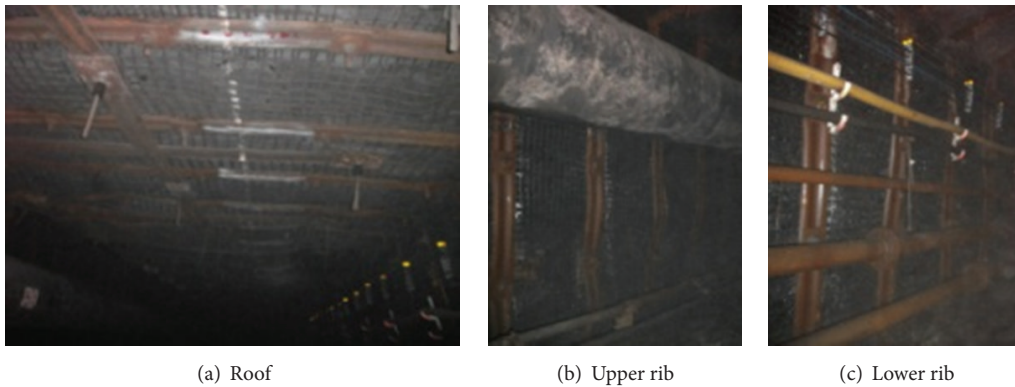


FIGURE 19: Roadway conditions after final support.

the dilation of the shallow rocks and the separation of the deep rocks. Thus, the pretightening torque of the roof bolt and rib bolt is set at 300 and 200 N·m, respectively. The pretension of the anchor cable is set at 150 kN.

### 5. Engineering Practice

The essence of controlling the rock surrounding the roadway is to control the deformation volume of the roadway and ensure a sufficient excavation profile for the normal and safe production in the mine. Therefore, the deformation volume of the rocks surrounding the roadway is chosen as the main indicator in evaluating the control effect [14, 15].

The deformation of the surrounding rocks of the 6<sub>1</sub>63 haulage roadway is small (Figure 17). Fifteen to eighteen days

after the excavation, the accumulative volume of the roof-to-floor convergence is about 30 mm; the accumulative volume of the roof settling is 20–25 mm and that of the rib-to-rib convergence is 95–105 mm.

Figure 18 shows that roof separation of the 6<sub>1</sub>63 haulage roadway occurs 4 to 6 days after the excavation. At a point 7.5 m within the roof, the separation volume is 39 mm and at 2.4 m within the roof, the separation volume is 20 mm (Figure 19).

### 6. Conclusions

- (1) We investigated the geological features and analyzed the factors affecting the deformation and failure of the roadway within the fault structure zone. A roadway with low-strength surrounding rocks and

- significantly influenced by the fault structure was defined as roadway sensitive to stress disturbance (RSSD).
- (2) Laboratory tests show that the percentage of the clay minerals in the roof mudstone was 73.4%. The clay minerals are rich in illite, smectite, and chlorite, which can easily swell after absorbing water. The illite/smectite mixed layer ratio in the roof mudstone is 25%, resulting in a low-strength roof and poor adaptation of the roof to the surrounding environment.
  - (3) Field monitoring results demonstrate that the deformation of the rocks surrounding the roadway consists mainly of the dilatation of the shallow rocks and the separation of the deep rocks, which is consistent with the results from the borehole camera imaging. The borehole camera also showed two types of fissures in the surrounding rocks: horizontal and longitudinal fissures. Horizontal and longitudinal fissures will evolve into bed separation and fracture zones or alternatively will result in fracture zones accompanied by numerous new fissures that expand into deeper areas.
  - (4) The sphere of influence of the fault on the stress of the surrounding rocks is about 27 m. The fault exerts a maximum impact on the vertical stress of the rib rock mass and a minimum impact on the vertical stress of the floor rock mass, while the influence of the fault on the vertical stress of the roof rock mass is medium.
  - (5) Based on the laboratory test results, field monitoring, and numerical simulation results, we put forward a zonal support system for RSSD. We present an upgraded support scheme for the 6,63 haulage roadway with the most efficient design for the pretension of the rock bolt and anchor cable and determined the support system parameters for the roadway within the fault structure zone. Engineering practice shows that the deformation of the surrounding rocks of the roadway can be effectively controlled. Thus, normal and safe production in the mine is ensured.
- [2] H.-Q. Sun, S.-Y. Bao, L. Lin, and T.-P. Liao, "Predicting coal mining faults using combined rock relationships," *Mining Science and Technology*, vol. 19, no. 6, pp. 745–749, 2009.
  - [3] K. A. S. Phillips and E. G. Hellewell, "Three-dimensional ground movements in the vicinity of a mining activated geological fault," *Quarterly Journal of Engineering Geology*, vol. 27, no. 1, pp. 7–14, 1994.
  - [4] W.-J. Yu, W.-J. Wang, and Z.-J. Wu, "Analysis on activation laws caused by coal mining in fault footwall and its criterion," *Journal of Coal Science and Engineering*, vol. 18, no. 2, pp. 123–128, 2012.
  - [5] G. C. Rawling, L. B. Goodwin, and J. L. Wilson, "Internal architecture, permeability structure, and hydrologic significance of contrasting fault-zone types," *Geology*, vol. 29, no. 1, pp. 43–46, 2001.
  - [6] X. Hu, L. Wang, Y. Lu, and M. Yu, "Analysis of insidious fault activation and water inrush from the mining floor," *International Journal of Mining Science and Technology*, vol. 24, no. 4, pp. 477–483, 2014.
  - [7] M. R. Islam and R. Shinjo, "Mining-induced fault reactivation associated with the main conveyor belt roadway and safety of the Barapukuria Coal Mine in Bangladesh: constraints from BEM simulations," *International Journal of Coal Geology*, vol. 79, no. 4, pp. 115–130, 2009.
  - [8] Z.-P. Meng, S.-P. Peng, and H. Li, "Influence of normal faults on the physical and mechanical properties of coal and the distribution of underground pressure," *Journal of China Coal Society*, vol. 26, no. 6, pp. 561–566, 2001.
  - [9] H. C. Shen, Y. F. Cheng, J. Y. Wang et al., "Finite element study on the effects of faults on the ground stress field," *Petroleum Geology and Oilfield Development in Daqing*, vol. 4, pp. 34–37, 2007.
  - [10] W. J. Yu, Q. Gao, X. Q. Jin, and Z. P. Zhang, "Field investigation and mechanics characteristics analysis of deep rock mass affected by fault structure," *Progress in Geophysics*, vol. 1, article 055, 2013.
  - [11] A. Sachan and D. Penumadu, "Identification of microfabric of kaolinite clay mineral using x-ray diffraction technique," *Geotechnical and Geological Engineering*, vol. 25, no. 6, pp. 603–616, 2007.
  - [12] Itasca Consulting Group Inc, *FLAC3D (Fast Lagrangian Analysis of Continua in 3 Dimensions) Version 3.1 User's Manual*, Itasca Consulting Group Inc, Minneapolis, Minn, USA, 2002.
  - [13] Y. R. Liu and H. M. Tang, *Rock Mechanics*, Chemical Industry Press, Beijing, China, 2008 (Chinese).
  - [14] L. M. Dou, X. Z. Zou, S. G. Cao, and P. C. Lu, *Coal Mine Surrounding Rock Control and Monitoring*, China University of Mining and Technology Press, Xuzhou, China, 2007 (Chinese).
  - [15] B. H. G. Brady and E. T. Brown, *Rock Mechanics for Underground Mining*, Springer, Berlin, Germany, 2004.

## Competing Interests

The authors declare that they have no competing interests.

## Acknowledgments

Financial support for this work, provided by the National Natural Science Foundation of China for Young Scientists (no. 51304208), is gratefully acknowledged. The staff of the Key Laboratory of Deep Coal Resource Mining (CUMT) provided assistance with the laboratory tests; their meticulous work is gratefully acknowledged.

## References

- [1] M. Molinda and D. K. Ingram, "Effects of structural faults on ground control in selected coal mines in southwest Virginia," *International Journal of Mining and Geological Engineering*, vol. 8, no. 4, pp. 332–347, 1990.

## Research Article

# Research on the Rockburst Tendency and AE Characteristics of Inhomogeneous Coal-Rock Combination Bodies

Yun-liang Tan,<sup>1,2</sup> Wei-yao Guo,<sup>1,2</sup> Qing-heng Gu,<sup>1,2</sup> Tong-bin Zhao,<sup>1,2</sup> Feng-hai Yu,<sup>1,2</sup> Shan-chao Hu,<sup>1,2</sup> and Yan-chun Yin<sup>1,2</sup>

<sup>1</sup>State Key Laboratory of Mining Disaster Prevention and Control Co-Founded by Shandong Province and the Ministry of Science and Technology, Shandong University of Science and Technology, Qingdao 266590, China

<sup>2</sup>School of Mining and Safety Engineering, Shandong University of Science and Technology, Qingdao 266590, China

Correspondence should be addressed to Wei-yao Guo; 363216782@qq.com and Qing-heng Gu; 15610451523@163.com

Received 16 January 2016; Accepted 22 March 2016

Academic Editor: Shimin Liu

Copyright © 2016 Yun-liang Tan et al. This is an open access article distributed under the Creative Commons Attribution License, which permits unrestricted use, distribution, and reproduction in any medium, provided the original work is properly cited.

In order to research the influence of homogeneity on the rockburst tendency and on AE characteristics of coal-rock combination body, uniaxial compressive tests of inhomogeneous coal-rock combination bodies obeyed by the Weibull distribution were simulated using particle flow code (PFC<sup>2D</sup>). Macromechanical properties, energy evolution law, and AE characteristics were analyzed. The results show that (1) the elastic modulus homogeneity  $m_E$  has an exponential relation with macroscopic modulus  $E$ , and the bonding strength homogeneity  $m_\sigma$  has an exponential relation with uniaxial compressive strength  $\sigma_c$ ; (2) the rockburst tendency of the coal-rock combination body will increase with the increase of  $m_E$  or  $m_\sigma$ , and  $m_\sigma$  is the leading factor influencing this tendency; and (3) both the change law of AE hits and lasting time in different periods of AE characteristics are influenced by  $m_\sigma$ , but  $m_E$  just influences the lasting time. The more inhomogeneous the coal-rock combination body is, the shorter the lasting time in booming period of AE characteristics will be. This phenomenon can be used to predict the rockburst tendency of the coal-rock combination body.

## 1. Introduction

The geotechnical properties of rock associated with coal seams play a significant role in the design, operation, safety, and stability of both underground and open-cut mining operations [1, 2]. In particular, for the combined structure composed of coal and rock mass, its stability directly reflects dynamic disaster dangers, such as roof fall, coal bump, and rockburst. In the process of deep coal resources exploitation, the engineering accidents and disasters often happen due to the instability and failure of coal and rock structure. In particular, coal-rock dynamic disasters can be easily induced when roof and floor suddenly lose stability in the process of coal mining [3, 4]. Therefore, the interaction between the surrounding rock and coal is a key influencing factor in keeping the dynamic equilibrium of structure composed of roof, coal, and floor. In recent years, many researches focusing on coal-rock combination bodies have been fruitfully conducted, and some outstanding achievements have been obtained and

reported. For example, the research done by Qi et al. [5, 6] on different coal-rock combination bodies and the mechanism of rockburst reflected that employing coal-rock combination body to determine the tendency of rockburst was in more accordance with the actual underground conditions. Dou et al. [7–9] studied the rockburst tendency and precursor information of acoustoelectric effect, and the tests proved that coal-rock combination bodies could lose instability suddenly. Zuo et al. [10] found that the failure of combined coal-rock mass mainly occurred inside the coal, and the confining pressure, combination modes, and loading conditions play a very important role on the failure mode of combined samples. Petukhov and Linkov [11] analyzed the stability of general bipartite system and the roof-coal system when studying the stable behavior of rock mass after postpeak point. Vakili and Hebblewhite [12] developed a new cavability assessment criterion for top-coal embedded in combined coal-rock system composed of immediate roof, top coal, cutting coal, and floor by numerical modeling. Mohtarami et al. [13]

studied the interaction between soil mass and downward rock blocks as a combined structure by a theoretical model for stability analysis.

Rock is a kind of porous medium material composed of mineral crystals different in size and shape, and these crystals are bonded together by cement. It is very inhomogeneous in the microstructure, which means that rock is inhomogeneous material. Researches [14–16] have shown that the inhomogeneity has an important effect on the failure patterns of rock since the inhomogeneity of rock influences its physical and mechanical properties and the crack generation and evolution law during the failure process of rock. Thus studying the influence of inhomogeneity on the properties of coal-rock combination body has both academic and engineering values. It is, however, really hard to complete the study of homogeneous degree's influence on the properties of coal-rock combination body through physical experiments. Numerical method has become an important optional choice for this research. Unfortunately, only few literatures refer to the simulation experiments on the rockburst tendency of inhomogeneous coal or rock [17], and the influence on the rockburst tendency and AE characteristics of coal-rock combination body were not further analyzed.

Particle flow method can reflect the microcharacteristics of rock and shows the mechanism problems of rock mechanics. It is an effective method to study the rock mechanics problems from the microscopic view. In this paper, particle flow software PFC<sup>2D</sup> is used to simulate the macromechanical properties of inhomogeneous coal-rock combination bodies. In order to research the influence of homogeneity on the rockburst tendency and AE characteristics of coal-rock combination body, both energy evolution law and AE change law are analyzed during the failure process of coal-rock combination body under uniaxial compression tests.

## 2. Particle Flow Model of Inhomogeneous Coal-Rock Combination Bodies

**2.1. Inhomogeneous Simulation of Coal-Rock Combination Body.** Hudson and Fairhurst [18] emphasised that as the strength of rock is not an intrinsic property but the result of a stochastic chain reaction, the Weibull distribution is appropriate for describing the mechanical breakdown process. As a microscopic parameter setting method, it is widely used at present, especially for studying the inhomogeneity of rock. Its probability distribution function  $P(x)$  and probability density function  $f(x)$  are shown in formulas (1) and (2), respectively. Figure 1 shows probability density function curves of different  $m$ , when  $x_0$  is 1. From this figure, we can find that the larger the homogeneity  $m$  is, the smaller the discreteness of microparameters is. This means that the properties of coal or rock will become more homogeneous:

$$P(x) = 1 - \exp \left[ - \left( \frac{x}{x_0} \right)^m \right], \quad (1)$$

$$f(x) = \frac{m}{x_0} \left( \frac{x}{x_0} \right)^{m-1} e^{-(x/x_0)^m}, \quad (2)$$

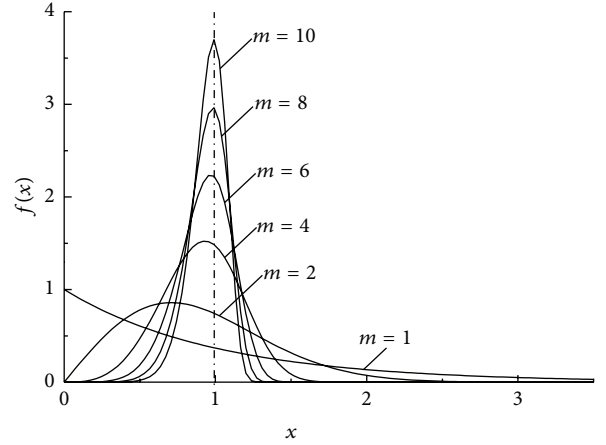


FIGURE 1: Curve of probability density of the Weibull distribution.

where  $x_0$  is the value of expectation and  $m$  is the value of homogeneity.

In particle flow code, particles are stiff. Particles are allowed to overlap each other for simulating the contact force between particles. There are two kinds of failure modes between particles, including shear failure and tension failure. PFC<sup>2D</sup> has two different bonding models (contact bond and parallel bond) built into the code. Generally, contact bond is used to simulate granular materials such as soil, and parallel bond is used to simulate compact materials such as rock [19]. We choose the parallel bond in this paper. Two experiment schemes are designed. The first scheme is to keep the bonding strength  $\sigma_0$  between coal particles 15 MPa and the bonding strength  $\sigma_1$  between rock particles 45 MPa, while the elastic modulus homogeneity  $m_E$  between them is changed, with the desired values for coal and rock as 4 GPa and 12 GPa, respectively. The second scheme is to keep the elastic modulus  $E_0$  between coal particles 4 GPa and the elastic modulus  $E_1$  between rock particles 12 GPa, while the bonding strength homogeneity  $m_\sigma$  between them is changed with the desired values for coal and rock as 15 MPa and 45 MPa, respectively ( $m_E$  and  $m_\sigma$  are short for elastic modulus homogeneity and bonding strength homogeneity later). Microparameters of coal and rock are shown in Table 1. The size of the model is  $50 \times 100 \text{ mm}^2$ , and this model is created by radius expansion method. The loading rate is 0.01 mm/s, and the loading model is shown in Figure 2. In order to analyze the energy accumulation and release, the change of deformation energy is recorded during the loading process.

**2.2. Index of Rockburst Tendency.** The impact energy index  $K_E$ , elastic energy index  $W_{ET}$ , and dynamic failure time  $D_T$  are often used for evaluating the rockburst tendency of coal. In this paper, the impact energy index  $K_E$  is introduced to study the effect of inhomogeneous parameters on the rockburst tendency of coal-rock combination body. As shown in Figure 3,  $K_E$  index refers to the ratio of the accumulative deformation energy  $F_s$  before stress peak to the releasable deformation energy  $F_x$  after stress peak under the condition of uniaxial compressive load. It reflects the

TABLE 1: Microparameters of rock and mine.

Materials	Density (kg/m <sup>3</sup> )	Radius (mm)	Friction coefficient	Radius of parallel bond (mm)	Elastic modulus (GPa)	Bonding strength (MPa)
Mine	1800	0.2~0.3	0.5	1	4	15
Rock	2600	0.2~0.3	0.5	1	12	45

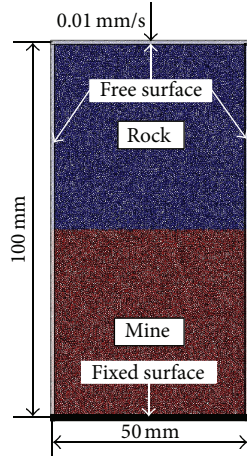


FIGURE 2: Test model.

energy transformation during the process of deformation and failure of coal-rock combination bodies.  $K_E$  is defined in (3). Consider

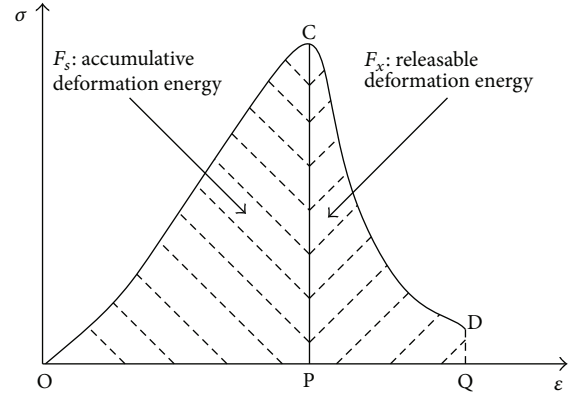
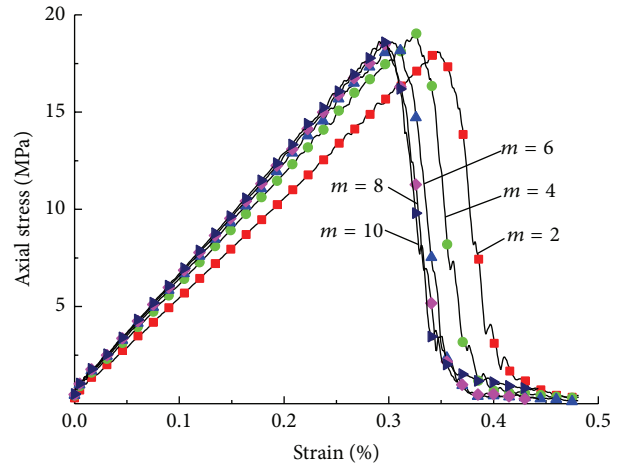
$$K_E = \frac{F_s}{F_x}, \quad (3)$$

where  $F_s$  is the accumulative deformation energy before stress peak and  $F_x$  is the releasable deformation energy after stress peak.

**2.3. Numerical Experiment Mechanism of AE Phenomenon.** AE events of rock are directly related to the generation of cracks, reflecting the crack formation of rock. AE is a good method for predicting rockburst [20, 21]. In the parallel bonding model of PFC<sup>2D</sup>, the formation of each crack will generate an AE pulse, and AE events of coal-rock failure can be simulated and calculated by recording the number of cracks and post-processing of the data. During the process of uniaxial compressive tests, the time series characteristic curves of AE can be obtained by the above-mentioned method to research the influencing rule of inhomogeneous parameters on AE characteristics of coal-rock combination body.

### 3. Homogeneity's Influence on the Rockburst Tendency of Coal-Rock Combination Body

**3.1. The Influence of Elastic Modulus Homogeneity.** Stress-strain curves for coal-rock combination bodies of different elastic modulus homogeneity  $m_E$  are shown in Figure 4. Figure 5 shows the relationship between macroelastic modulus  $E$  and  $m_E$ . From Figure 4, we can find that  $m_E$  influences

FIGURE 3: Calculation chart of  $K_E$ .FIGURE 4: Stress-strain curves of different  $m_E$ .

the uniaxial compressive strength of coal-rock combination body little but mainly influences the strain during the failure process. The larger  $m_E$  is, the lesser the strain is when the sample failure happens. The macroelastic modulus of coal-rock combination body increases with the increase of  $m_E$ , while the growth rate decreases gradually. The relationship between them can be described through an exponential function, which is shown in formula (4). Consider

$$E = 6.13 \times 10^9 - 2.14 \times 10^9 \times 0.675^{m_E}. \quad (4)$$

The bonding rupture number of different  $m_E$  during the loading process is shown in Figure 6. From Figure 6, we can see that  $m_E$  has little influence on the total number of bonding ruptures or its generation because the bonding strength between particles is not changed, but it has an obvious influence on the time of crack evolution. The lesser

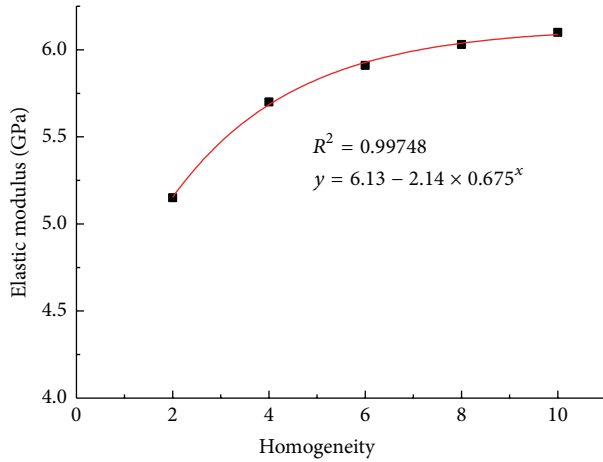


FIGURE 5: The relationship between elastic modulus and  $m_E$ .

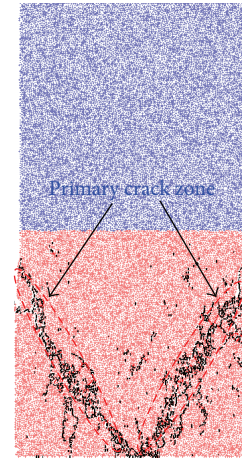


FIGURE 7: Failure mode of coal-rock combination body ( $m_E = 2$ ).

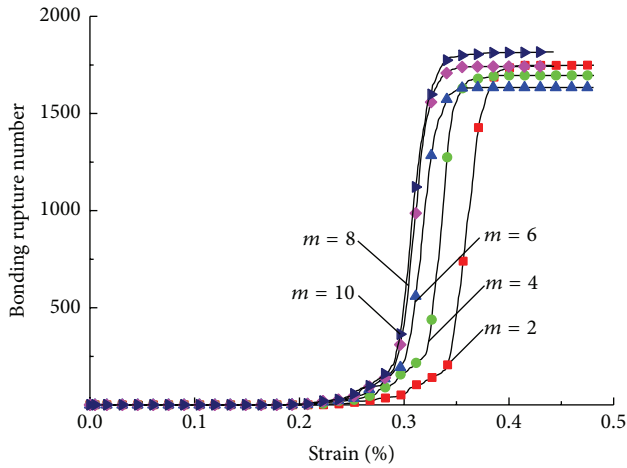


FIGURE 6: Bonding rupture number of different  $m_E$ .

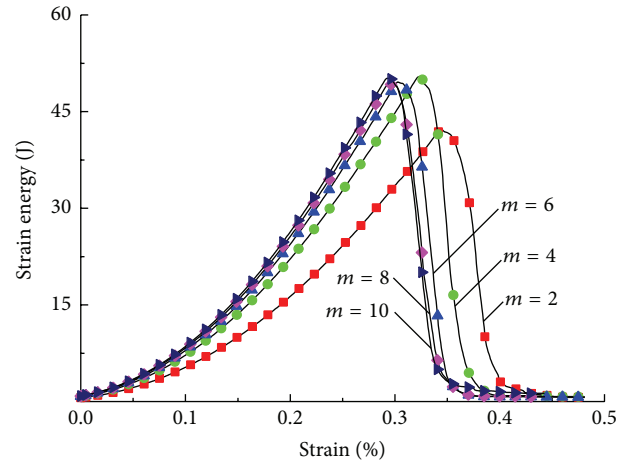


FIGURE 8: Energy curves of different  $m_E$ .

$m_E$  is, the longer the time of crack evolution is. What is more, the failure modes of different  $m_E$ , which are mainly “V shape” shear failure of coal, are similar, as shown in Figure 7 (this figure only gives the failure mode of coal-rock combination body when  $m_E$  is 2, because their failure modes are similar).

Strain energy curves of different  $m_E$  during the loading process are shown in Figure 8. This figure shows that when  $m_E$  is small, the accumulative strain energy before the failure of coal-rock combination body is relatively low. With the increase of  $m_E$ , the accumulative strain energy increases gradually, while  $m_E$  has little influence on the energy release after stress peak.

The relationship between impact energy index and  $m_E$  is shown in Figure 9. The impact energy index of coal-rock combination body shows a gradual increase with the increase of  $m_E$ . The amplitude of variation is small. When  $m_E$  increases from 2 to 10, impact energy index increases from 4.81 to 5.50 only by 0.14 times.

As a general view, the influence of  $m_E$  on the failure modes and strength of coal-rock combination body is small, but the influence on the strain is large. When  $m_E$  is small,

the difference of elastic modulus between particles is large, causing the coal and rock to be soft. During the loading process, the energy accumulates slowly. When the local stress exceeds the bonding strength between particles, crack generation happens, causing energy release. The release is abundant because of the long time of crack evolution. So the accumulative energy before the stress peak is small, and the rockburst tendency is weak. When  $m_E$  is large, the difference of elastic modulus between particles is small, and the process for accumulating energy is fast. So the energy release before the failure of coal-rock combination body is little, which means that the accumulative energy before the peak stress is large. That is why the rockburst tendency will strengthen if  $m_E$  is large.

**3.2. The Influence of Bonding Strength Homogeneity.** Stress-strain curves of coal-rock combination bodies for different bonding strength  $m_\sigma$  are shown in Figure 10. Figure 11 shows the relationship between uniaxial compressive strength  $\sigma_c$  and  $m_\sigma$ .  $m_\sigma$  has little influence on the macroelastic modulus of coal-rock combination body, but a big influence on the

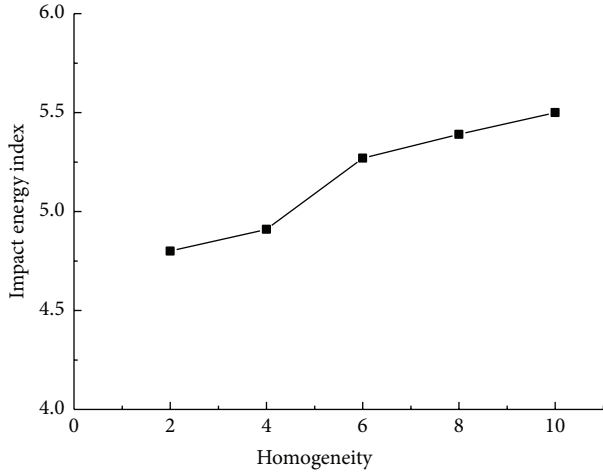


FIGURE 9: The relationship between impact energy index and  $m_E$ .

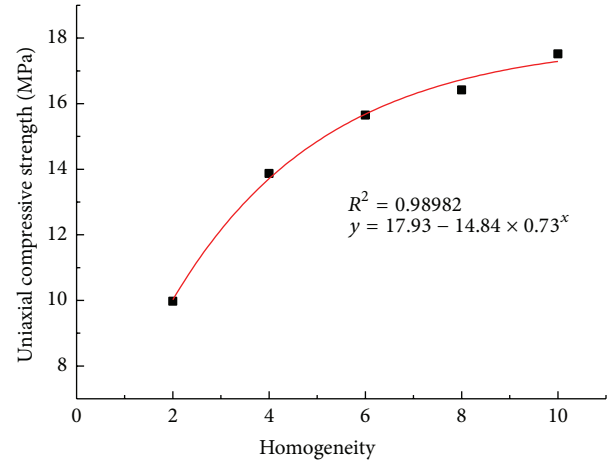


FIGURE 11: The relationship between uniaxial compressive strength and  $m_\sigma$ .

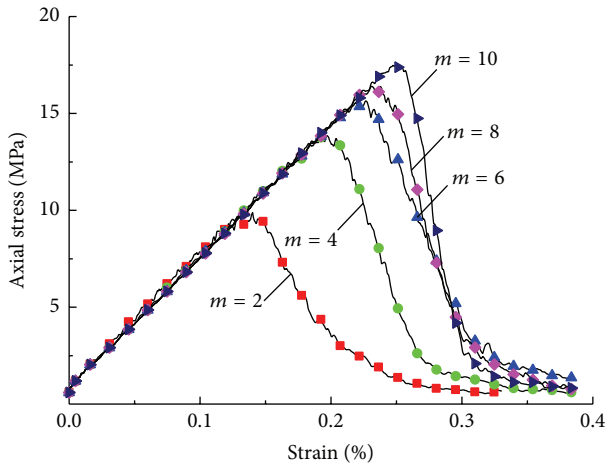


FIGURE 10: Stress-strain curves of different  $m_\sigma$ .

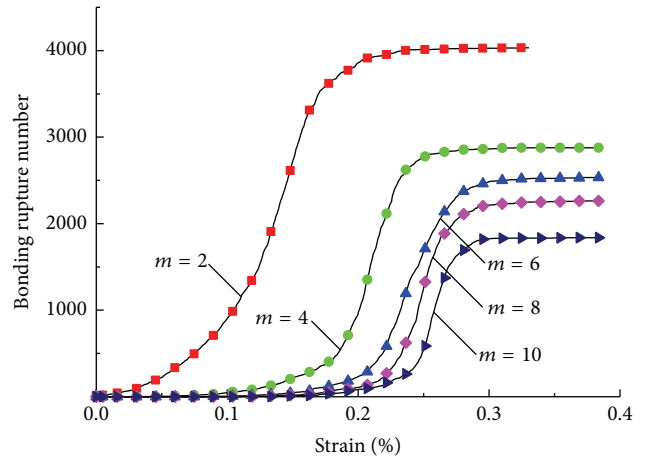


FIGURE 12: Bonding rupture number of different  $m_\sigma$ .

uniaxial compressive strength. The uniaxial compressive strength shows an increasing trend with the increase of  $m_\sigma$ , but its growth rate decreases. The relationship between them can be described by an exponential function, which is shown in formula (5). Consider

$$\sigma_c = 17.93 \times 10^6 - 14.84 \times 10^6 \times 0.73^{m_\sigma}. \quad (5)$$

The bonding rupture number of different  $m_\sigma$  during the loading process is shown in Figure 12. The smaller  $m_\sigma$  is, the longer the crack evolution time is, which will result in a larger number of bonding ruptures because of the great amount of particles of coal-rock combination body with low bonding strength under which cracks will generate, while the larger  $m_\sigma$  is, the shorter the crack evolution time is, which will result in lesser number of bonding ruptures when the samples are broken, because the bonding strength between particles is large and crack generation needs high stress.

Failure modes of different  $m_\sigma$  are shown in Figure 13. From Figure 13, “V shape” shear failure is found to be the main failure mode where  $m_\sigma$  has an obvious effect on the distribution of microfissures. When  $m_\sigma$  is small,

there are lots of microfissures distributing among the “V shape” shear zone. Both the randomness and discreteness of microfissures distribution are reduced with the increase of  $m_\sigma$ . What is more, these microfissures are gradually close to the “V shape” shear zone. Thus fissures localization is increasingly apparent, which means that the “V shape” shear zone becomes narrower.

Strain energy curves of different  $m_\sigma$  during the loading process are shown in Figure 14. From the prepeak state of strain energy curves, it shows that the accumulative strain energy increases with the increase of  $m_\sigma$ . From the postpeak state, it shows that the energy is released faster and faster with the increase of  $m_\sigma$ , easily leading to rockburst.

The relationship between impact energy index and  $m_\sigma$  is shown in Figure 15. When  $m_\sigma$  increases, the impact energy index of coal-rock combination body will increase and the rockburst tendency will become more obvious. The impact energy index rises from 1.54 to 4.38 as  $m_\sigma$  increases from 2 to 10. Combined with the above research, it is evident that the influence of  $m_\sigma$  on the rockburst tendency for coal-rock

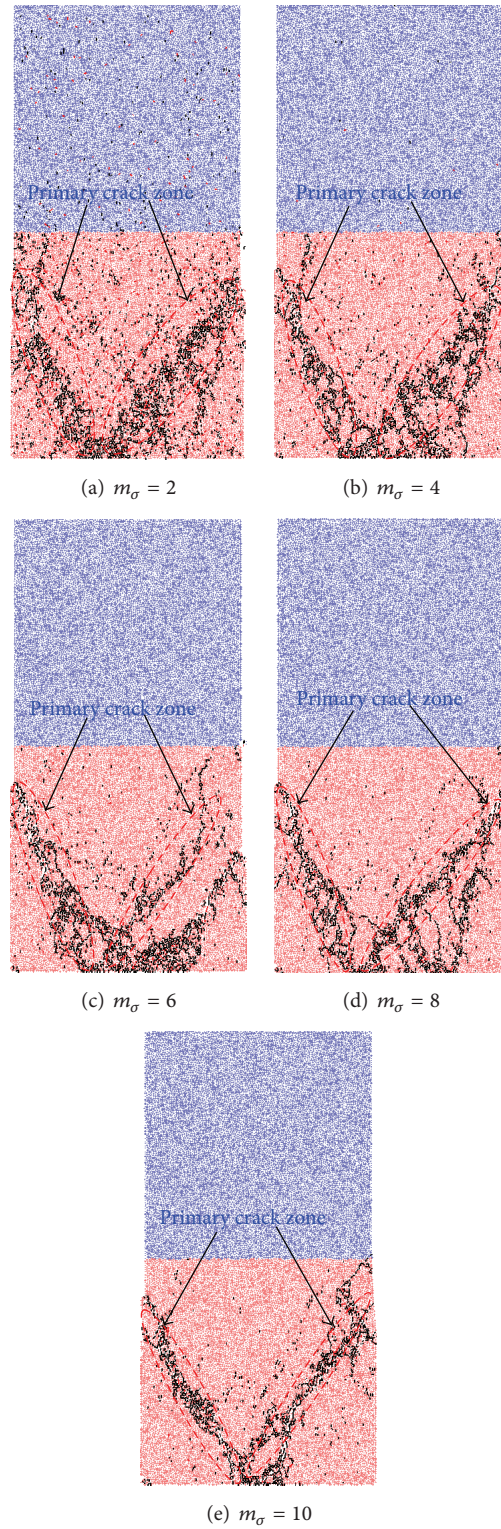
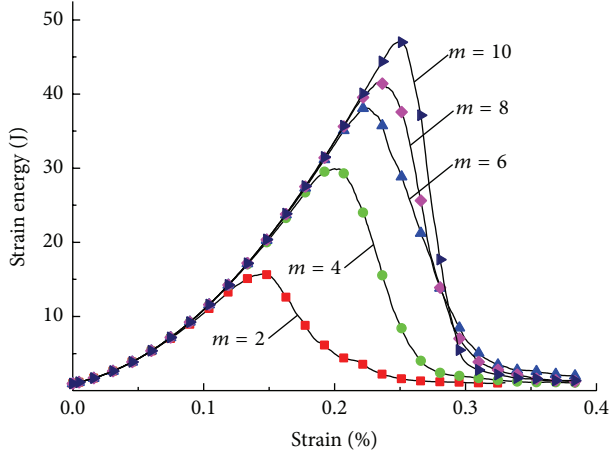
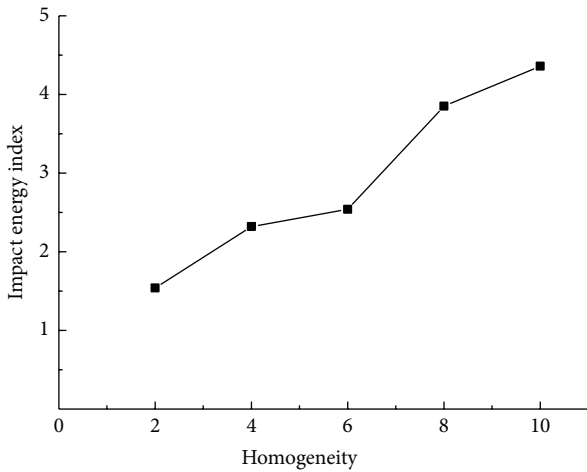


FIGURE 13: Failure modes of different  $m_\sigma$ .

combination body is stronger than that of  $m_E$ . So  $m_\sigma$  is the key controlling factor.

In general,  $m_\sigma$  has a strong influence on the failure modes and on the strength of coal-rock combination body.

Its influence, however, is small on the macroelastic modulus. When  $m_\sigma$  is small, the number of particles with lower bonding strength is large. In the initial stage of loading, the bonding of particles begins to break under low strength. It

FIGURE 14: Energy curves of different  $m_\sigma$ .FIGURE 15: The relationship between impact energy index and  $m_\sigma$ .

will last in the whole loading process, and the time of crack evolution is long. The accumulative energy before the stress peak is small due to the energy release. Thus the rockburst tendency is weak. However, when  $m_\sigma$  is large, the number of particles with higher bonding strength is high, the failure strength of coal-rock combination body is strong, and the time of crack evolution is short. The accumulative energy gets large and the rate of energy release goes fast. Therefore, the rockburst of coal-rock combination body is easy to happen.

#### 4. Homogeneity's Influence on AE Characteristics of Coal-Rock Combination Body

**4.1. The Influence of Elastic Modulus Homogeneity.** The relationship between the number of AE hits and strain during the failure process of coal-rock combination bodies under different  $m_E$  is shown in Figure 16. According to AE characteristics, the stress-strain curves can be generally divided into four stages: I: quiet period, II: developing period, III:

booming period, and IV: dropping period. The influence of  $m_E$  on the change law of AE hits is inapparent.

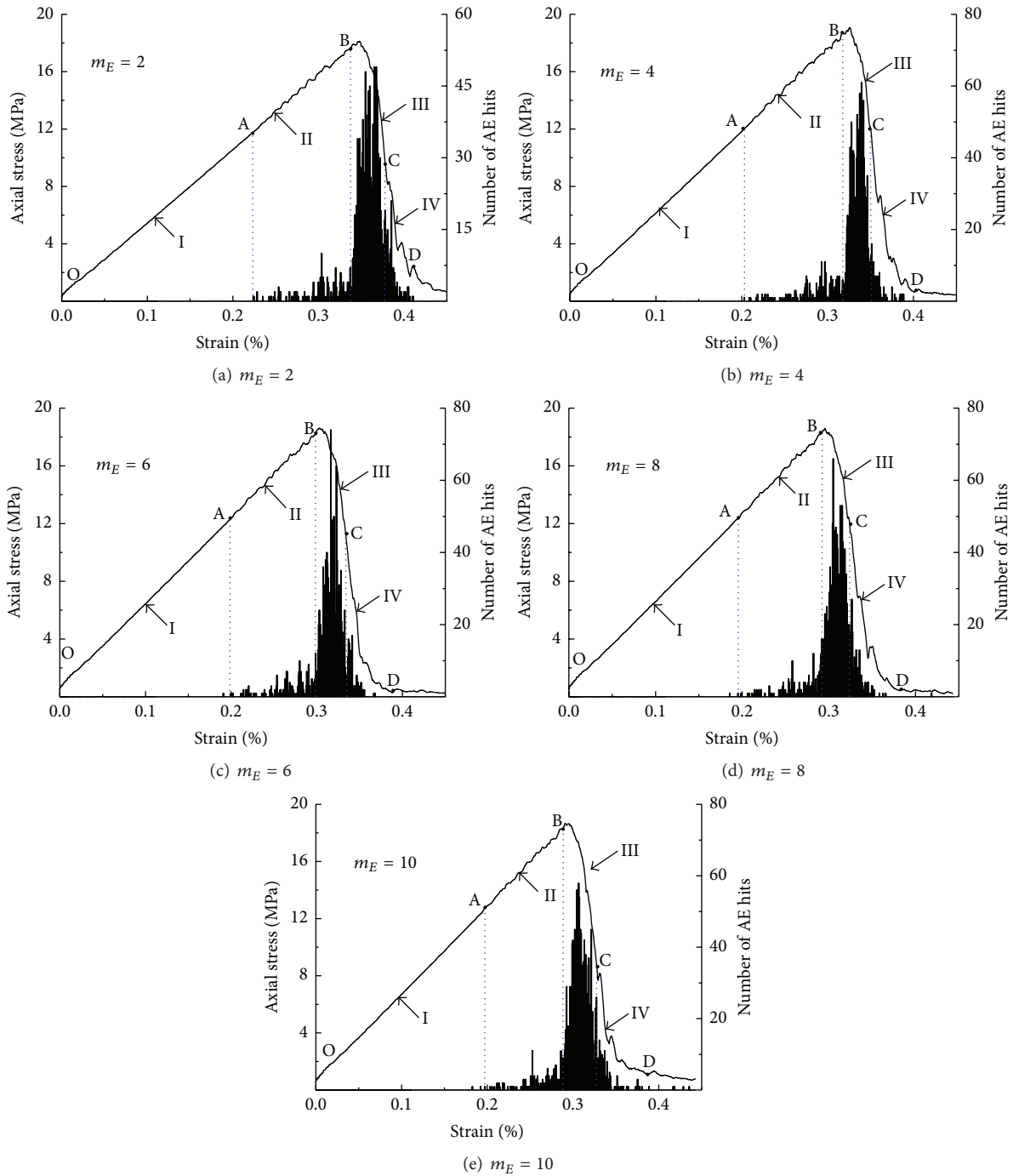
However, the duration times of AE characteristics under different  $m_E$  are various. AE phenomenon has a direct connection with the internal crack generation of samples, but  $m_E$  has little influence on the cracks' number. Thus, the influence of  $m_E$  on the change law of AE hits in different stages is unobvious.  $m_E$  influences the time of crack evolution greatly, causing lasting time under different  $m_E$  in each stage different. For example, when  $m_E$  increases from 2 to 10, the total strain in I, quiet period, and II, developing period, decreases from 0.339% to 0.289% and the strain in III, booming period, from 0.071% to 0.062%. This phenomenon implies that when  $m_E$  increases, the rate of both energy accumulation and energy release will increase, manifesting the increasing possibility of rockburst.

**4.2. The Influence of Bonding Strength Homogeneity.** The relationship between the number of AE hits and strain during the failure process of coal-rock combination bodies under different  $m_\sigma$  is shown in Figure 17. It is obviously shown that  $m_\sigma$  has a significant influence on the wholeness law of AE characteristics. The change law of AE hits for coal-rock combination body can be described as follows:

- (1) When  $m_\sigma$  is small, the combination body will come into the II, developing period, directly without I, quiet period, and the number of AE hits keeps high. As the load increases, the number of AE hits will increase continuously. It will be at a high level in both the prepeaking strength and postpeaking strength.
- (2) When  $m_\sigma$  continues to increase, the combination body will come into the I, quiet period, during the initiating loading, which shows no AE phenomenon. With the increase of load, the number of AE hits shows an obviously increasing trend until it comes into the III, booming period. After that, it comes into IV, dropping period, in which the number of AE hits decreases sharply.
- (3) When  $m_\sigma$  is high, AE phenomenon teems when near the III, booming period, whereas the number of AE hits is in a low level before that.

Above all, we can find that the AE characteristics of coal-rock combination body can preferably reflect the change of  $m_\sigma$ .

In addition, the lasting time of I, quiet period, increases with the increase of  $m_\sigma$ . For instance, when  $m_\sigma$  increases from 2 to 10, the strain of coal-rock combination body during the I, quiet period, increases from 0 to 0.105%. The duration of III, booming period, and peaking points of AE hits, however, shows a dropping tendency, such as the strain of coal-rock combination body during III, booming period, decreases from 0.043% to 0.026% as  $m_\sigma$  changes from 2 to 10. The reason is that the smaller  $m_\sigma$  is, the longer the crack evolution time is. The phenomenon shows that  $m_\sigma$  is the key factor influencing the change law of AE characteristics. It also implies that when  $m_\sigma$  is larger, the accumulative energy will be larger and

FIGURE 16: AE curves of different  $m_E$ .

the rate of energy release will be faster. So the larger  $m_\sigma$  is, the greater the possibility of rockburst will be.

## 5. Discussing the Influence of Homogeneous Parameters

Comparing the influence of the elastic modulus homogeneity  $m_E$  and bonding strength homogeneity  $m_\sigma$  on the rockburst tendency of coal-rock combination body, we know that the variable range of impact energy index influenced by

$m_E$  is 4.81~5.50 and the range influenced by  $m_\sigma$  is 1.51~4.38. Besides,  $m_\sigma$  influences greater the rockburst tendency of coal-rock combination body compared to  $m_E$ . Elastic modulus is an elastic deformation parameter. On the one hand, it has a strong influence on the elastic deformation but only has an effect on the energy accumulation before the failure of samples. On the other hand, it has a weak effect on the plastic deformation and postpeak failure, resulting in the fact that the energy release and crack generation of coal-rock combination body are

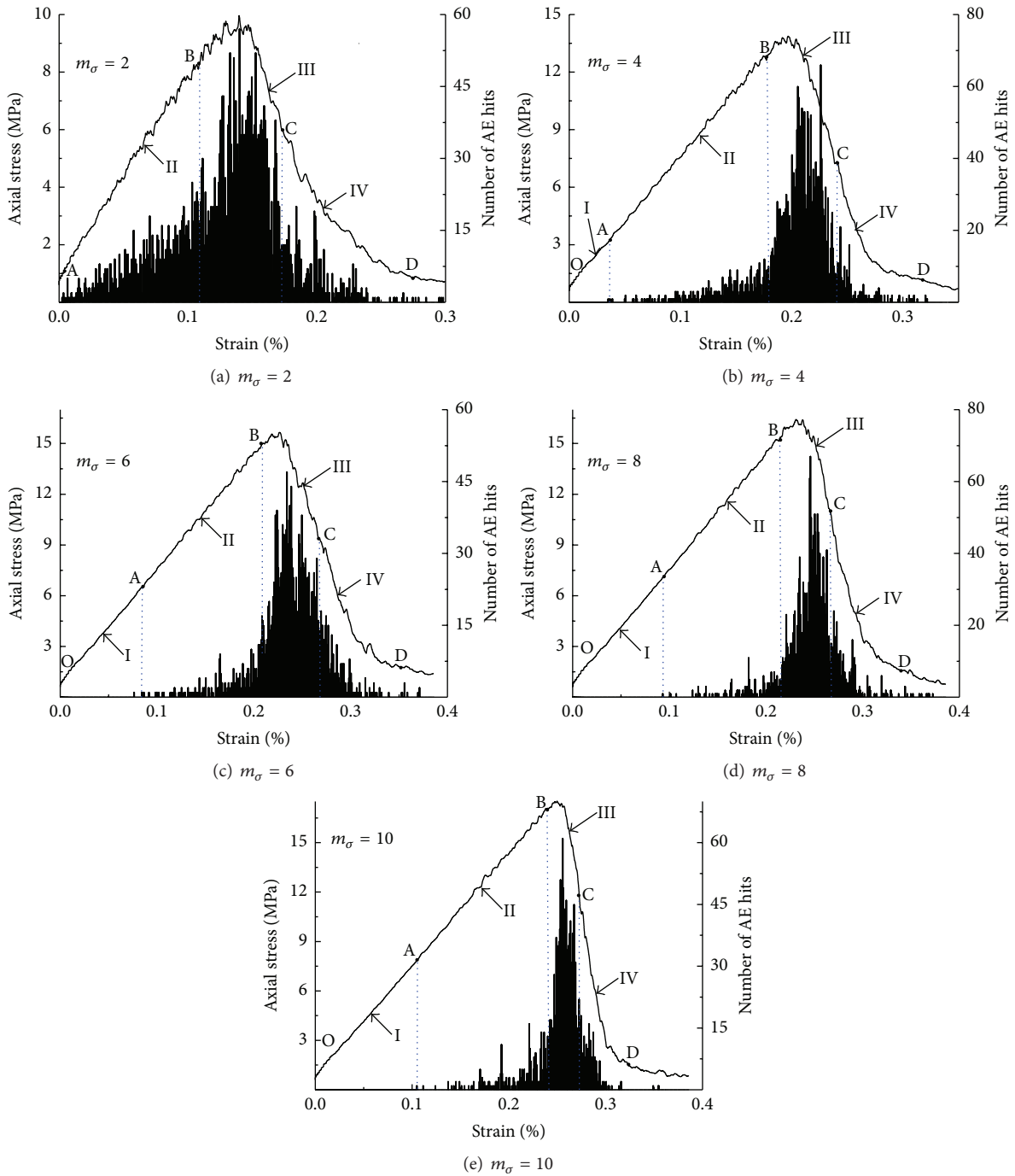


FIGURE 17: AE curves of different  $m_\sigma$ .

rarely influenced by  $m_E$ . Bonding strength mainly affects the failure process of coal-rock combination body. It controls the energy accumulation of prepeak strength, the energy release of postpeak strength, and the number of cracks. The AE phenomenon has a direct relation with the crack evolution law during the failure process of coal-rock combination body. Therefore,  $m_\sigma$  has a great influence on the rockburst tendency and AE characteristics for coal-rock combination body.

## 6. Conclusions

From the above research on the influence of homogeneity on the rockburst tendency and AE characteristics of coal-rock combination body, the conclusions are as follows:

- (1) The elastic modulus homogeneity  $m_E$  has a weak influence on the failure modes and the strength of coal-rock combination body, and its macroelastic modulus shows an exponential function relation with

$m_E$ . The bonding strength homogeneity  $m_\sigma$ , however, has a little influence on the macroelastic modulus of the combination, and its uniaxial compressive strength shows an exponential function relation with  $m_\sigma$ .

- (2) With the increase of elastic modulus homogeneity  $m_E$  or bonding strength homogeneity  $m_\sigma$ , the possibility of rockburst tendency of coal-rock combination body will be enhanced.  $m_\sigma$  plays a leading role in influencing the rockburst tendency. When  $m_\sigma$  increases from 2 to 10, the impact energy index increases from 1.54 to 4.38 by 1.84 times while  $m_E$  only increases by 0.14 times.
- (3) The bonding strength homogeneity  $m_\sigma$  has a strong influence on the wholeness law of AE characteristics, whereas the elastic modulus homogeneity  $m_E$  only influences the lasting time of AE characteristics in each stages.  $m_\sigma$  is the key factor influencing the change law of AE characteristics for coal-rock combination body. When  $m_E$  increases, the lasting time of I, quiet period, II, developing period, and III, booming period, shows a slowly dropping trend; when  $m_\sigma$  increases, the lasting time of I, quiet period, and II, developing period, increases but decreases during III, booming period.
- (4) Combined with homogeneity's influence on the rockburst tendency and AE characteristics of coal-rock combination body, we can find that the larger the homogeneous degree is, the stronger the rockburst tendency will be, while the lasting time of III, booming period, will decrease with the increase of the homogeneous degree. This phenomenon has an important guiding significance for monitoring the rockburst.

## Competing Interests

The authors declare that there are no competing interests regarding the publication of this paper.

## Acknowledgments

The research described in this paper was financially supported by Natural Science Foundation of China (no. 51474136, no. 51474137, and no. 51274133), Doctoral Scientific Fund Project of the Ministry of Education of China (no. 20123718110013), Tai'shan Scholar Engineering Construction Fund of Shandong Province of China, and Qingdao Postdoctoral Applied Research project (no. 2015198).

## References

- [1] C. R. Ward, Ed., *Coal Geology and Coal Technology*, Blackwell Scientific Publications, Melbourne, Australia, 1984.
- [2] L. Thomas, *Coal Geology*, John Wiley & Sons, New York, NY, USA, 2002.
- [3] Y. Tan, Y. Yin, S. Gu, and Z. Tian, "Multi-index monitoring and evaluation on rock burst in Yangcheng Mine," *Shock and Vibration*, vol. 2015, Article ID 624893, 5 pages, 2015.
- [4] Y.-L. Tan, J.-G. Ning, T.-B. Zhao et al., *Deformation and Control of Deep Roadways*, Coal Industry Press, Beijing, China, 2011.
- [5] Q.-X. Qi and L.-M. Dou, *Theory and Technology of Rock Burs*, China Mining University Press, Xuzhou, China, 2008.
- [6] J.-X. Liu, C.-A. Tang, W.-C. Zhu et al., "Rock-coal model for studying the rockburst," *Chinese Journal of Geotechnical Engineering*, vol. 26, no. 2, pp. 276–280, 2004.
- [7] L.-M. Dou, J.-C. Tian, C.-P. Lu et al., "Research on electromagnetic radiation rules of composed coal-rock burst failure," *Chinese Journal of Rock Mechanics and Engineering*, vol. 24, no. 19, pp. 3541–3544, 2005.
- [8] C.-P. Lu, L.-M. Dou, and X.-G. Wu, "Experimental research on rules of rockburst tendency evolution and acoustic-electromagnetic effects of compound coal-rock samples," *Chinese Journal of Rock Mechanics and Engineering*, vol. 26, no. 12, pp. 2549–2555, 2007.
- [9] Y.-X. Zhao, Y.-D. Jiang, J. Zhu, and G.-Z. Sun, "Experimental study on precursory information of deformations of coal-rock composite samples before failure," *Chinese Journal of Rock Mechanics and Engineering*, vol. 27, no. 2, pp. 339–346, 2008.
- [10] J.-P. Zuo, Z.-F. Wang, H.-W. Zhou, J.-L. Pei, and J.-F. Liu, "Failure behavior of a rock-coal-rock combined body with a weak coal interlayer," *International Journal of Mining Science and Technology*, vol. 23, no. 6, pp. 907–912, 2013.
- [11] I. M. Petukhov and A. M. Linkov, "The theory of post-failure deformations and the problem of stability in rock mechanics," *International Journal of Rock Mechanics and Mining Sciences & Geomechanics Abstracts*, vol. 16, no. 2, pp. 57–76, 1979.
- [12] A. Vakili and B. K. Hebblewhite, "A new cavability assessment criterion for longwall top coal caving," *International Journal of Rock Mechanics & Mining Sciences*, vol. 47, no. 8, pp. 1317–1329, 2010.
- [13] E. Mohtarami, A. Jafari, and M. Amini, "Stability analysis of slopes against combined circular-toppling failure," *International Journal of Rock Mechanics and Mining Sciences*, vol. 67, pp. 43–56, 2014.
- [14] S. C. Yuan and J. P. Harrison, "A review of the state of the art in modelling progressive mechanical breakdown and associated fluid flow in intact heterogeneous rocks," *International Journal of Rock Mechanics and Mining Sciences*, vol. 43, no. 7, pp. 1001–1022, 2006.
- [15] Y.-L. Tan, D.-M. Huang, and Z. Zhang, "Rock mechanical property influenced by inhomogeneity," *Advances in Materials Science and Engineering*, vol. 2012, Article ID 418729, 9 pages, 2012.
- [16] Y.-L. Tan, Y.-C. Yin, and D. Huang, "Inhomogeneous micro-structure influence on macro-crack of sandstone," *Journal of Testing and Evaluation*, vol. 41, no. 6, pp. 1024–1031, 2013.
- [17] T.-B. Zhao, Y.-C. Yin, Y.-L. Tan, P. Wei, and J.-C. Zou, "Bursting liability of coal research of heterogeneous coal based on particle flow microscopic test," *Journal of the China Coal Society*, vol. 39, no. 2, pp. 280–285, 2014.
- [18] J. A. Hudson and C. Fairhurst, "Tensile strength, Weibull's theory and a general statistical approach to rock failure. Structure, solid mechanics and engineering design," in *The Proceedings of the Southampton 1969 Civil Engineering Materials Conference*, M. Te'eni, Ed., pp. 901–914, 1969.

- [19] Y.-C. Yin, T.-B. Zhao, Y.-L. Tan et al., "Research of stress distribution evolution law and influencing factors," *Journal of Mining & Safety Engineering*, vol. 30, no. 5, pp. 712–716, 2013.
- [20] Y.-L. Tan, Z. Zhang, and T.-B. Zhao, "AE pattern of rock burst disaster induced by strata activation in coal mine," *Disaster Advances*, vol. 4, no. 4, pp. 29–33, 2011.
- [21] Y.-L. Tan, F.-C. Li, H. Zhou, and X.-J. Han, "Analysis on acoustic emission pattern for rock burst," *Chinese Journal of Rock Mechanics and Engineering*, vol. 19, no. 4, pp. 425–428, 2000.